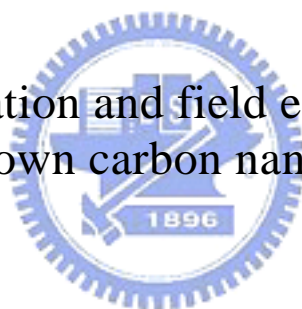


國立交通大學

材料科學與工程學系
博士論文

選擇性沉積碳奈米結構圖案之奈米操控
與場效發射研究

Nano-manipulation and field emission study of the
selectively grown carbon nanostructures pattern



研究生：林貞君

指導教授：郭正次 教授

潘扶民 教授

中華民國九十八年一月

選擇性沉積碳奈米結構圖案之奈米操控與場效發射研究

Nano-manipulation and field emission study of the selectively
grown carbon nanostructures pattern

研究生：林貞君

Student: Chen-Chun Lin

指導教授：郭正次 教授

Advisors: Prof. Chen-Tzu Kuo

潘扶民 教授

Prof. Fu-Ming Pan

國立交通大學

材料科學與工程學系

博士論文

A Thesis

Submitted to Department of Materials Science and Engineering

College of Engineering

National Chiao Tung University

in partial Fulfillment of the Requirements

for the Degree of

Doctor of Philosophy

in

Materials Science and Engineering

January 2009

Hsinchu, Taiwan, Republic of China

中華民國九十八年一月

選擇性沉積碳奈米結構圖案之奈米操控與場效發射研究

研究生：林貞君

指導教授：郭正次 教授
潘扶民 教授

國立交通大學
材料科學與工程學系

摘要

操控碳奈米結構(CNSs)沉積的位置、密度與排列方向為目前碳奈米技術主要的研究課題之一，本研究主要目的為開發在指定的區域沉積具有方向性排列的 CNSs 製程，並且量測其結構與性質特性，使用的三種製程包含陽極氧化鋁(AAO)模板及觸媒輔助方法、無電鍍觸媒輔助法及電泳輔助沉積法。在 CNSs 的結構與性質分析方面，包含 SEM、EDS、TEM、HRTEM、Raman、AES，及場效發射電性量測；利用紫外可見光吸收光譜(UV-Vis absorption spectroscopy)及界達電位量測(Zeta potential measurements)進行 CNSs 懸浮液之穩定性分析。

第一種製程是 AAO 模板及觸媒輔助方法，首先在矽基材上沉積鋁膜，利用兩階段陽極氧化處理製備出具有均勻孔洞大小直徑約 80 nm、厚度約 550 nm 的奈米孔洞作為模板，以電鍍法沉積鈷觸媒於 AAO 孔洞內，再以電子迴旋共振化學氣相沉積法合成 CNSs，為製作場發射陣列，SiO₂ 介電層與 Al 閘極層分別沉積於 CNSs 上，經黃光製程後利用乾式與濕式蝕刻方法顯露出場發射區域。在模板輔助成長下，當電鍍鈷觸媒的時間為 45 s 時(高度約 48 nm)，CNSs 的平均直徑約 22 nm，密度約 37 #/μm²；當鈷電鍍時間增加為 90 s 時(高度約 84 nm)，CNSs 的直徑約 53 nm，密度約 162 #/μm²。為了解 CNSs 在受限制的 AAO 通道內如何成長，提出一個可能的成長機制。CNSs 大部份為頂端成長模式，並且存在一個最佳的鈷觸媒電鍍時間 60 s，CNSs 的平均直徑約 25 nm，密度約 45 #/μm²，具有較佳的場發射特性(起始電場為 5.1 V/μm)，其相對應製作的 CNSs 場發射陣列具有起始電壓 8.1 V/μm 的場發射特性。此方法可以彰顯以 AAO 做為模板，可以有效的控制 CNSs 場發射陣列的結構與特性

第二種製程是無電鍍觸媒輔助法，其主要的目的為利用微波電漿化學氣相沉積系統在具溝槽之圖案矽基材上，選擇性成長水平奈米碳管(CNTs)橫跨其溝槽。此製程之選擇性是利用無電鍍法在觸媒於無晶矽層(a:Si)上析出觸媒金屬之化學反應性甚大於氮化矽層(Si₃N₄)，而 Si₃N₄ 層設計鍍在 a:Si 層上，可導引 CNTs 水平成長方向成長。結果顯示 CNTs 主要為竹節狀多壁結構，管壁石墨層數約 20~30。CNTs 的電導性可經由 760°C 的熱退火後，得到很大的改善。結果展現水平成長 CNT 之數目可藉由觸媒電鍍時間與溝槽寬度來調控。本製程亦具有製造奈米元件導線之潛力。

第三種製程是 CNSs 電泳輔助沉積法，利用電泳沉積法(EPD)及後續的退火處理將單壁奈米碳管(SWNTs)選擇性沉積在各種材料或圖案上。此 EPD 製程首先將 SWNTs 與三種分散劑或界面活性劑(SDS、TOPO、CTAB)配製成 CNTs 懸浮液。結果顯示就 SWNTs 的分散性及懸浮液穩定性而言，SDS 為最好的界面活性劑。EPD 製程參數中，除了 CNT 的濃度之外，對於薄膜場發射與附著性並無顯著的影響。然而要改善薄膜與基材間的附著性需要施予較高的退火溫度加上適當的退火時間，並因而降低電阻，提高場發射特性。高效率的退火薄膜具有小的內應力，其結構往往是由許多微米大小的島狀結構組成，而小島間有許多水平排列的 CNTs。另外，就應用 EPD 製程於不同基材的可行性，例如導電玻璃，其圖案是由具有導電及不導電材料所組成(Al 和 SiO₂)，或在不同形狀基材之可行性，例如彎曲的鋁箔紙，本製程可以成功的用來選擇性沉積 CNTs 圖案。



Nano-manipulation and field emission study of the selectively grown carbon nanostructures pattern

Student: Chen-Chun Lin

Advisors: Prof. Cheng-Tzu Kuo
Prof. Fu-Ming Pan

Department of Materials Science and Engineering
National Chiao Tung University

Abstract

How to deposit or manipulate the carbon nanostructures (CNSs) with the desired orientation, number density and locations to form patterns is one of the key issues for fabricating the nanodevices. The purpose of this research is to develop nanofabrication processes to manipulate the CNSs patterns and to examine their structures and properties. The developed processes may be roughly divided into three categories, including the anodic aluminum oxides (AAO) template-catalyst-assisted, the electroless plating catalyst-assisted, and CNSs-electrophoresis-assisted processes. The structures and properties of the CNSs and their patterns were characterized by SEM, EDS, TEM, HRTEM, Raman, AES, and field emission I-V measurements. The stability of CNSs-suspensions was evaluated by UV-Visible absorption spectroscopy and Zeta potential measurements.

For the AAO template-catalyst-assisted process, nanoporous AAO template was first prepared by a two-step anodization process on the Si(100) substrate with 80 nm in diameter and 550 nm in depth, followed by Co catalyst and the vertically aligned CNSs deposition in AAO pore channels by electron cyclotron resonance chemical vapor deposition (ECR-CVD). The field emitter arrays were further prepared by directly depositing SiO₂ dielectric and Al gate layer on the CNSs. Reactive ion and wet etches were then used to open the field-emission area. The results show that the average diameters and the corresponding number density of the AAO-assisted CNSs vary from 22 nm, 37 #/μm² to 53 nm, 162 #/μm² for Co deposition times of 45 s (~ 48 nm in height) and 90 s (~ 84 nm in height), respectively. A mechanism is first proposed to delineate the CNS growth in a confined pore channel space of the AAO template. The CNSs are mainly the tip-growth type in structure and there is existence of an optimum field emission turn-on field of 5.1 V/μm for AAO-assisted CNSs with ~ 25 nm in diameter and ~ 45 #/μm², which is corresponding to the turn-on field of 8.1 V/μm for the emitter array. The results had demonstrated that the structure and properties of CNSs emitter array can be effectively manipulated by this AAO template-assisted process.

For the electroless plating catalyst-assisted process, the main purpose was to selectively grow the horizontally-oriented carbon nanotubes (CNTs) across the trenches of the patterned Si wafer in a microwave plasma CVD system. The CNT selectivity of the process is based on

the greater chemical reactivity of the catalyst with a:Si than with Si_3N_4 , where the Si_3N_4 barrier layer of the pattern was designed on top of the a:Si layer to guide the growth of CNTs in horizontal direction to bridge across the trenches of the pattern. The CNTs are mainly bamboo-like multiwalled CNTs (MWNTs) with a wall thickness of 20~30 graphene layers. Its electrical conductivity can be greatly improved by subjecting to 760°C heat treatment under nitrogen atmosphere. The results demonstrate that the amounts of the horizontally-oriented CNTs are tunable with the Ni catalyst plating time and the trench width. This process also demonstrates the potential for nano-connector fabrication in nano devices.

For CNSs-electrophoresis-assisted method, electrophoretic deposition (EPD) followed by post air annealing treatment was developed to selectively deposit the single-walled CNTs (SWNTs) on various substrates or patterns. The EPD was conducted from a solution mixture of SWNTs and various dispersants or surfactants, including sodium dodecyl sulfate (SDS), hexadecyl trimethyl ammonium bromide (CTAB) and tricylphosphine oxide (TOPO). The results indicate that the SDS is the best surfactant in terms of SWNTs dispersion and solution stability, and the EPD parameters, except CNTs concentration in the suspension, have no significant effects on their field emission (FE) and adhesion properties of the deposited films. However, a higher post annealing temperature combined with an optimum annealing time is required to improve the film-substrate adhesion, so to reduce its electrical resistance and to enhance FE properties. The high performance annealed films with negligible internal stress are made of the micro-sized islands with the horizontally oriented SWNTs between them. On feasibility to apply the EPD process on other substrate materials such as ITO, the pattern made of conductive and nonconductive coatings (Al and SiO_2), or the substrates with different shapes like curved Al-foil, can be successfully used to selectively deposit CNTs pattern by EPD.

Acknowledgements (謝辭)

首先，學生由衷地感謝 **郭正次教授**與 **潘扶民教授**的耐心指導、論文寫作技巧方面的悉心教誨、提供齊全的研究設備與資源，並且在待人處世方面給予提醒與啟發，使我受益匪淺，謹此致以最誠摯的謝意。同時感謝考試委員成大機械系 **李驊登教授**、交大材料系 **張立教授**、逢甲材料系 **何主亮教授**、中興材料系 **呂福興教授**、北科大機械系 **林啟瑞教授**的親臨指導，有了您的寶貴意見與指導，使得本論文更具完整性。

家人的支持是我最重要的力量，首先感謝我的最佳智囊團帥**爸爸**還有俏皮可愛的**媽媽**，每當我在學校遇到煩惱的事情或是身體不舒服的時候，最愛回到溫暖的家了，也希望爸爸媽媽的身體健康，我終於要出去賺錢了，你們可以多安排一點休閒活動，好好享受一下；跟我一起住的體貼型**男弟弟**保鏢，每當大風大雨或是太晚回家的時候就變成我的司機，真的我幫了不少忙，希望你的學業還有以後的工作都能順順利利；生活多采多姿又越來越漂亮的**妹妹**，少了愛打扮的妳時時叮嚀我，我都變醜了啦！也祝你學業順利還有天天快樂阿！給我最想念的**外公**，常常懷念博一住在外公家的日子，祖孫倆一起分享偷偷吃挫冰的滿足感，每次出國參加研討會您一定舉雙手贊成，還會給我紅包當旅費哩；最時髦最有品味的外婆，您總是關心我的身體還有近況，絕頂的廚藝、風趣的談吐總是讓大家充滿歡樂，希望您的身體健康，永遠美麗。還有感謝最多鬼點子的**阿嬤**還有最愛玩的小舅，每次的家庭聚會總是獨一無二歡樂無窮，是最好的放鬆劑了。

感謝好朋友們的鼓勵與陪伴，首先是最捨不得的好朋友**澎澎**，本來說好要來參加我的畢業典禮的，我們總是分享生活中大大小小的事情，一起經歷快樂還有傷心，你也總是給我最大的鼓勵，要我克服困難，謝謝妳，我永遠都會想念妳的；最喜歡給我驚喜的小倩，雖然平常大家各忙各的，但是你就是三不五時會來看看我這個老朋友，讓我知道你一直有在關心我，我每次都很感動的，也祝你早日畢業，我也會三不五時幫你加油的喔！給有著堅強毅力的**Shally**，你是我的力量加油站，也是最會叮嚀我的造型顧問，希望你趕快學成歸國阿；還有一同從碩士開始奮鬥的**心心**與**庭庭**，有你們的相挺，研究的路上不孤單，也希望你們都能一切順利，還有趕快找到另一半囉；還有重要的**Kaoming**，總是在我身邊照顧我、給我力量，是我的一大精神支柱阿，希望你能天天開心、心想事成啦！

感謝一起作實驗打拼的伙伴，**凱鈞**、**盈君**還有**全雯**，有了你們大力的幫忙，我的論文才能完整。同窗副修體育系的室長**必愷**，肩負著設備工程師的使命，也帶領著固定運動的氣氛，我們可是每年都有得到環校路跑的運動衫呢！希望你身體健康，還有早日畢業喔！最仔細、貼心的**伊茹**，不管在學業或是生活中，總是感受到你的體貼，我們的葡西之旅還有每年的生日心機都是令人難忘的一段回憶，祝福你趕快實現夢想！旅遊伙伴的第一人選還有購物達人**淑筠**，每次跟你出去玩怎麼覺得就是特別的瘋狂好玩，要買東西或是學校裡面大大小小的事情問你就對了，真是太高興有你這麼好的助理與朋友！才剛開始熟的**泰瑞**，你的熱情開朗還有真誠是我覺得最難得的，希望你能繼續保持下去，並且一切順利啦。另外，感謝**柏林**學長、**兆焄**學長、**威翔**學長、**德銘**學長在實驗上的建議，謝謝**協宗**、**岳翰**、**玉容**、**祐君**、**土狼**、**峻愷**、**國銘**、**奕同**、**詩容**、**淑幸**、**蝗蟲**、**文綏**、**立群**、**碩傑**、**宜學**、**怡萱**等等在實驗與生活上的協助。同時要感謝華映與**莫處長**提供產學合作的機會與獎學金，並謝謝**劉梅**、**美昭**的照顧。

最後，再一次跟大家說聲謝謝，很高興在交大這段期間，可以認識大家，讓我的生活更豐富。

Contents

Abstrate in Chinese (摘要).....	I
Abstract in English	III
Acknowledgements in Chinese (謝辭).....	V
Contents	VI
List of Symbols.....	VIII
Table Caption.....	X
Figure Caption	XI
Chapter 1 Introduction.....	1
Chapter 2 Literature Review	3
2.1 Overview of the CNSs.....	3
2.2 Applications of the CNSs	7
2.3 Selective deposition methods for the nanostructures	17
2.4 Fabrication methods for the oriented CNSs	23
2.5 Analysis methods of the CNSs	26
2.5.1 Morphologies, and lattice image analyses.....	26
2.5.2 Bonding and crystal structure analyses	27
2.5.3 Electrical, optical and thermal properties measurements.....	28
Chapter 3 Experimental Methods.....	30
3.1 Experimental flowcharts.....	30
3.2 AAO template-catalyst-assisted process.....	34
3.2.1 AAO-template preparation by anodization process.....	34
3.2.2 Catalyst deposition in the nanopores of AAO template by electroplating	36
3.2.3 CNSs deposition by ECR-CVD.....	36
3.2.4 Fabrications of the emitter arrays on the AAO-assisted CNSs.....	37
3.3 Electroless plating catalyst-assisted process	40
3.3.1 Substrate preparation for selective deposition of catalyst	40
3.3.2 Catalyst deposition by electroless plating	41
3.3.3 CNTs deposition by MPCVD.....	42
3.3.4 RTA heat treatment	43
3.4 CNSs-electrophoresis-assisted process.....	45
3.4.1 Substrate preparation for selective deposition.....	45
3.4.2 Suspensions preparation for CNTs dispersion.....	46
3.4.3 The electrophoretic processes with CNT suspensions.....	46
3.4.4 Post-annealing	46
3.5 Structures and properties characterization.....	48
3.5.1 SEM, TEM, EDS and HRTEM	48

3.5.2 AES	48
3.5.3 Raman spectroscopy	48
3.5.4 XPS	49
3.5.5 Electrical properties measurement.....	49
3.5.6 UV-Vis spectroscopy and Zeta potential measurement	50
Chapter 4 Results and discussion for the AAO template-catalyst-assisted CNSs emitter arrays	52
4.1 Morphologies of AAO template and Co catalysts in nanopores	52
4.2 Effects of the Co plating time on the AAO template-catalyst- assisted CNSs	54
4.2.1 On morphologies of the CNSs.....	54
4.2.2 On Raman spectra and TEM images of the CNSs.....	55
4.2.3 On number density of the CNSs and growth mechanism discussion.....	59
4.2.4 On field emission properties of the CNSs	63
4.3 Effects of the processing parameters of the field emitter arrays	64
4.3.1 Effect of the CNSs growth time on SiO ₂ film morphology.....	64
4.3.2 Effect of the etching times and methods on emitter morphology and CNSs Raman spectra	65
4.4 Field emission properties of the emitter arrays	69
4.5 Summary.....	70
Chapter 5 Results and discussion for the electroless plating catalyst-assisted process.....	71
5.1 Compositions of the catalyst films by XPS and EDS.....	71
5.2 Morphologies and lattice images of the catalyst nanoparticles and the as-deposited CNTs.....	74
5.3 Auger spectra at different positions on the Ni catalyst-deposited pattern	78
5.4 Morphologies at trench on the pattern with the Ni-assisted CNTs.....	79
5.5 I–V curves of the pattern with the horizontally-aligned CNTs across trenches	82
5.6 Summary.....	83
Chapter 6 Results and discussion for the CNSs-eletrophoresis-assisted process.....	84
6.1 Raman spectrum of the raw SWNTs	84
6.2 Effect of the surfactant type on stability of SWNT suspensions	85
6.3 Effect of post annealing on morphologies and field emission properties of the CNSs-EPD-assisted films	88
6.4 CNSs deposition selectivity of the pattern components by EPD	91
6.5 Substrate diversifications of the EPD process.....	92
6.6 Summary.....	93
Chapter 7 Conclusions.....	94
Chapter 8 Future Prospects.....	96
References	97

List of Symbols

A	Absorbance
AAO	Anodic aluminum oxide
a:C	Amorphous carbon
AES	Auger electron spectroscopy
AFM	Atomic force microscope
a:Si	Amorphous silicon
BE	Binding energy
BOE	Buffered oxide etchant
CNFs	Carbon nanofibers
CNSs	Carbon nanostructures
CNT-FETs	Carbon nanotube -field effect transistors
CNTs	Carbon nanotubes
CTAB	Hexadecyl trimethyl ammonium bromide
CVD	Chemical vapor deposition
DSSC	Dye-sensitized solar cells
ECR-CVD	Electron cyclotron resonance chemical vapor deposition
EDS	Energy dispersive spectroscopy
E_F	Energy level of the free electrons
E_{to}	Turn-on field
EPD	Electrophoretic deposition
ϕ	Work function
FE	Field emission
FED	Field emission display

FIB	Focused ion beam
F-N	Fowler-Nordheim
HDP-RIE	High density plasma reactive ion etching
HRTEM	High resolution transmission electron microscopy
I	The intensity of light passing through a sample
I_0	The intensity of light before it passes through the sample
I / I_0 or %T	Transmittance or express in percentage (%T)
LPCVD	Low-pressure CVD
M_{ion}	Metallic ions
MPCVD	Microwave plasma chemical vapor deposition
MWNTs	Multi-walled carbon nanotubes
OPVs	Organic photovoltaic devices
PL	Photoluminescence
RIE	Reactive ion etching
RTA	Rapid thermal annealing
RBM	Radial breathing mode
STM	Scanning tunneling microscopy
SDS	Sodium dodecyl sulfate
SEM	Scanning electron microscopy
SWNTs	Single-walled carbon nanotubes
TEM	Transmission electron microscopy
TGA	Thermogravimetric analysis
TOPO	Trioctylphosphine oxide
UV-Vis	Ultraviolet-visible

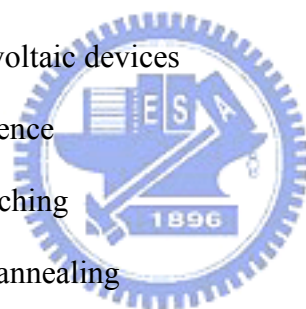


Table Caption

Table 3-1 Specimen designations of the AAO-assisted CNSs and their deposition conditions	39
Table 3-2 The compositions of the electroless solutions.	41
Table 3-3 Specimen designations of the electroless plating catalyst-assisted CNTs and their deposition conditions.	44
Table 3-4 Suspension designations and their compositions.	46
Table 3-5 Specimen designations of the CNSs-EPD-assisted films and their deposition parameters.	47
Table 5-1 Comparison of the features of the electroless plating catalyst-assisted carbon nanotubes with different catalyst materials.	77



Figure Caption

<p>Fig. 2-1 Eight allotropes of carbon: (a) Diamond, (b) Graphite, (c) Lonsdaleite, (d) C₆₀, (e) C₅₄₀, (f) C₇₀, (g) Amorphous carbon, and (h) Single-walled carbon nanotube [http://en.wikipedia]</p>	3
<p>Fig. 2-2 Ternary ‘phase’ diagram of carbon allotropes. P/H corresponds to the ratio of pentagonal/hexagonal rings [Heinmann 1997-1654]</p>	5
<p>Fig. 2-3 The three structural forms of carbon nanofibers, classified by the angle of the graphene layers/platelets with respect to the filament axis [Rodriguez 1995-3862]</p>	6
<p>Fig. 2-4 Structures of a graphene sheet, single-walled carbon nanotube and multi-walled carbon nanotube [http://www.personal.psu]</p>	7
<p>Fig. 2-5 Potential-energy diagram illustrating the effect of an external electric field on the energy barrier for electrons at a metal surface [Cheng 2003-1021]</p>	8
<p>Fig. 2-6 A prototype 4.5 field emission display fabricated by Samsung using carbon nanotubes [Choi 1999-399]</p>	11
<p>Fig. 2-7 Demonstration of field emission light source using carbon nanotubes as the cathodes [Saito 1998-L346]</p>	11
<p>Fig. 2-8 Nanoelectronic devices. (a) Schematic diagram for a CNT-FET. The semiconducting nanotube, which is on top of an insulating aluminum oxide layer, is connected at both ends to gold electrodes. (b) Scanning tunneling microscope (STM) picture of a SWNT field-effect transistor made using the design of (a) [Bachtold 2001-1317]</p>	12
<p>Fig. 2-9 Use of a MWNT as an AFM tip At the center of the VGCF is a MWNT which forms the tip. The VGCF provides a convenient and robust technique for mounting the MWNT probe for use in a scanning probe instrument [Ajayan 2001-391]</p>	14
<p>Fig. 2-10 SEM micrographs showing growth of carbon nanotube obelisks on an array of submicron nickel dots [Ren 1999-1086]</p>	17
<p>Fig. 2-11 A SEM image of a patterned SiO₂/Si substrate exposed to the precursor. Carbon nanotubes have grown selectively on the SiO₂ patterns, with no observable growth on the Si areas [Zhang 2000-3764]</p>	18
<p>Fig. 2-12 (a) Three stages of AAO pore formation (b) The reactions involved in Al anodization process (c) The size of the pores or their interpore distance versus the applied voltage [Thamide 2002-240; Li 1998-2470; Li 1998-6023]</p>	20
<p>Fig. 2-13 Approaches to carbon nanotube organization: (a) Aligned growth under external forces, (b) Template approaches, (c) Crowding effect, (d) Postgrowth aligned deposition from liquid dispersions, and (e) Epitaxial approaches [Joselevich 2002-1137; Li, 1999-367; Fan 1999-512; Ago 2005-433; Burghard 1998-584]</p>	24

Fig. 3-1 Experimental flowchart for the AAO template-catalyst-assisted process.....	31
Fig. 3-2 Experimental flowchart for the electroless plating catalyst-assisted process.	32
Fig. 3-3 Experimental flowchart for the CNSs-electrophoresis-assisted process.	33
Fig. 3-4 Schematic diagram of the two-step anodization process.	35
Fig. 3-5 Schematic diagram of experimental setup for the Al anodization.	35
Fig. 3-6 Schematic diagram of the ECR-CVD system.	37
Fig. 3-7 The fabrication scheme of the emitter arrays on the AAO-assisted CNSs: (a) preparation of the AAO layer on the Si wafer, (b) CNS growth by ECR-CVD deposition, (c) SiO ₂ dielectric and Al gate electrode depositions on the CNSs, and (d) RIE and BOE etches to open the field-emission area.	38
Fig. 3-8 Schematic diagrams showing the electroless plating catalyst-assisted CNTs grown across trenches of a pattern.	40
Fig. 3-9 Schematic diagram of the MPCVD system.	43
Fig. 3-10 Square-shaped pattern made of Al and SiO ₂ components for EPD process.	45
Fig. 3-11 Schematic diagram of the field emission measurement setup.	50
Fig. 4-1 SEM image of the AAO template after two-step anodization process.	52
Fig. 4-2 Cross-section view of SEM images of the Co-deposited AAO template under different Co electroplating duration: (a) 45, (b) 60, (c) 75, (d) 90, (e) 600 and (f) 1200 s. (For SP. #A2, A3, A4, A5, A7 and A8, respectively.)	53
Fig. 4-3 The curves showing features of morphologies as a function of the Co plating time in AAO template catalyst-assisted process: (a) the deposited Co height in AAO, (b) tube diameter of CNSs, and (c) number density of the CNSs.	54
Fig. 4-4 Top-view SEM images of the as-deposited CNSs under different Co electroplating times: (a) 45, (b) 60, (c) 75 and (d) 90 s. (For SP. # A2, A3, A4 and A5, respectively)	55
Fig. 4-5. Raman spectra of the as-deposited carbon nanostructures under different Co electroplating times. (SP. #A2-5).....	56
Fig. 4-6 Cross-sectional SEM images of the as-deposited CNSs in nanopores of AAO template under different Co electroplating times: (a) 60, (b) 90 and (c) 0 s. (For SP. # A3, A5 and A1, respectively).....	58
Fig. 4-7 TEM images of the Co-assisted CNSs: prepared by different sampling techniques: (a) FIB and (b) ultrasonic agitation. (SP. #A6, and A5, respectively).....	58
Fig. 4-8 HRTEM images of CNFs near the tip under different Co electroplating times: (a) 60 and (b) 90 s. (For SP. # A3 and A5).....	59
Fig. 4-9 Schematic illustration of carbon nanostructure growth mechanism in the AAO pore channel with different Co plating time: (a) 90 s and (b) 60 s, respectively.....	62
Fig. 4-10 (a) J-E curves of the as-deposited AAO-assisted CNSs under different Co electroplating times. (SP. #A2, A3, A4, A5, respectively) and (b) is the F-N plot of the SP. #A3.	64

Fig. 4-11 SEM side view images of the SiO ₂ -coated CNSs for different CNS growth times (a) 30, and (b) 35 min, respectively.	65
Fig. 4-12 SEM images of the SiO ₂ -coated CNSs after RIE etch for (a) 240 s, (b) 300 s, (c) 360 s, (d) 420 s, (e) 480 s and (f) higher magnification of (e). (SP. #A9, A11, A12, A13 and A14 respectively)	66
Fig. 4-13 SEM images of the as-prepared AAO-assisted emitter arrays: (a) top-view of emitters, (b) higher magnification of (a), (c) side-view of (b), and (d) higher magnification of (e), respectively. (SP. #A10).....	67
Fig. 4-14. Raman spectra of (a) the as-deposited CNSs and (b) the as-prepared AAO-assisted emitter arrays. (SP. #A3 and A10).....	68
Fig. 4-15 (a) J-E curve of the AAO-catalyst-assisted CNSs emitter arrays and (b) is its corresponding F-N plot. (SP. #A10).....	69
Fig. 5-1 EDS spectrum of the as-plated Ni catalyst films on a:Si/Si substrate by electroless plating (SP. #B3).....	72
Fig. 5-2 XPS spectra of the as-plated catalyst films on a:Si/Si substrates for different catalyst materials: (a) Co, (b) Fe and (c) Ni. (SP. # B1, B2 and B3, respectively) 73	73
Fig. 5-3 SEM micrographs of nanoparticles after H-plasma pretreatment for different catalyst materials: (a) Co, (b) Fe and (c) Ni. (SP. # B1, B2 and B3, respectively) 74	74
Fig. 5-4 SEM micrographs of the as-deposited CNTs for different catalyst materials: (a) Co, (b) Fe and (c) Ni. (SP. # B1, B2 and B3, respectively)	76
Fig. 5-5 Raman spectra of the as-deposited CNTs for different catalyst materials: (a) Co, (b) Fe and (c) Ni. (SP. # B1, B2 and B3, respectively).	76
Fig. 5-6 TEM micrograph showing morphology of the as-deposited bamboo-like CNT with discrete Ni catalyst particles split from one original particle in the tube. (SP. #B3)	78
Fig. 5-7 HRTEM lattice image of a compartment of the tube around the Ni catalyst. (SP. # B3)	78
Fig. 5-8 (a) Schematic diagram showing the AES analytical positions on the patterned substrate, (b) the corresponding Auger spectra of Ni catalyst at Position 1 or 2, and (c) Position 3, respectively. (SP. #B7)	79
Fig. 5-9 SEM micrographs of the as-deposited CNTs on the substrate patterned by Si ₃ N ₄ /a:Si under different catalyst electroless plating times: (a) 10, (b) 15 (c)20 (d)30 and (e) 60 s. (SP. # B4, B5, B6, B8 and B9, respectively).....	81
Fig. 5-10 (a) and (b) are two typical SEM micrographs of the as-deposited CNTs across trenches of the Ni-coated patterns at two different positions of SP. #B7.	82
Fig. 5-11 I-V curves of the horizontally-oriented CNTs patterns, (a) the as-deposited, and (b) the post-annealed conditions. (SP. #A7).....	82
Fig. 6-1 Raman spectrum of raw SWNTs materials, the inset is the corresponding detail of RBM spectrum.....	84

Fig. 6-2 Pictures of (a) the as-agitated suspensions, and (b) corresponding suspensions after 2 week precipitation. (Suspension designation: S1: SWNTs and D.I. water, S2: SWNTs, SDS and D.I. water, S3: SWNTs, CTAB and D.I. water, and S4: SWNTs and TOPO and butyl alcohol).....	86
Fig. 6-3 UV-Vis absorption spectra of the as-sonicated suspensions (black line) and the corresponding suspensions after 2 weeks precipitation (grey line) for different suspensions: (a) S1, (b) S2, (c) S3 and (d) S4, respectively.....	86
Fig. 6-4 (a) HRTEM image of the SWNT sonicated for 3 hours in SDS aqueous suspension (with schematic inset to show the SDS striations), and (b) the corresponding EDS spectrum.	87
Fig. 6-5 SEM micrographs of the deposited and 3-min-annealed films under same EPD deposition conditions but different post annealing temperatures: (a) 100°C, (b) 200°C, (c) 300°C (SP. #C6, C8 and C11, respectively) and (d) is the corresponding image of (c) at higher magnification.	89
Fig. 6-6 J-E curves of the deposited and annealed films on Al-coated Si substrate under same annealing time (5 min) but different annealing temperatures: (a) as-deposited, (b) 100°C, (c) 200°C and (d) 300°C. (SP. #C5, C7, C9, and C2, respectively)	90
Fig. 6-7 J-E curves of the deposited and annealed films on Al-coated Si substrate under same annealing temperature (300°C) but different annealing times: (a) 1, (b) 3, (c) 5, (d) 10 and (e) 15 min. (SP. #C10, C11, C2, C12 and C13, respectively)	90
Fig. 6-8 SEM morphologies of the EPD-prepared SWNTs pattern made of Al and SiO ₂ coatings: (a) at Al/SiO ₂ interface (with schematic inset to show the interface position on the pattern), and (b) on the Al region of the pattern. (SP. #C15).....	91
Fig. 6-9 (a) SEM morphology of the EPD-deposited film on ITO, (b) is the higher magnification SEM morphologies of the sections marked in (a). (SP. #C16).....	92
Fig. 6-10 Pictures of the EPD-deposited films on Al foil with varies shapes and higher magnification image shown in both (b). (SP. #C17)	92

Chapter 1

Introduction

Intrinsic small dimensions and remarkable unique properties make carbon nanostructures (CNSs) promising building blocks for molecular or nanoscale devices, which may overcome fundamental physical and economic limitations of conventional Si-based VLSI (very large scale integration) fabrication techniques. CNSs need to be assembled into hierarchical arrays over large-scale areas for them to be used as active components (such as transistors or sensing elements), which often need to be interfaced with other device components (such as electrodes). Therefore, how to place the nanotubes at desired locations, directions, and densities for fabricating functional devices has been one of the longstanding unsolved problems of CNS-based nanodevices.

Carbon nanotubes (CNTs) have many desirable properties as a source of field electron emitters, such as high aspect ratio, small radius of curvature, high mechanical strength and chemical stability. Therefore, CNTs have attracted wide interest in the development of field-emission flat panel displays (FED) using them as field emitters. For FED applications, it is necessary to grow vertically aligned CNT arrays on a large area with suitable tube density and tube diameters [Wong 2006-334, Choi 2006-1556, Kim 2005-2084]. The CNTs can behave metallic or semiconducting properties, depending on their rolling helicity or chirality [Lambin 2000-1713, Yamabe 2001-61]. Because of their unique electrical properties and nanoscale dimensions, CNTs are good candidates for nanoscale electronic devices. For example, CNTs have been used as circuit components to be modulated to generate carbon nanotube field-effect transistors (CNT-FETs) [Fuhrer 2000-494, Rochefort 2001-2521, Han 2001-5731]. However, until now the industrial application of CNTs for electronic devices has not been realized because of difficulty in the

assembly and integration with the well-established silicon IC technology. Therefore, it would be desirable from both scientific and technological points of view to control not only the size and chirality of CNTs, but also their position and orientation. Single-walled carbon nanotubes (SWNTs) have many potential applications in nanoscale devices but it remains a challenge to uniformly disperse SWNTs for their applications, because as-synthesized SWNTs generally exist as tube bundles or aggregates bound tightly by strong Van der Waals attractions between tubes. There are some methods have been proposed by using both organic and aqueous media as solvents ^[Hilding 2003-1, Du 2005-548], functionalizing the tubes ^[Marsh 2007-5490] and adding surfactants ^[Islam 2003-269, Kim 2006-1541].

The goal of this study is to develop nanofabrication processed to manipulate the CNSs patterns and to examine the structures and properties. The developed processes include the AAO template-catalyst-assisted, electroless plating catalyst-assisted, and CNSs-electrophoresis-assisted methods. The experimental flowcharts, the detail experimental procedures and structure-property-analyses methods for each process will be illustrated in the Chapter 3. The results and discussion of the AAO template-catalyst-assisted, electroless plating catalyst-assisted, and CNSs-electrophoresis-assisted processes will be presented in the Chapter 4, 5 and 6, respectively. Chapter 7 summarizes the results of these three processes, while Chapter 8 provides directions for future research.

Chapter 2

Literature Review

2.1 Overview of the CNSs

Carbon, a group IV element like Si, is associated with a rich and diverse chemistry. However, a new era in carbon materials began when in the mid-1980s the family of buckminsterfullerenes (“buckyballs”) was discovered [Kroto 1985-162] and followed by the discovery of fullerene nanotubules (“buckytubes”) [Iijima 1991-56]. The discovery of these structures set in motion a new world-wide research boom that seems still to be growing. The entire range of dimensionalities is represented in the nanocarbon world, beginning with zero

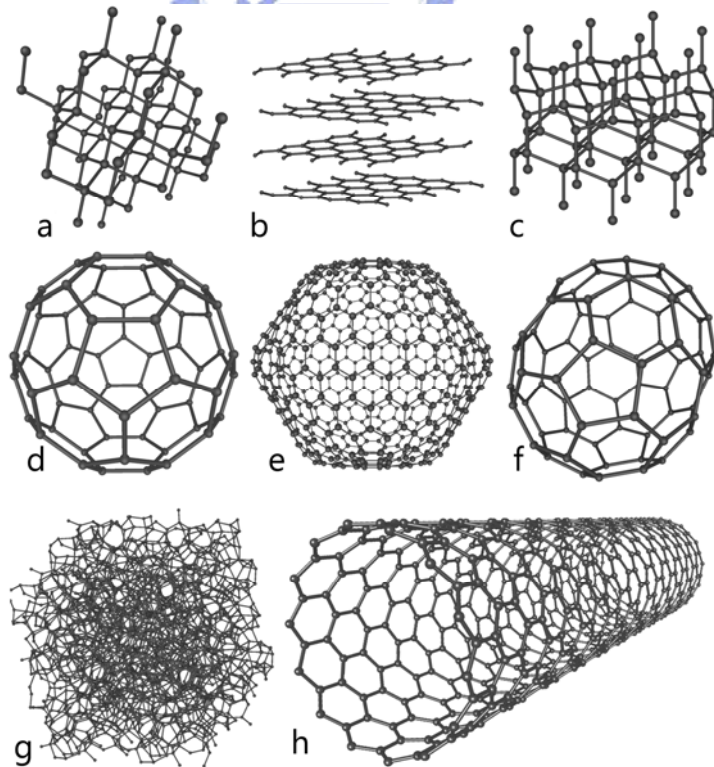


Fig. 2-1 Eight allotropes of carbon: (a) Diamond, (b) Graphite, (c) Lonsdaleite, (d) C₆₀, (e) C₅₄₀, (f) C₇₀, (g) Amorphous carbon, and (h) Single-walled carbon nanotube <http://en.wikipedia>.

dimension structures (fullerenes, diamond clusters) and includes one-dimensional structures (nanotubes), two-dimensional structures (graphene), and three-dimensional structures (nanocrystalline diamond, fullerite). Eight allotropes of carbon: (a) diamond, (b) graphite, (c) lonsdaleite (hexagonal diamond), (d) C₆₀ (Buckminsterfullerene or buckyball), (e) C₅₄₀, (f) C₇₀, (g) amorphous carbon, and (h) single-walled carbon nanotube (SWNT or buckytube) are shown in Fig. 2-1 [\[http://en.wikipedia\]](http://en.wikipedia).

An interesting discussion of carbon allotropy and a scheme for classifying existing carbon forms is proposed ^[Heinmann 1997-1654]. The classification scheme is based on the types of chemical bonds in carbon, with each valence state corresponding to a certain form of a simple substance. Elemental carbon exists in three bonding states corresponding to sp³, sp², and sp hybridization of the atomic orbitals, and the corresponding three carbon allotropes with an integer degree of carbon bond hybridization are diamond, graphite, and carbyne. All other carbon forms constitute so-called transitional forms that can be divided to two big groups. The first group comprises mixed short-range order carbon forms of more or less arranged carbon atoms of different hybridization states, for example, diamond-like carbon, vitreous carbon, soot, carbon blacks, etc., as well as numerous hypothetical structures like graphynes and ‘superdiamond’. The second group includes intermediate carbon forms with a non-integer degree of carbon bond hybridization, spⁿ. The subgroup with 1 < n < 2 includes various monocyclic carbon structures. For 2 < n < 3, the intermediate carbon forms comprise closed-shell carbon structures such as fullerenes (the degree of hybridization in C₆₀ is ~ 2.28 ^[Haddon 1993-53]), carbon onions and nanotubes, hypothetical tori, etc. The fractional degree of hybridization in this group of carbon structures is due to the curvature of the framework. A tentative ternary carbon allotropy diagram based on carbon valence bond hybridization is shown in Fig. 2-2. The value of the suggested scheme is that any form of carbon substance is included in the classification.

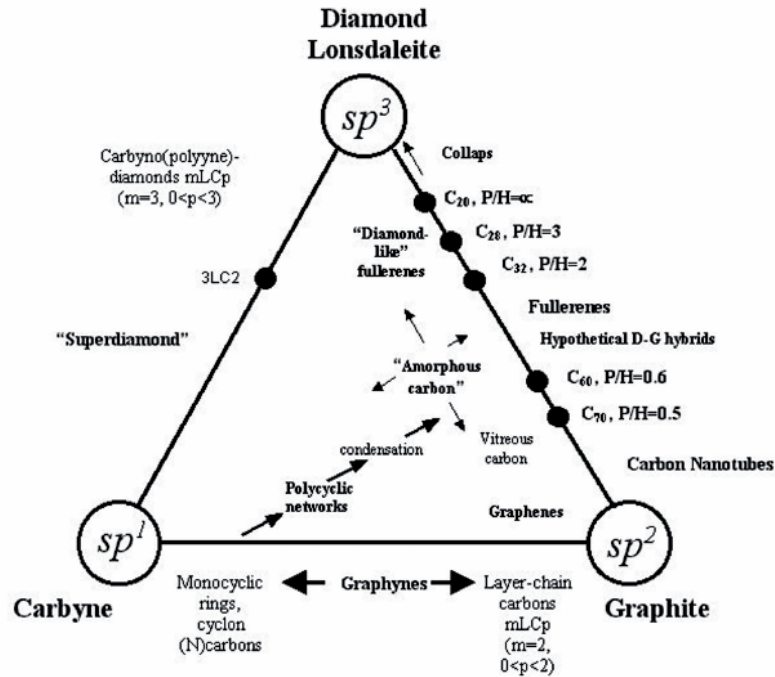


Fig. 2-2 Ternary 'phase' diagram of carbon allotropes. P/H corresponds to the ratio of pentagonal/hexagonal rings [Heinmann 1997-1654]

Carbon filaments have been found, most often by accident, inside furnaces containing hydrocarbon gases or carbon monoxide, as reported by several authors as far back as 50 years ago. These filaments, which are typically several nanometers in diameter and several micrometers long, have a tubular microstructure and are conventionally referred to as vapor-grown carbon fibers (VGCFs). CNTs or buckytubes can be considered as a derivative of both the carbon fibers and fullerenes. However, the main difference between CNTs and carbon nanofibers (CNFs) consists in the lack of a hollow cavity for the latter. There are mainly three types of CNFs which differ for the disposition of the graphene layers: in ribbon-like CNF the graphene layers are parallel to the growth axis, the platelet CNF display graphene layers perpendicular to the growth axis and finally herringbone CNF have layers stacked obliquely in respect to the growth axis (see Fig. 2-3) [Rodriguez 1995-3862]. The diameters of CNF are generally higher than the ones presented by nanotubes and can easily reach 500 nm.

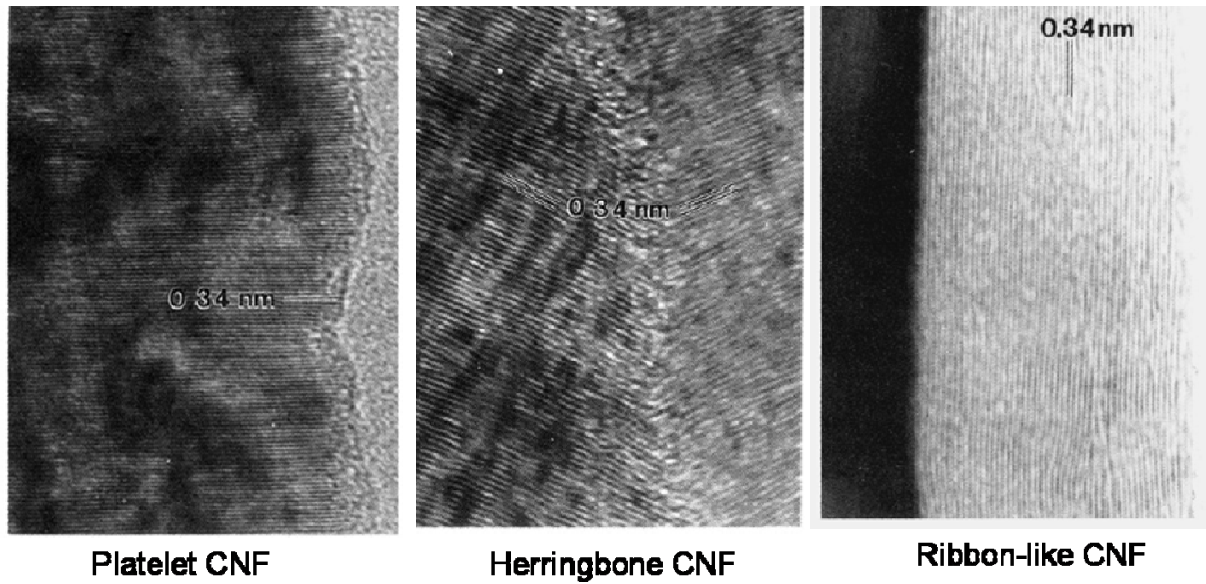


Fig. 2-3 The three structural forms of carbon nanofibers, classified by the angle of the graphene layers/platelets with respect to the filament axis [Rodriguez 1995-3862].

Since CNTs were discovered by Iijima in 1991 [Iijima 1991-56], their synthesis methods, structures and properties have been studied and CNTs can be divided essentially into two categories: SWNT and multi-walled carbon nanotube (MWNT) as displayed in Fig. 2-4. Ideally, a SWNT is made of a perfect graphene sheet, i.e. a polyaromatic mono-atomic layer made of a hexagonal display of sp^2 hybridized carbon atoms that genuine graphite is built up with, rolled up into a cylinder and closed by two caps (semi-fullerenes). The internal diameter of these structures can vary between 0.4 and 2.5 nm and the length ranges from few microns to several millimeters. MWNT can be considered as concentric SWNT with increasing diameter and coaxially disposed. The number of walls present can vary from two (double wall nanotubes) to several tens, so that the external diameter can reach 100 nm. The concentric walls are regularly spaced by 0.34 nm similar to the intergraphene distance evidenced in turbostratic graphite materials.

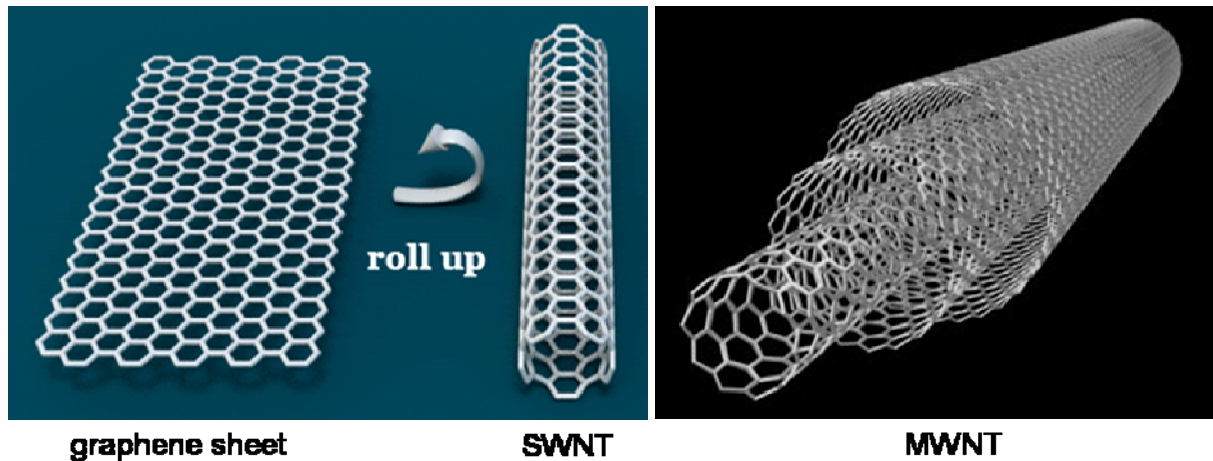


Fig. 2-4 Structures of a graphene sheet, single-walled carbon nanotube and multi-walled carbon nanotube ^[<http://www.personal.psu.edu>].

2.2 Applications of the CNSs

In the past decade, a significant amount of work has been done on the CNSs to reveal their unique structural, mechanical, chemical and electronic properties and many potential applications have been proposed, including field emission display, conductive or high-strength composites, nanometer sized device, sensors and probes, energy storage, interconnect and drug delivery. Some of these applications are now realize in products and others are demonstrated in early to advanced devices. The applications and related properties were classified and described as follows.

(a) Field emission Devices

Electron field emission is a quantum process where, under a sufficiently high external electrical field, electrons can escape from the metal surface to the vacuum level by tunneling. The basic physics of field emission is summarized by the Fowler-Nordheim equation, which states that the emission current increases exponentially with increasing electric field. When a sufficient electric field is applied on the emitter surface as shown schematically in Fig. 2-5 [Cheng 2003-1021], electrons will tunnel through the surface-potential barrier across the metal-vacuum interface and escape from the emitter surface, even under a very low

temperature. This potential barrier is called the work function which corresponds to the potential difference between Fermi level (E_F , energy level of the free electrons) of the emitter and the field-free vacuum. Work function (ϕ) is a surface property of material and correlates with the electronic structure and orientation of the crystal plane. For an atomically smooth molybdenum surface, the work function is 4.36 eV for the (112) plane and 4.95 eV for the (110) plane. In order to obtain high emission currents at low voltages, one desires to have an as low as possible work function and the carbon has a low work function about 5 eV [CRC 2008-12.]. Besides, CNTs have others desirable properties as a source of field electron emitters, such as high aspect ratio, small radius of curvature, high electrical conductivity, high mechanical strength, and chemical stability.

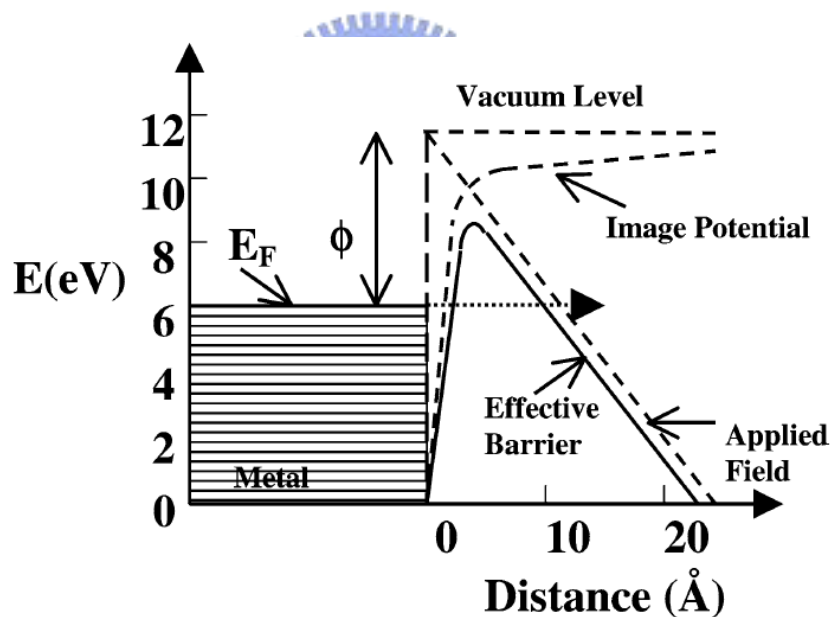


Fig. 2-5 Potential-energy diagram illustrating the effect of an external electric field on the energy barrier for electrons at a metal surface [Cheng 2003-1021].

The potential barrier is square when no electric field is present. If an external electric field is applied, the potential barrier at the surface becomes thinner and the vacuum energy level is reduced as shown schematically in Fig. 2-17 [Cheng 2003-1021]. The top of the barrier is rounded due to image force. The decrease in barrier width allows the electrons having energy

less than vacuum level to tunnel through. The decrease in barrier height ($\Delta\phi$) can be described by the following relation:

$$\Delta\phi = \left(\frac{qE}{4\pi\epsilon_0} \right)^{1/2} \quad (2.1)$$

where ϕ is the work function, E is the applied electric field, q is electron charge, and ϵ_0 is permittivity of free space. The applied electric field decisively affects the barrier height and thus the emitted current. Fowler and Nordheim ^[Fowler 1928-173] in 1928 derived a relationship between the field-emission current density (J) from a pure metal and the applied electric field. The widely quoted Fowler-Nordheim (F-N) equation can be expressed as ^[Fowler 1928-173]

$$J = \frac{AE^2}{\phi t^2(y)} \exp \left[-\frac{B\phi^{3/2}v(y)}{E} \right] \quad (2.2)$$

where $A = 1.54 \times 10^{-6}$ (A V⁻² eV), $B = 6.83 \times 10^7$ (V eV^{-3/2} m⁻¹), $y = 3.7947 \times 10^{-4} E^{1/2} / \phi$, $t^2(y) \sim 1.1$, and $v(y)$ can be approximated as

$$v(y) = \cos(0.5\pi y) \text{ or } v(y) = 0.95 - y^2 \quad (2.3)$$

Generally, the field emission current (I) is measured as a function of the applied voltage (V). Substituting relationships of $J = I/\alpha$ and $E = \beta V/d$ into Equation (2), where α is the emitting area, β is the local field enhancement factor at the emitting surface, and d is the distance between cathode and anode, following equation can be obtained:

$$I = \frac{A\alpha\beta^2V^2}{d^2\phi t^2(y)} \exp \left[-\frac{Bd\phi^{3/2}v(y)}{\beta V} \right] \quad (2.4)$$

In addition, the Napierian logarithm form of Equation (2.4) can be expressed as

$$\ln\left(\frac{I}{V^2}\right) = \ln\left[\frac{A\alpha\beta^2}{d^2\phi t^2(y)}\right] - \frac{Bd\phi^{3/2}v(y)}{\beta V} \quad (2.5)$$

using $v(y) \sim 1$ in Equation (2.16), it gives

$$\ln\left(\frac{I}{V^2}\right) = \ln\left[\frac{A\alpha\beta^2}{d^2\varphi t^2(y)}\right] - \frac{Bd\varphi^{3/2}}{\beta V} \quad (2.6)$$

Here, a plot of $\ln(I/V^2)$ versus $1/V$ yields a linear curve. This plot is the well known F-N plot.

From Equation (2.6), the slope (S) of the F-N plot is given by

$$S = -\frac{Bd\varphi^{3/2}}{\beta} \quad (2.7)$$

The value of field enhancement factor can be estimated from the slope of the measured F-N curve if the work function of the emitter is known. All the field emission sources rely on the field enhancement due to sharp tips or high aspect ratio of protrusions, so emitters tend to have smaller virtual source sizes because of the primary role of the β factor. The larger the β , the higher the field concentration, and therefore the lower the effective threshold voltage for emission. For a thin cylinder, the β value is roughly proportional to the height-diameter ratio (aspect ratio) [Utsumi 1991-2276]. For electron emission to occur, the electric field at the emitting surface must be on the order of 1-3 V/nm, which at reasonable applied voltages requires larger values of β . It should be noted that the F-N model is valid only for flat metal surfaces at 0 K, and is in many case not satisfactory. However, the model is simple and widely used. One can only hope that efforts that aim to extend the model or to develop numerical approaches will soon supplement it.

Research on field emission properties using carbon nanostructures have been investigate extensively such as field emission electron sources [De Heer 1995-270] for flat panel displays [Lee 2001-265.], lamps [Saito 2000-169], gas discharge tubes providing surge protection [Rosen 2000-1668], and X-ray [Sugie 2001-2578] generators and microwave amplifiers [Brodie 1992-395]. Flat panel displays are one of the more lucrative applications of carbon nanotubes but are also the most technically complex. Nanotubes are at an advantage over liquid crystal displays since they have low power consumption, high brightness, a wide viewing angle, a fast response rate and a wide operating system. A 4.5 inch diode-type field emission display has been fabricated by

Samsung (Fig. 2-6), with SWNT stripes on the cathode and phosphor-coated ITO stripes on the anode running orthogonally to the cathode stripes [Choi 1999-399].

Cathode ray lighting elements with carbon nanotube materials as the field emitters have been fabricated by Ise Electronic Co. in Japan [Saito 1998-L348]. As illustrated in Fig. 2-7, these nanotube-based lighting elements have a triode-type design.



Fig. 2-6 A prototype 4.5 field emission display fabricated by Samsung using carbon nanotubes [Choi 1999-399].

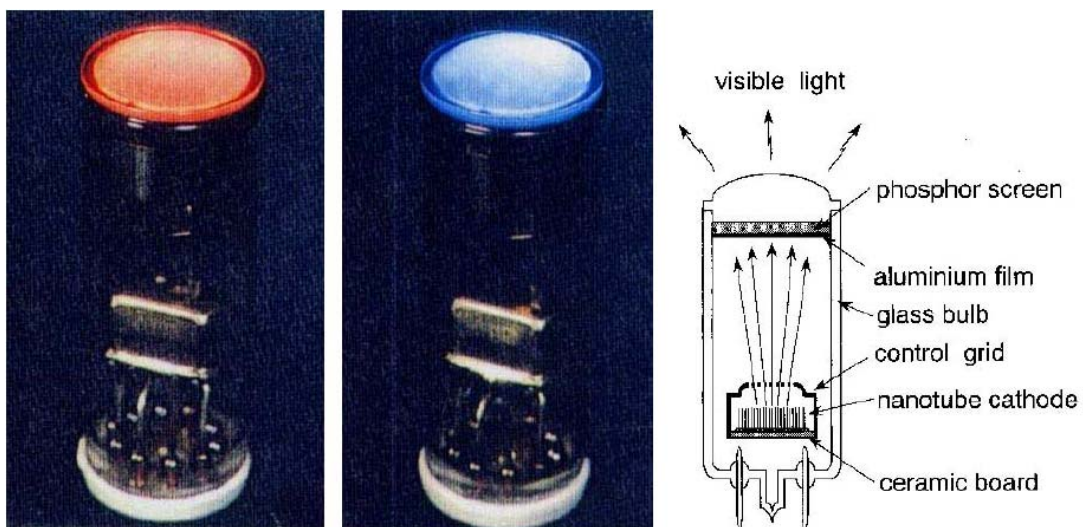


Fig. 2-7 Demonstration of field emission light source using carbon nanotubes as the cathodes [Saito 1998-L346].

(b) Nanometer sized device

Electronic circuits cannot continue to shrink by orders of magnitude and provide corresponding increases in computational power, unless radically different device materials, architectures, and assembly processes are developed. Dramatic recent advances have fueled speculation that nanotubes will be useful for downsizing circuit dimensions. Research toward nanoscopic CNT-FETs aims to replace the source-drain channel structure with a nanotube. A more radical approach is to construct entire electronic circuits from interconnected nanotubes. Because the electronic properties depend on helicity, it should be possible to produce a diode, for example, by grafting a metallic nanotube to a semiconducting nanotube. As shown in Fig. 2-8, Bachtold et al. ^[Bachtold 2001-1317] reported a nanotube transistor using integrated nanotubes which may lead to large scale integration.

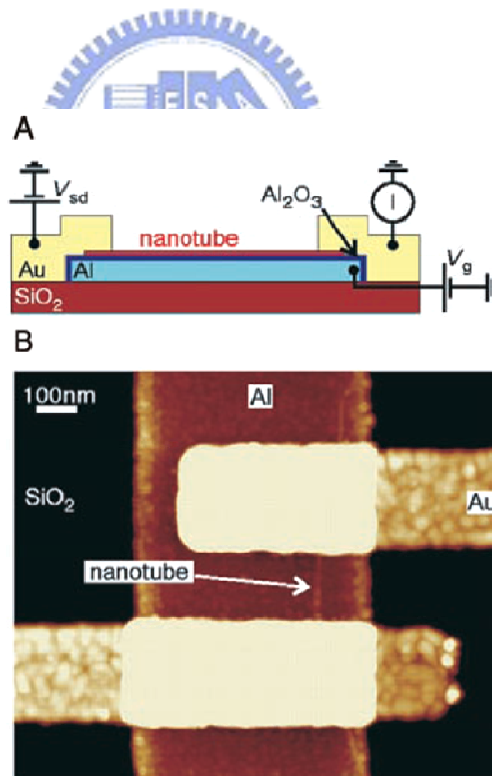


Fig. 2-8 Nanoelectronic devices. (a) Schematic diagram for a CNT-FET. The semiconducting nanotube, which is on top of an insulating aluminum oxide layer, is connected at both ends to gold electrodes. (b) Scanning tunneling microscope (STM) picture of a SWNT field-effect transistor made using the design of (a) ^[Bachtold 2001-1317].

(c) Sensors

CNTs have some advantages for sensing applications such as their small size with larger surface; high sensitivity, fast response and good reversibility at room temperature enable them as a gas molecule sensor; enhanced electron transfer when used as electrodes in electrochemical reactions; and easy protein immobilization with retention of activity as potential biosensors are among some of the desirable applications. The main advantage of these sensors are the nanoscopic size of the nanotube sensing element and the corresponding nanoscopic size of the material required for a response [Baugham 2002-787].

The electrical resistivity of SWNTs has been found to change sensitively on exposure to gaseous ambients containing NO₂, NH₃, and O₂. By monitoring this change the presence of gases could be detected. Results showed are at least an order of magnitude faster than those currently available and that they could be operated at room temperature or at higher temperatures for sensing applications [Ajayan 2001-391].

(d) Probes

With extremely small sizes, high conductivity, high mechanical strength and flexibility (ability to easily bend elastically), nanotubes may ultimately become indispensable in their use as nanoprobes. The mechanical robustness of the nanotubes and the low buckling force increase the probe life along and minimizes damage during repeated hard crashes into substrates [Wang 2001-883]. The cylindrical shape and small tube diameter also allow for imaging in narrow deep crevices and improve resolution in comparison to conventional nanoprobes, especially for high sample feature heights [Hafner 1999-761]. Since MWNTs are conducting they can be used as scanning probes on microscope tips in instruments such as a STM, atomic force microscope (AFM) and electrostatic force microscopes (Fig. 2-9).

On an AFM tip they can be controlled like tweezers to pick up and release nanoscale structures. Nanoscopic tweezers have been made that are driven by the electrostatic interaction between two nanotubes on a probe tip [Kim 1999-2148]. They may be used as

nanoprobes for assembly. These uses may not have drastically impact of other commercial applications, however they increase the value of measurement systems for characterization and manipulation on the nanometer scale.

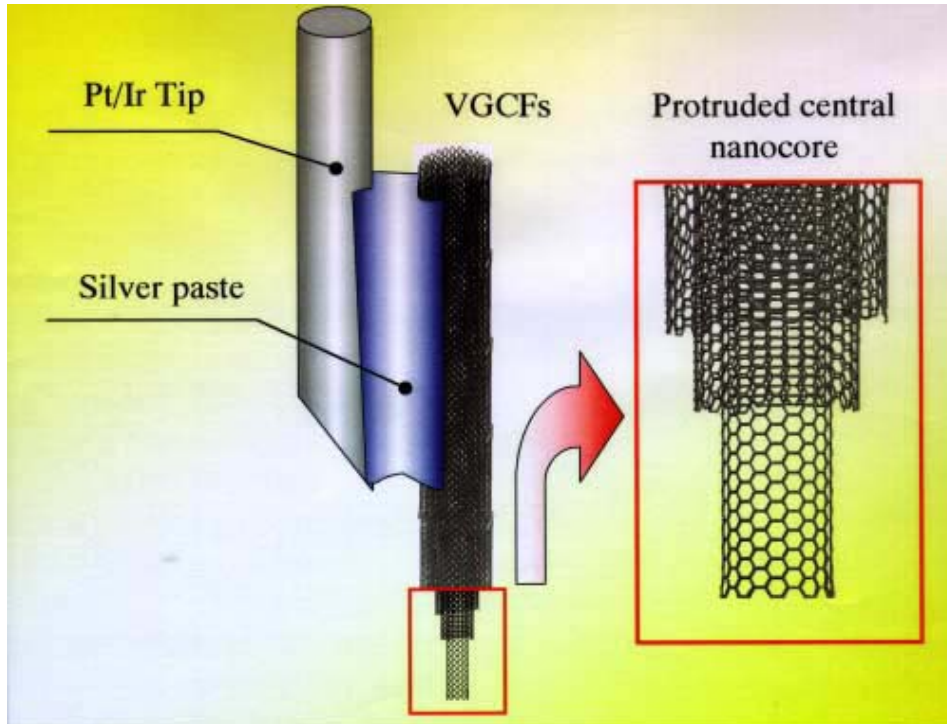


Fig. 2-9 Use of a MWNT as an AFM tip At the center of the VGCF is a MWNT which forms the tip. The VGCF provides a convenient and robust technique for mounting the MWNT probe for use in a scanning probe instrument [Ajayan 2001-391].

(e) Energy storage

Graphite, carbonaceous materials and carbon fiber electrodes have been used for decades in fuel cells, batteries and several other electrochemical applications. Carbon nanotubes are now being considered for energy storage and production because of their small dimensions, a smooth surface topology, and perfect surface specificity since only the graphite planes are exposed in their structure.

Fuel cells will most likely be the energy source of the future, for vehicles, local off-grid power supply, and power sources for small and handheld electronic devices. Pure MWNTs

and MWNTs deposited with metal catalysts (Pd, Pt, Ag) have been used to electro-catalyze an oxygen reduction reaction, which is important for fuel cells [Britto 1999-154, Che 1998-346, Planeix 1994-7935]. It is seen from several studies that nanotubes could be excellent replacements for conventional carbon-based electrodes.

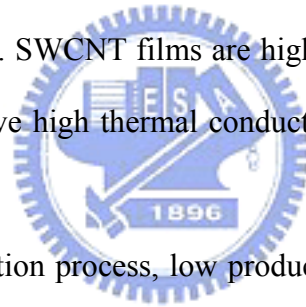
The basic working mechanism of rechargeable lithium batteries is electrochemical intercalation and de-intercalation of lithium between two working electrodes. MWNTs consist of more than two graphitic sheets rolled into closed and concentric 1D cylinders. The graphitic sheets have an inter-planar spacing of ca. 0.34 nm, which allows the intercalation/deintercalation of Li ions. Several different approaches have been used to incorporate MWCNTs as the anode material in Li-ion batteries [Yang 2001-7, Yang 2005-347, Claye 2000-2845]. The MWNT-based batteries show reversible capacities of 80– 540 mAh g⁻¹ and very high irreversible capacities. As a result, there has been much recent effort devoted to improving these capacities and the Coulombic efficiency to meet the power requirements of microelectronic and telecommunication devices.

The area of hydrogen storage in CNTs remains active and controversial. Extraordinarily high and reversible hydrogen adsorption in SWNT containing materials [Dillon 1997-377, Chen-1999-91, Liu 1999-1127, Nutenadel 1999-30] has been reported and has attracted considerable interest in both academia and industry. However, many of these reports have not been independently verified. There is also a lack of understanding of the basic mechanism(s) of hydrogen storage in these materials.

(f) Photovoltaic application

Organic photovoltaic devices (OPVs) are fabricated from thin films of organic semiconductors, such as polymers and small-molecule compounds, and are typically on the order of 100 nm thick. Combining the physical and chemical characteristics of conjugated polymers with the high conductivity along the tube axis of CNTs provides a great deal of incentive to disperse CNTs into the photoactive layer in order to obtain more efficient OPV

devices [Miller 2006-133117, Ago 1999-1281, Miller 2006-123115, Miller 2007 -023105]. The interpenetrating bulk donor–acceptor heterojunction in these devices can achieve charge separation and collection because of the existence of a bicontinuous network. Along this network, electrons and holes can travel toward their respective contacts through the electron acceptor and the polymer hole donor. Photovoltaic efficiency enhancement is proposed to be due to the introduction of internal polymer/nanotube junctions within the polymer matrix. The high electric field at these junctions can split up the excitons, while the SWNT can act as a pathway for the electrons. Another benefit is that SWCNT films exhibit a high optical transparency in a broad spectral range from the UV-visual far into the near IR range. Only a few materials retain reasonable transparency in the infrared spectrum while maintaining transparency in the visible part of the spectrum as well as acceptable overall electrical conductivity, so CNTs could be used as a transparent electrode. SWCNT films are highly flexible, do not creep, do not crack after bending, theoretically have high thermal conductivities to tolerate heat dissipation, and have high radiation resistance.



Due to the simple fabrication process, low production cost, and high efficiency, there is significant interest in dye-sensitized solar cells (DSSCs). With recent progress in CNT development and fabrication [Kongkanand 2007-676, Jang 2004-9807, Lee 2007-513115], there is promise to use various CNT based nanocomposites and nanostructures to direct the flow of photogenerated electrons and assist in charge injection and extraction. To assist the electron transport to the collecting electrode surface in a DSSC, a popular concept is to utilize CNT networks as support to anchor light harvesting semiconductor particles. Other researchers fabricated DSSCs using the sol-gel method to obtain titanium dioxide coated MWNTs for use as an electrode. Because pristine MWNTs have a hydrophobic surface and poor dispersion stability, pretreatment was necessary for this application

2.3 Selective deposition methods for the nanostructures

(a) Patterning by photo- or electron-beam lithography

In most selective deposition process, the location of CNSs is defined by patterning the catalyst materials or substrates using photo- or electron-beam lithography. Growth of a single freestanding MWNTs on each nano-nickle dot was first proposed by Ren's group. [Ren 1999-1086] As known in Fig. 2-10, they fabricated the array of individual MWNTs onto a grid of patterned nickel to investigate array of MWNTs for applications of flat panel field emission displays. Using the similar idea of constructing periodic arrays of nickel dots prepared by polystyrene nanosphere lithography was reported by Huang's group. Patterned CNTs were fabricated by pre-patterning catalysts on the substrate depending on lithography technique. The idea of the substrate-dependent site-selective growth of aligned CNTs on the SiO₂/Si was reported by Zhang's group by using the precursors of ferrosene and xylene, as shown in Fig. 2-11 [Zhang 2000-3764]. Later, the method continues to arrange into well-defined configuration in order to build integrated system by Wei's group by using pre-patterning the SiO₂/Si substrate [Wei 2000-3586].

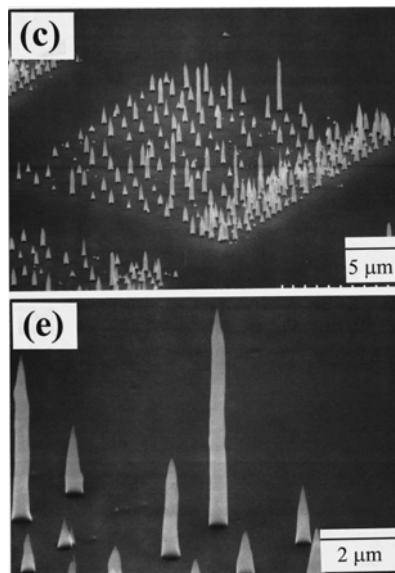


Fig. 2-10 SEM micrographs showing growth of carbon nanotube obelisks on an array of submicron nickel dots [Ren 1999-1086].

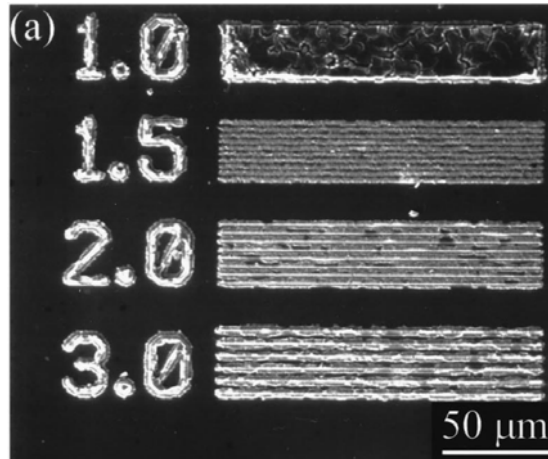


Fig. 2-11 A SEM image of a patterned SiO₂/Si substrate exposed to the precursor. Carbon nanotubes have grown selectively on the SiO₂ patterns, with no observable growth on the Si areas [Zhang 2000-3764].

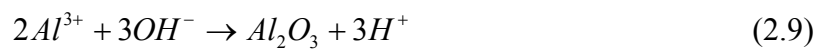
(b) Template-based method

Porous structures such as zeolite [Hernadi 1996-416], anodic aluminum oxide (AAO) or porous Si are often used as the template for nanostructures. AAO has advantages of the uniform pore diameter, highly ordered pore arrangement, high packing density, low cost ... are often used as templates, stencils, or masks, a number of approaches for fabricating a variety of nano-superstructures. The structure of the AAO consists of close-packed hexagonal cells, each with a straight pore channel perpendicular to the aluminum substrate and a thin Al₂O₃ barrier layer lies adjacent to the aluminum substrate with a hemispherical, scalloped geometry at the pore bottom. The porous oxide growth consists of three stages that can be identified by the characteristic behavior of current versus time for potentiostatic anodization or potential versus time for galvanostatic anodization. These stages of pore formation are schematically shown in Fig. 2-12(a). When an anodic voltage is applied, the current decreases linearly with time, implying a linear increase in resistance or a linear growth of aluminum oxide on the surface of aluminum and high-resistance oxide (stage I). Tiny cracks appear at the oxide/electrolyte interface and they widen to form pores (stage II). Further anodization causes the pores to accelerate and attain a constant dissolution speed (stage III) [Thamide 2002-240].

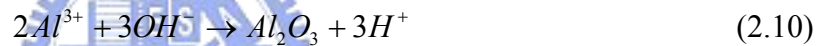
The reactions involved in Al anodization process are described in Fig. 2-12(b). When aluminum is oxidized to alumina, the oxidation takes place at the entire metal/oxide interface, aluminum ions are formed due to charge transfer or electrochemical reaction:



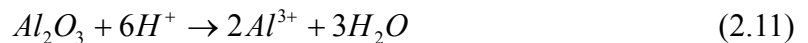
The metal/oxide interface moves away from the interface of the electrolyte and the oxide was due to interaction of diffusing oxygen species with aluminum ions produced anodically at the Al_2O_3/Al interface:



At the oxide/electrolyte interface, aluminum oxide grows according to the outward migration of aluminum ions (mainly by a place-exchange mechanism) and their reaction with oxygen-containing electrolyte species:



This aluminum oxide is also dissolved as a result of field-stimulated interaction of electrolyte species with the oxide surface:



The oxide/electrolyte and metal/oxide interface are moving boundaries and the local electric field is the key variable along the interfaces that determines the reaction rate or speed of the interface ^[Li 1998-2470].

A number of researches have been reported that the geometric dimension and size of these pores are strongly related to the anodizing conditions (applied voltage, acid concentration of the electrolyte, and temperature). Most of these experimental data were obtained for sulfuric, oxalic, and phosphoric acids in the range of $0 < \text{pH} < 1$ and with the applied voltage of 20–160 volts. Fig. 2-12(c) shows that the size of the pores or their interpore distance could be varied linearly with the applied voltage and the thickness of the porous

oxide film could be also controlled by the anodization time [Li 1998-6023].

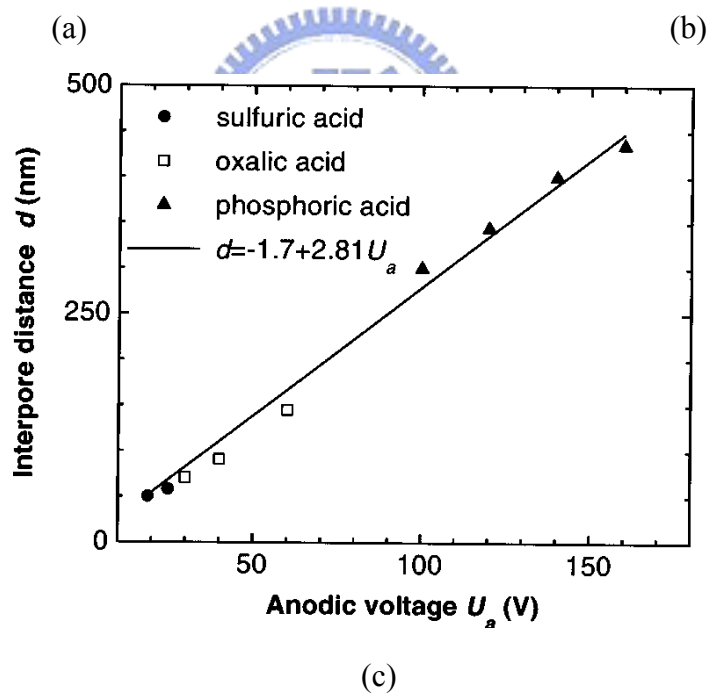
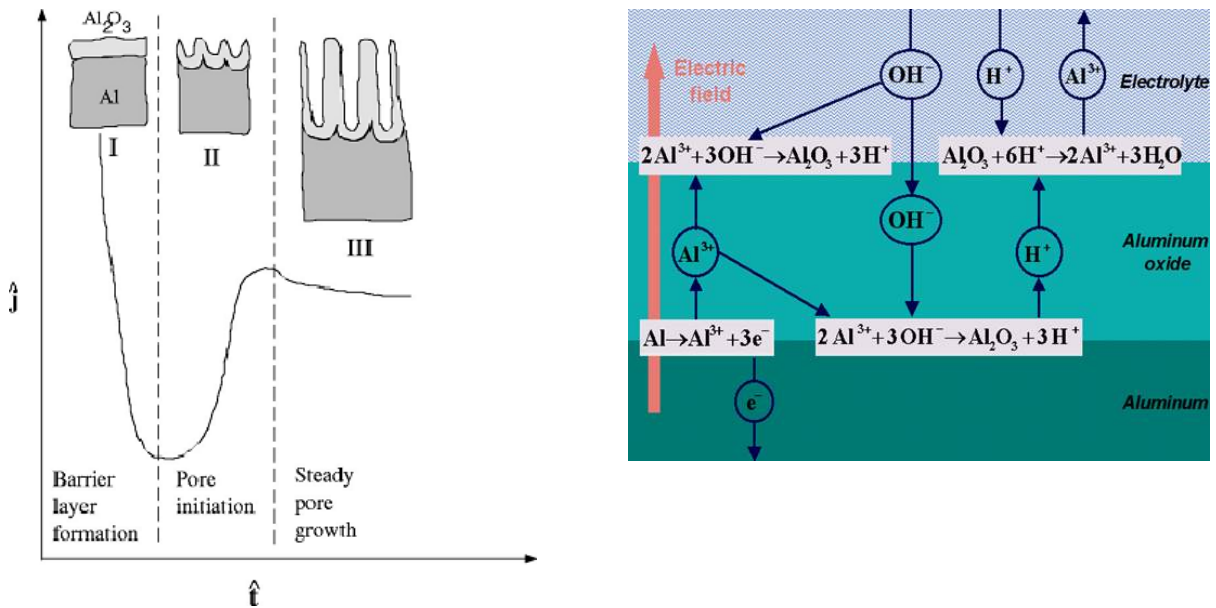


Fig. 2-12 (a) Three stages of AAO pore formation (b) The reactions involved in Al anodization process (c) The size of the pores or their interpore distance versus the applied voltage [Thamide 2002-240; Li 1998-2470; Li 1998-6023].

(c) Electrophoretic deposition (EPD)

EPD [Boccaccini 2006-3149] is a colloidal process wherein a direct current (DC) electric field is

applied across a stable suspension of charged particles attracting them to an oppositely charged electrode. One electrode (cathode) consists of the substrate to coat, the anode being either an aluminum foil or stainless steel. The thickness of the coating depends on the distance between the two electrodes, the voltage (can vary from 10 to 300 V), the properties of the suspension (e.g. pH) and the duration.

(d) Self-assembly

Self-assembly is a term used to describe processes in which a disordered system of pre-existing components forms an organized structure or pattern as a consequence of specific, local interactions among the components themselves, without external direction. Self-assembly can be classified as either static or dynamic. In static self-assembly, the ordered state forms as a system approaches equilibrium, reducing its free energy. However in dynamic self-assembly, patterns of pre-existing components organized by specific local interactions are not commonly described as "self-assembled" by scientists in the associated disciplines. These structures are better described as "self-organized".

(e) Electroless plating

Electroless (autocatalytic) plating involves the presence of a chemical reducing agent in solution to reduce metallic ions to the metal state. There are no external electrodes present, but there is electric current (charge transfer) involved. Instead of an anode, the metal is supplied by the metal salt; replenishment is achieved by either adding salt or an external loop with an anode, of the corresponding metal, that has higher efficiency than the cathode. There is therefore, instead of a cathode to reduce the metal, a substrate serving as the cathode, while the electrons are provided by a reducing agent. The process takes place only on catalytic surfaces rather than throughout the solution (if the process is not properly controlled, the reduction can take place throughout the solution, possibly on particles of dust or of catalytic metals, with undesirable results).

The electroless process involves a continuous buildup of metal coating on a substrate by

the mere immersion in a suitable aqueous solution. A chemical reducing agent in solution supplies the electrons for converting metal ions to the metal form.



The important point is that the catalytic surface is the only place where this simplified reaction occurs. Once the deposition starts on a surface, the deposited metal must also be catalytic for the deposition to continue. The progress of electroless deposition is linear in time. As deposition progresses, islands are formed around these nucleation sites. These islands grow in size until they merge and a continuous film results. It was also established that the film mass thickness growth rate in electroless deposition is linear in time once film continuity has been reached. The mass thickness of a deposit is the deposited film's volume per unit area. This thickness factor refers to the total material deposited as a continuous film of even thickness, and it is compared to electrodeposition under conditions of constant current density.

(f) Electroplating

For the electroplating process an electrical current is used to coat a substrate or to fill a mould with a metal or an alloy on a conductive substrate. The substrate to be plated is the negative electrode, the cathode, as it is called. The positive electrode is the anode made from the material to be plated on the cathode. Anode and cathode are connected to an external power supply. The electrodes are immersed in a solution called electrolyte containing metallic ions. If a current is applied the ions will conduct the current. The positively charged ions are transported by the field lines to the cathode where they are reduced to metal by the electrons of the cathode. If the electrolyte contains metallic ions being different from the material of the anode an alloy will be deposit. At the cathode the chemical reaction is given as:

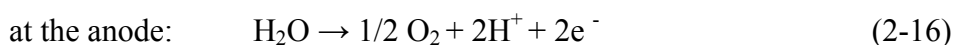
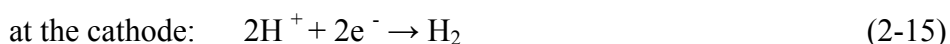


The anode dissolves and provides the metallic ions. The dissolution reaction is as follows:



The overall chemical processes are described by the chemical reaction given as (in acidic

solutions):



The hydrogen gas is an unfavourable product because it is incorporated in the deposited material and reduces its quality.

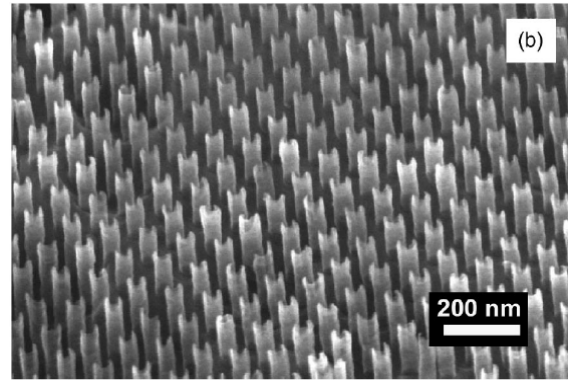
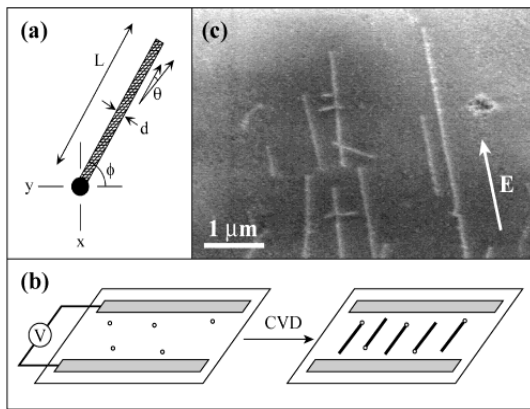
2.4 Fabrication methods for the oriented CNSs

(a) Aligned growth under external forces

Directed assembly under external forces such as by flow and electric fields^[Huang 2003-1651, Chen 2001-3714, Zhang 2001-3155]. In particular, the approach using electric-field assisted assembly has been actively explored as a viable integration strategy for lateral alignment of CNTs. The use of electric field can be applied postgrowth^[Krupke 2003-1019, Nagahara, I. 2002-3826] or during growth^[Ural 2002-3464, Joselevich 2002-1137]. In the Fig. 2-13(a), the growth is defined by patterning the catalyst nanoparticles, while the direction of growth is defined by a local electric field parallel to the substrate. Statistical analysis of the nanotube angular distribution indicates that field-directed growth can discriminate between metallic and semiconducting nanotubes during their formation^[Joselevich 2002-1137].

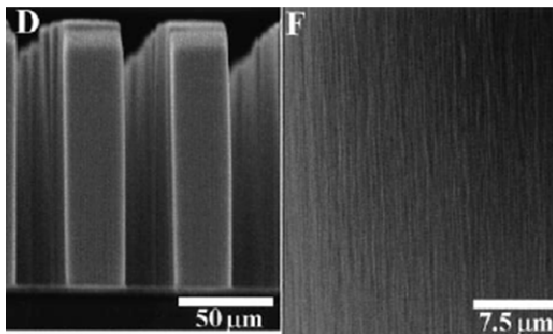
(b) Template approaches

Another method of aligned growth of nanostructures is to use a nanoporous template. In this method, porous alumina produced in an aluminum anodization process is used as a template for nanotube growth. The anodic alumina has a porous structure with nanopores (30–50 nm) self-organized in a hexagonal pattern. Catalyst is electrodeposited into the nanopores and then nanotubes are synthesized by CVD. The porous template may be etched away after nanotube synthesis. An array of aligned nanotubes prepared using this fabrication process is shown in Fig. 2-13(b)^[Li, 1999-367].

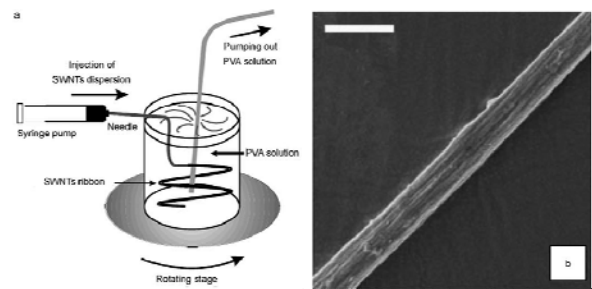


(a)

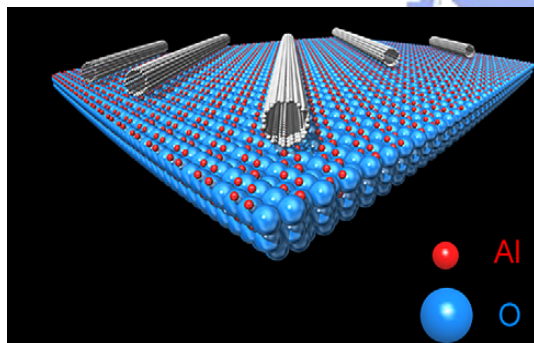
(b)



(c)



(d)



(e)

Fig. 2-13 Approaches to carbon nanotube organization: (a) Aligned growth under external forces, (b) Template approaches, (c) Crowding effect, (d) Postgrowth aligned deposition from liquid dispersions, and (e) Epitaxial approaches [Joselevich 2002-1137; Li, 1999-367; Fan 1999-512; Ago 2005-433; Burghard 1998-584]

(c) Crowding effect

Most frequently found in the literature are nanotubes grown in a very dense organization with vertical alignment due to the crowding effect. Fan *et al.*^[Fan 1999-512] used porous silicon

substrates with evaporated iron catalyst pattern to produce nanotube blocks by thermal CVD that grew perpendicular to the substrate. As shown in Fig. 2-13(c), the high density of nanotubes within each block confined the nearest neighbors and attracted the outermost nanotubes to their neighbors via van der Waals forces, resulting in the oriented growth.

(d) Postgrowth aligned deposition from liquid dispersions

Several approaches have been explored to laterally align CNTs such as controlled directed deposition through chemical modification of the surfaces of nanotubes or substrates [Burghard 1998-584, Meitl 2004-1643]. Postgrowth aligned deposition from liquid dispersions at specific locations and directions on the surface, by means of chemical modifications on either or both surface and nanotubes under external forces generated by flow, magnetic, or electric fields, and surface acoustic waves. However, the dispersion of nanotubes in liquid is difficult, normally requiring sonication or acid treatment. Moreover, the intrinsic electrical and mechanical properties of the SWNTs are often damaged by both sonication and chemical modification.

Poulin and co-workers have made important progress in this direction through their flow-induced alignment method [Vigolo, 2000-290]. The method starts with a macroscopically stable nanotube suspension, which is made by dispersing SWNTs in an aqueous solution of sodium dodecyl sulfate (SDS). As shown in Fig. 2-13(d), the suspension is injected through a 0.5-mm-diameter syringe needle into a 5 wt% polyvinylalcohol solution, which is in a cylindrical container rotated at speeds ranging from 30 to 150 rpm. CNT alignment induced by the shear or elongational flow takes place at the tip of the needle. The alignment is maintained by the polyvinylalcohol solution because it allows the nanotubes to rapidly stick together as they emerge from the needle. Long ribbons (Fig. 2-13(d)) are thus formed in the solution and SWNT bundles are preferentially aligned along the main axis of the ribbons.

(e) Epitaxial approaches

Epitaxial approaches, namely, surface-guided growth along lattice directions

(lattice-directed epitaxy), atomic steps (ledge-directed epitaxy), and nanofacets (graphoepitaxy) on single-crystal surfaces [Ago 2005-433, Ismach 2006-1706].

2.5 Analysis methods of the CNSs

In nanoscale science and technology, the characterization of products represents a persistent problem and the experimental techniques that have been used for the qualitative and quantitative characterization of CNSs in the current literature are presented briefly.

2.5.1 Morphologies, and lattice image analyses

High-resolution microscopes are indispensable instruments for the characterization of CNSs due to their ability to directly visualize the outcome of the experiments. Transmission electron microscopy (TEM), scanning electron microscopy (SEM), and atomic force microscopy (AFM) have been the most widely employed techniques. In TEM, a thin sample (normally several tens of nanometers or less in thickness) is required to ensure that an accelerated electron beam can pass through it. The sample size is very small, normally no more than 50 mm. The focused ion beam, also known as FIB, is also commonly used to prepare samples for the transmission electron microscope. The nanometer-scale resolution of the FIB allows the exact thin region to be chosen. This is vital, for example, in integrated circuit failure analysis. If a particular transistor out of several million on a chip is bad, the only tool capable of preparing an electron microscope sample of that single transistor is the FIB. However, the drawback to FIB sample preparation is the surface damage and implantation, which produces noticeable effects when using techniques such as high-resolution “lattice imaging” TEM or electron energy loss spectroscopy. This damaged layer can be minimized by FIB milling with lower voltages or by further milling with a low voltage argon ion beam after completion of the FIB process. In SEM, there is no limit on

sample size in principle, but the sample should be conducting or semiconducting. High-resolution imaging of CNTs on insulating substrates such as glass or plastics can not be achieved by SEM. The AFM consists of a microscale cantilever with a sharp tip (probe) at its end that is used to scan the specimen surface. The information is gathered by "feeling" the surface with a mechanical probe and is not limited by the size or electrical conductivity of the substrates. Piezoelectric elements that facilitate tiny but accurate and precise movements on (electronic) command enable the very precise scanning.

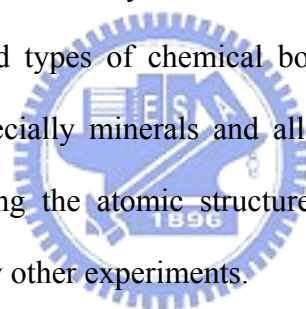
2.5.2 Bonding and crystal structure analyses

Electron diffraction of solids is usually performed in a TEM where the electrons pass through a thin film of the material to be studied. The resulting diffraction pattern is then observed on a fluorescent screen, recorded on photographic film or using a CCD camera. In a TEM, a single crystal grain or particle may be selected for the diffraction experiments. This means that the diffraction experiments can be performed on single crystals of nanometer size, whereas other diffraction techniques would be limited to studying the diffraction from a multi-crystalline or powder sample. Furthermore, electron diffraction in TEM can be combined with direct imaging of the sample, including high resolution imaging of the crystal lattice, and a range of other techniques. These include chemical analysis of the sample composition through energy-dispersive X-ray spectroscopy, investigations of electronic structure and bonding through electron energy loss spectroscopy, and studies of the mean inner potential through electron holography.

Raman spectroscopy is a spectroscopic technique used in condensed matter physics and chemistry to study vibrational, rotational, and other low-frequency modes in a system. It relies on inelastic scattering, or Raman scattering, of monochromatic light, usually from a laser in the visible, near infrared, or near ultraviolet range. The laser light interacts with phonons or other excitations in the system, resulting in the energy of the laser photons being shifted up or

down. The shift in energy gives information about the phonon modes in the system. Raman spectroscopy is commonly used in chemistry, since vibrational information is specific for the chemical bonds in molecules. It therefore provides a fingerprint by which the molecule can be identified.

X-ray crystallography is a method of determining the arrangement of atoms within a crystal, in which a beam of X-rays strikes a crystal and scatters into many different directions. From the angles and intensities of these scattered beams, a crystallographer can produce a three-dimensional picture of the density of electrons within the crystal. From this electron density, the mean positions of the atoms in the crystal can be determined, as well as their chemical bonds, their disorder and sundry other information. X-ray crystallography has been fundamental in the development of many scientific fields. This method could determine the size of atoms, the lengths and types of chemical bonds, and the atomic-scale differences among various materials, especially minerals and alloys. X-ray crystallography is still the chief method for characterizing the atomic structure of new materials and in discerning materials that appear similar by other experiments.

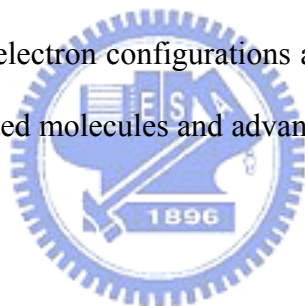


2.5.3 Electrical, optical and thermal properties measurements

Field emission (FE) is the emission of electrons from the surface of a condensed phase into another phase due to the presence of high electric fields. In this phenomenon, electrons with energies below the Fermi level tunnel through the potential barrier at the surface, which the high electric field sufficiently narrows for the electrons to have a non-negligible tunneling probability. Variations in the emitted current are primarily due to the field dependence of this surface potential barrier. The measurements were conducted by the simple diode configuration and carried out in a high vacuum chamber pumped down to a pressure of about 10^{-6} Torr. A high voltage source-measure unit (Keithley 237) was used for providing the sweeping electric field (E) and monitoring the emission current density (J).

The thermal properties are often measured by thermogravimetric analysis (TGA), which is a type of testing that is performed on samples to determine changes in weight in relation to change in temperature. Such analysis relies on a high degree of precision in three measurements: weight, temperature, and temperature change. As many weight loss curves look similar, the weight loss curve may require transformation before results may be interpreted. A derivative weight loss curve can be used to tell the point at which weight loss is most apparent.

Photoluminescence (PL) is a process in which a substance absorbs photons (electromagnetic radiation) and then re-radiates photons. Quantum mechanically, this can be described as an excitation to a higher energy state and then a return to a lower energy state accompanied by the emission of a photon. A basic understanding of the principles involved can be gained by studying the electron configurations and molecular orbitals of simple atoms and molecules. More complicated molecules and advanced subtleties are treated in the field of computational chemistry.



Chapter 3

Experimental Methods

Three processes were developed to selectively deposit the oriented CNSs with the given number density on the desired positions to form CNSs patterns. The processes include the AAO template-catalyst-assisted, electroless plating catalyst-assisted, and CNSs-electrophoresis-assisted methods. The experimental flowcharts, the detail experimental procedures and structure-property-analyses methods for each process will be illustrated separately in the following Sections.

3.1 Experimental flowcharts

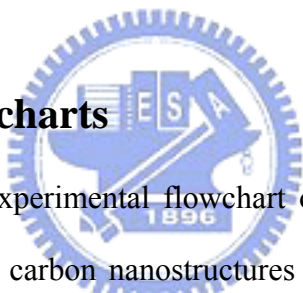


Fig. 3-1 illustrates the experimental flowchart of the AAO template-catalyst-assisted process. The vertically-aligned carbon nanostructures with tunable density are grown using AAO as a template and applied for field emitter arrays.

The experimental flowchart in Fig. 3-2 shows fabrication steps and analyses of the electroless plating catalyst-assisted process. In this process, the catalyst assisted CNTs by electroless plating are examined and then horizontally CNTs are grown across the patterned substrate where the catalysts are selectively deposited by electroless plating.

Flowchart of the CNSs-electrophoresis-assisted process is shown in Fig. 3-3. Electrophoresis method was used for depositing carbon nanostructure films on various substrates from stable SWNTs suspensions and their field emission properties are measured.

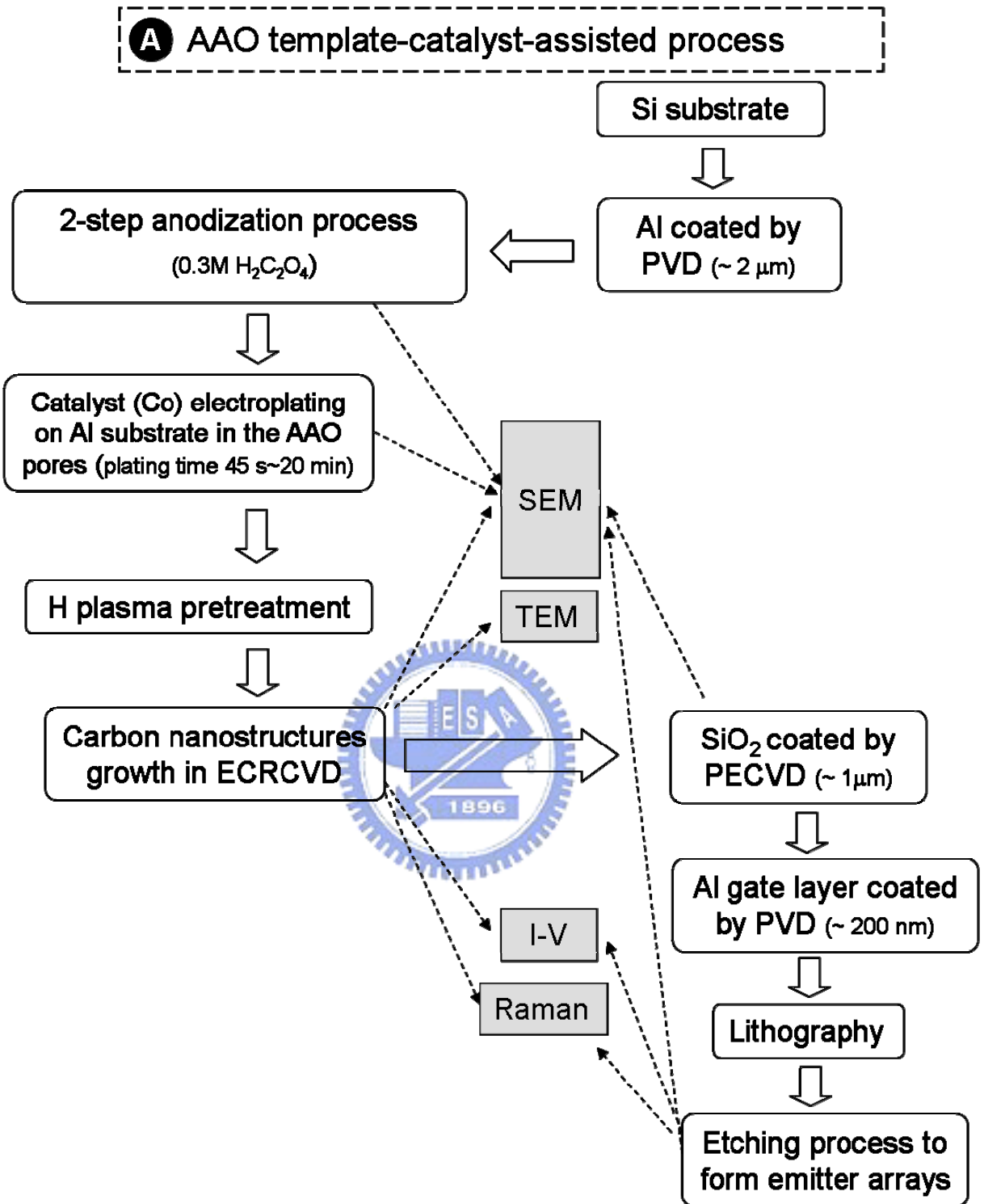


Fig. 3-1 Experimental flowchart for the AAO template-catalyst-assisted process.

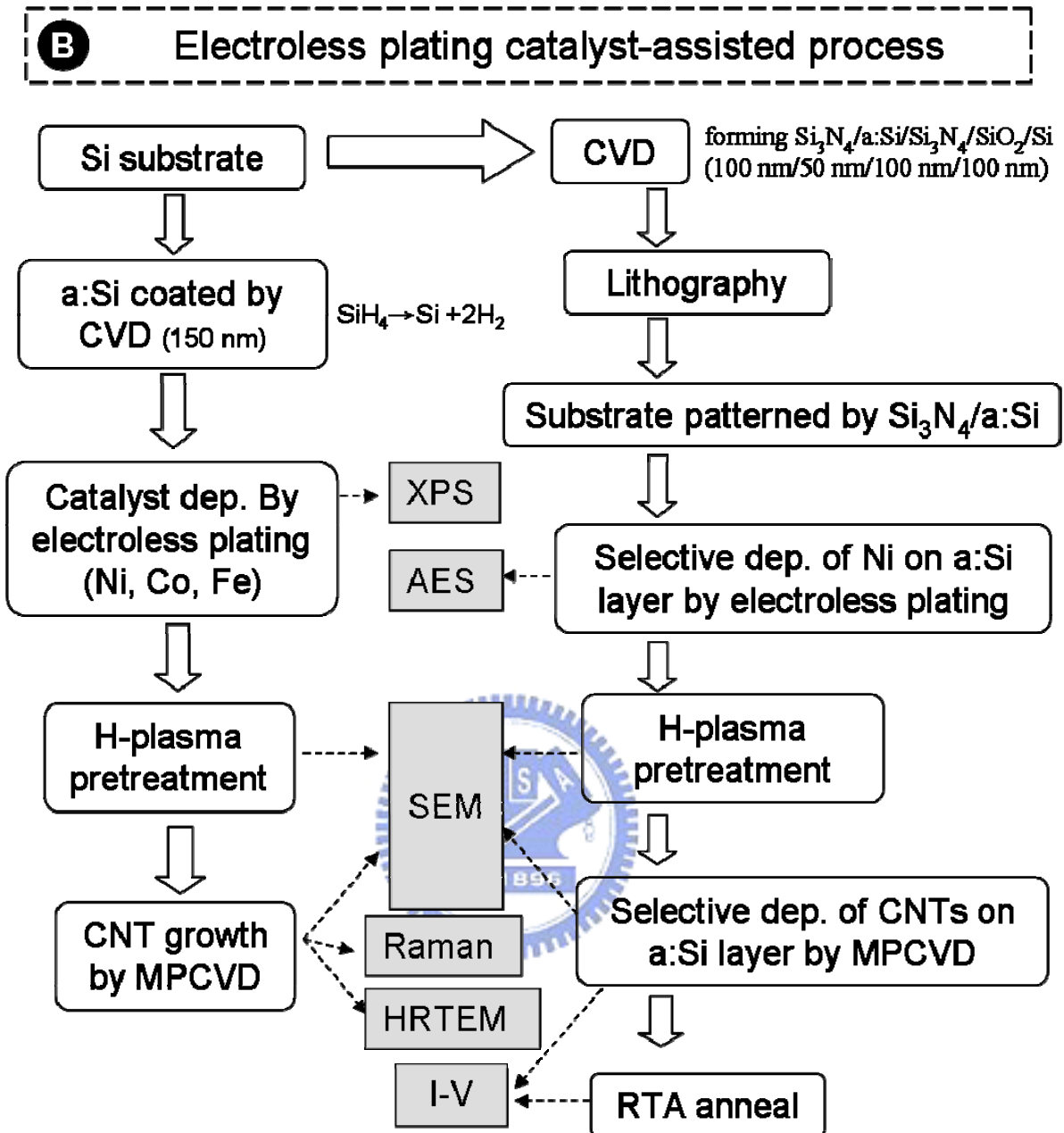


Fig. 3-2 Experimental flowchart for the electroless plating catalyst-assisted process.

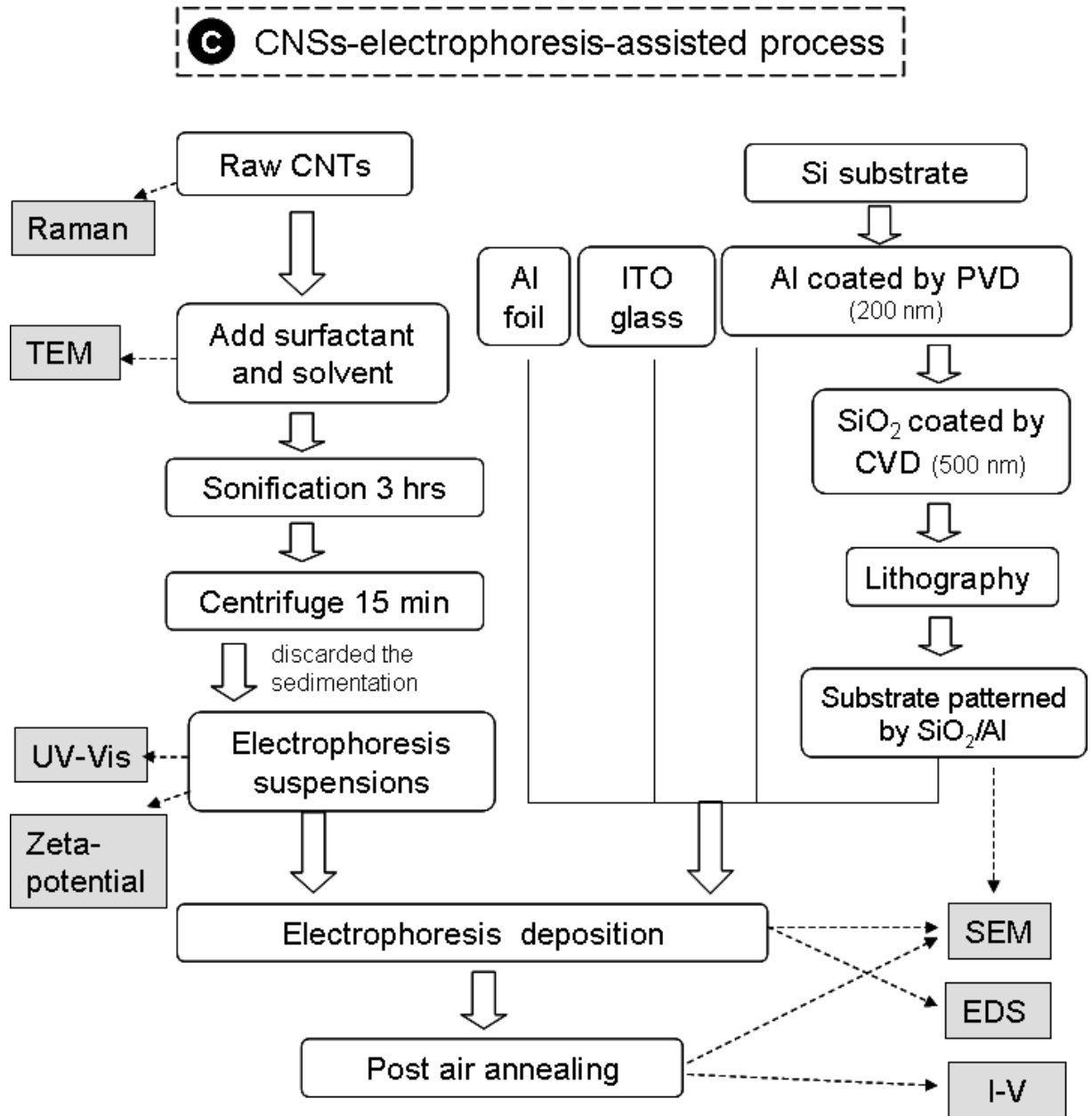


Fig. 3-3 Experimental flowchart for the CNSs-electrophoresis-assisted process.

3.2 AAO template-catalyst-assisted process

3.2.1 AAO-template preparation by anodization process

In this study, AAO template is directly fabricated on the Si wafer by a two-step anodization process, and the corresponding schematic diagram is sketched in Fig. 3-4. It begins with the deposition of an aluminum film on a (100)-oriented *p*-silicon wafer by a high vacuum thermal evaporator (ULVAC EBX-6D) with a base pressure of $< 4 \times 10^{-6}$ Torr. Aluminum ingots with a purity of 99.999 % are used as aluminum source after cleaning in a 10 vol.% hydrogen chloride (HCl) solution for 60 s. Tungsten boats are cleaned in a mixed solution of 20 vol.% hydrogen fluoride (HF) and 80 vol.% nitric acid (HNO₃) for 15 sec and then are used to carry and melt the aluminum ingots.

Experimental setup for anodization is shown in the Fig. 3-5, including a tank, electrodes, electrolyte and a power supply. A platinum foil is used as the cathode and the anode was the aluminum film specimen which only a circle with an area of about 1.3 cm² is exposed to the electrolyte. First anodizing step is carried out in a 0.3 M oxalic acid (H₂C₂O₄) solution at room temperature under a constant polarization voltage of 40 V for 5 min (Fig. 3-4(b)). Power is applied by a source-measure unit (Keithley Model 2400) and controlled by the computer program. The thus formed nanoporous AAO about 1 μm thick is removed by wet chemical etching at 60°C with a mixture solution of H₃PO₄ and CrO₃, thereby leaving a relatively ordered indent pattern on the surface of the Al film (Fig. 3-4(c)). The second anodizing step is carried out on the indented Al film for 4 min under the same anodization condition as the first anodizing step (Fig. 3-4(d)). AAO barrier layer etching and pore widening are preformed by immersing the specimens in a 5 wt.% H₃PO₄ solution at 30°C for 40 min. This results in highly uniform and periodic nanoporous channels in the AAO layer, which are then used as the template for the growth of carbon nanostructures.

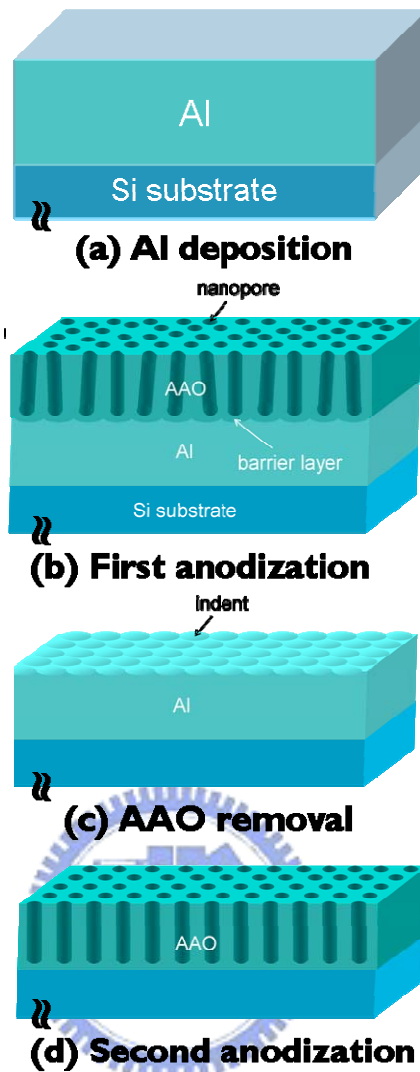


Fig. 3-4 Schematic diagram of the two-step anodization process.

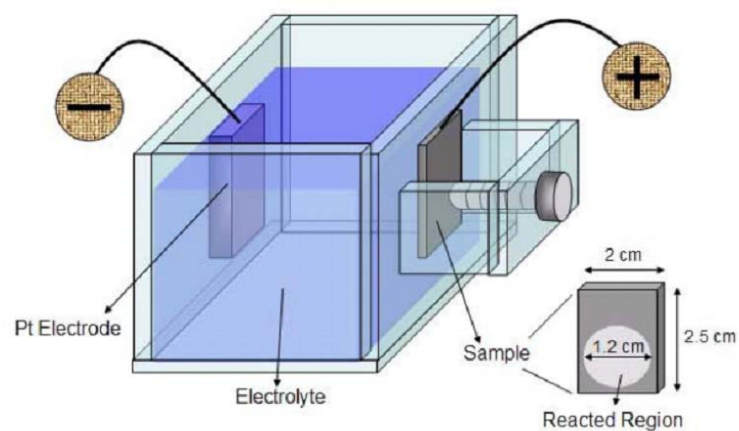


Fig. 3-5 Schematic diagram of experimental setup for the Al anodization.

3.2.2 Catalyst deposition in the nanopores of AAO template by electroplating

A metallic Al layer ~300 nm thick is left on the wafer surface after the AAO fabrication, and is used as the bottom electrode. Cobalt is used as the catalyst for CNS growth, and is electrochemically deposited at the AAO pore bottom in the mixture electrolyte of CoSO_4 and H_3BO_3 . Co electroplating is carried out in the electrolyte mixture of CoSO_4 and H_3BO_3 by applying an AC voltage of 12.3 V_{rms} . The size of the Co particle in AAO pore channels is tuned by varying the plating time (0 ~ 1200 s).

3.2.3 CNSs deposition by ECR-CVD

The schematic diagram of the ECR-CVD system is shown in Fig. 3-8. Microwave power (2.45 GHz) is supplied to a plasma chamber through a quartz dome entrance window. A magnetic field of 875 Gauss for ECR plasma excitation is generated by the coils surrounding the resonance volume and is applied perpendicularly to the substrate surface. A negative dc bias is applied to the substrate holder. The plasma stream is introduced into the deposition chamber, which has previously been pumped down to a base pressure of about 10^{-6} Torr by a diffusion pump system. It takes the advantages of low temperature, high dissociation efficiency and wider deposition area.

To deposit carbon nanostructures in the AAO template, the Co catalysts are first treated with the H_2 plasma at 600°C for 10 min in the ECR-CVD system. Then, the CNS growth is carried out at 600°C in an ECR-CVD system using a gas mixture of 20% CH_4 and 80% H_2 (5 sccm/ 25 sccm) as the plasma source for 30 min. During the CNS growth, the ECR-CVD system is under the following operation conditions: magnetic field strength 875 G, microwave power 750 W, substrate bias -100 V, working pressure $\sim 2 \times 10^{-3}$ Torr, deposition temperature 600°C .

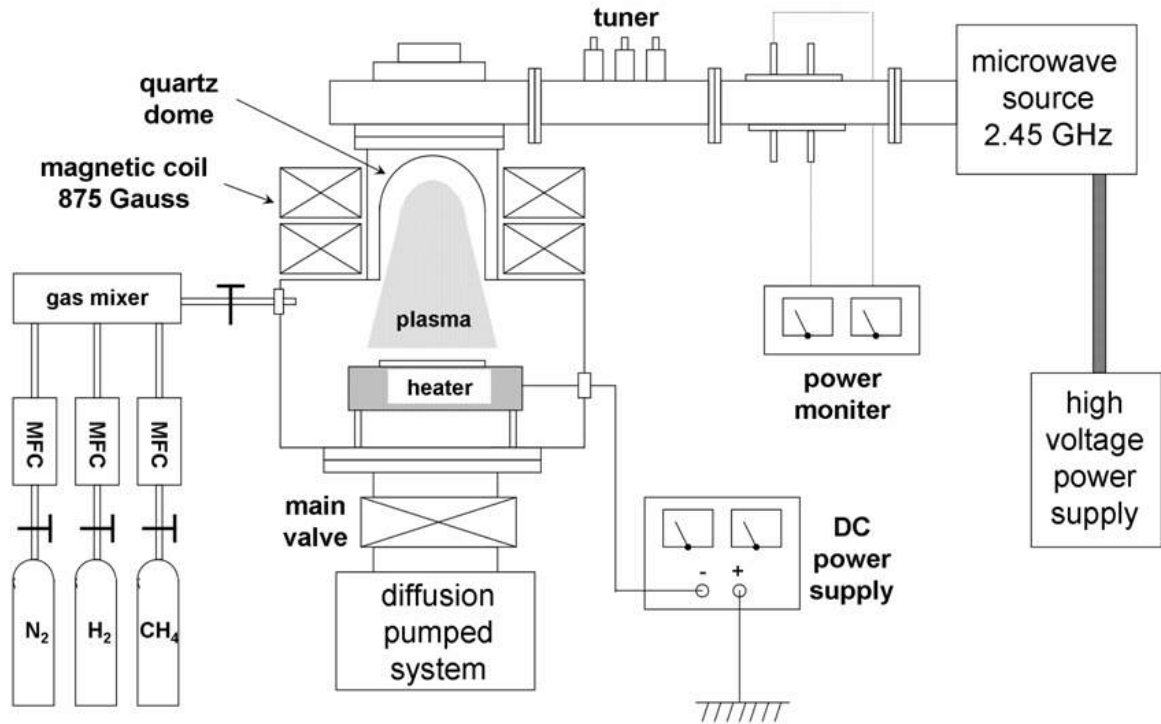


Fig. 3-6 Schematic diagram of the ECR-CVD system.

3.2.4 Fabrications of the emitter arrays on the AAO-assisted CNSs

The fabrication scheme of the emitter arrays from AAO-assisted CNSs is shown in the Fig. 3-9. After the preparation of the AAO-assisted CNS emitters, tetraethoxysilane (TEOS) oxide is deposited on the CNSs as the dielectric layer by plasma enhanced CVD (PE-CVD), and followed by the evaporation-deposition of an Al layer as the gate electrode. The pattern with a diameter of $6.5 \mu\text{m}$ is photolithographically defined by a mask aligner (Karl-Suss MJB-3). The Al top layer is etched by a high density plasma reactive ion etching (HDP-RIE) system using the gas mixture of BCl_3 and Cl_2 as the etchant source. The oxide dielectric is then HDP-RIE etched using a gas mixture of CHF_3 and Ar as the plasma source. After the HDP-RIE process, buffered oxide etchant (BOE) is used to remove the remnant SiO_2 .

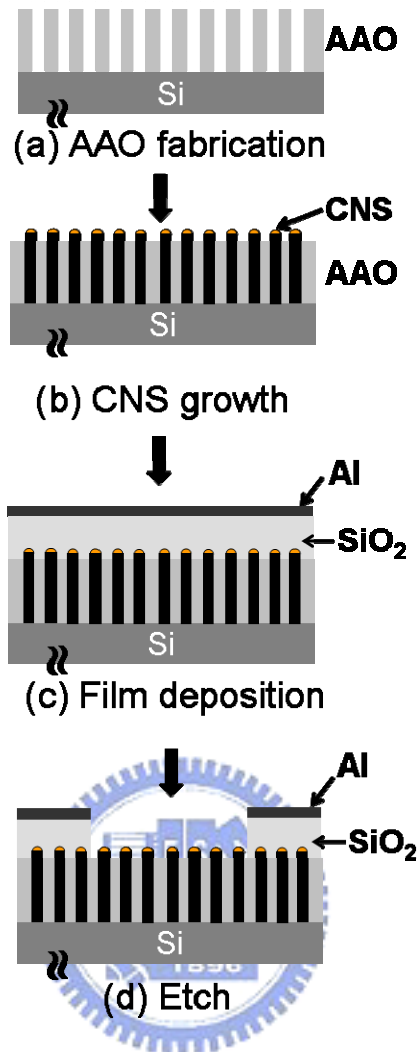


Fig. 3-7 The fabrication scheme of the emitter arrays on the AAO-assisted CNSs: (a) preparation of the AAO layer on the Si wafer, (b) CNS growth by ECR-CVD deposition, (c) SiO_2 dielectric and Al gate electrode depositions on the CNSs, and (d) RIE and BOE etches to open the field-emission area.

Table 3-1 Specimen designations of the AAO-assisted CNSs and their deposition conditions.

Specimen Designation	Co catalyst plating time (s)	CNSs deposition time (min) [#]	Post array-preparation conditions [☆]	
			RIE (s)	BOE (s)
A1	0	35	-	-
A2	45	35	-	-
A3	60	35	-	-
A4	75	35	-	-
A5	90	35	-	-
A6	90	20	-	-
A7	600	-	-	-
A8	1200	-	-	-
A9	60	30	240	-
A10	60	30	270	5
A11	60	30	300	-
A12	60	30	360	-
A13	60	30	420	-
A14	60	30	480	-

[#] Other desposition conditions:

H-plasma pretreatment conditions:

H₂=30 sccm, 750 W microwave power, substrate bias -30 V, under $\sim 2 \times 10^{-3}$ Torr, and $\sim 600^\circ\text{C}$ in the ECRCVD system for 10 min.

CNSs deposition conditions:

CH₄/H₂=5/25 sccm/sccm, 750 W microwave power, substrate bias -100 V, under $\sim 2 \times 10^{-3}$ Torr, and $\sim 600^\circ\text{C}$ in the ECRCVD system.

[☆]Other emitter arrays preparation conditions:

The pattern with a diameter of 6.5 μm is photo-lithographically defined and etched by a HDP-RIE system and then BOE is used to remove the remnant SiO₂.

3.3 Electroless plating catalyst-assisted process

3.3.1 Substrate preparation for selective deposition of catalyst

Two substrates are used for electroless plating catalyst-assisted process. For examining the characteristics of the catalysts and carbon nanotubes by electroless plating, substrate condition 1 (SC 1) is prepared by coating a 150 nm-thick a:Si layer on the Si substrate by vertical furnace system. The other substrate (SC 2) is the trench patterned Si substrate designed for growing horizontally- oriented CNTs across the trenches and the process is schematically shown in Fig. 3-8.

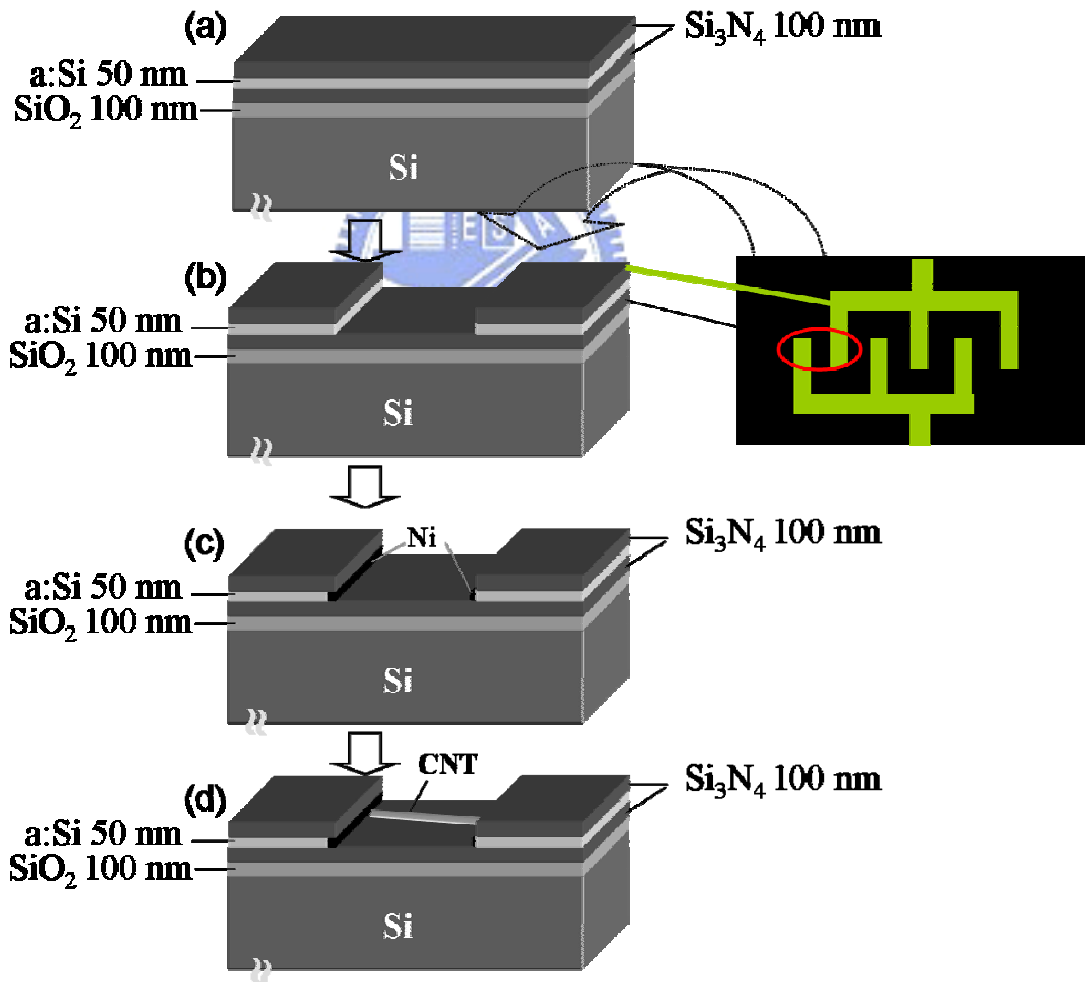


Fig. 3-8 Schematic diagrams showing the electroless plating catalyst-assisted CNTs grown across trenches of a pattern.

For film depositing step in Fig. 3-8(a), a 100 nm-thick Si₃N₄ layer is coated by LPCVD and a 100 nm-thick SiO₂ layer is first coated on the Si substrate by furnace to prevent crack formation from large tensile stress of Si₃N₄ layer. Then, the film depositing step is followed by a 50 nm-thick a:Si layer coating in the vertical furnace system and accomplished after another 100 nm-thick Si₃N₄ layer coating. After photolithography, the 400 nm-wide and 800 nm-wide trenches on the wafer were then created by RIE process as shown in Fig. 3-8(b) and the top-view of the designed pattern is shown in the right of Fig. 3-8(b).

3.3.2 Catalyst deposition by electroless plating

Three different solutions (Ni, Co, and Fe Bath) for electroless plating are prepared and their compositions are listed in the Table 3-2. There are no external electrodes present and electroless plating reaction begins when the specimens are immersed into the solution at 100°C. Instead of an anode, the metal is supplied by the metal salt and a substrate serving as the cathode, and the presence of a chemical reducing agent in solution to reduce metallic ions to the metal state. For the Ni alkaline bath with 100 ml, it consists of a metallic salt 0.5g

Table 3-2 The compositions of the electroless solutions.

Compositions	Ni Bath	Co Bath	Fe Bath
Metallic salt	0.5 g 0.02 M NiSO ₄ · 6H ₂ O	0.6 g 0.02 M Co(NO ₃) ₂ · 6H ₂ O	0.84 g 0.02 M Fe(NO ₃) ₃ · 9H ₂ O
Other compositions	10 ml	10 %	N ₂ H ₄
	0.5 g	0.1M	NH ₄ Cl
	20 ml	1.4 %	NH ₄ OH
	140 ml		DI water

0.02M NiSO₄·6H₂O, a reducing agent 10 ml 10% N₂H₄, 0.5g 0.1M NH₄Cl, 20 ml 1.4% NH₄OH and 140 ml de-ionized water. For the Co bath or Fe bath, the metallic salt is changed to Co(NO₃)₂ · 6H₂O or Fe(NO₃)₃ · 9H₂O, respectively. In order to selectively deposit on the pattern, the patterned substrate is immersed into the solution and the catalyst are coated on the catalytic surface a:Si layer as shown in Fig. 3-8(c).

3.3.3 CNTs deposition by MPCVD

The schematic diagram of MPCVD system is shown in Fig.3-9. The main components of the system can be divided into six parts: the microwave generator, wave guides, reaction chamber, gas flow controller, gas pressure controller and pumping system. The microwave generator of microwave source system (Frequency 2.45 GHz, Power 1.3 kW) was produced by Tokyo electronic Corp. Ltd. The reaction chamber contains quartz tube (inner: 47 mm, outer: 50 mm, China Quartz Corp. Ltd), stainless chamber, stainless holder and rotary pump (Hitachi Corp. Ltd). As Fig. 3-10 shown, sample holder is manufactured by stainless steel, it can bear high working temperature and reduce vacuum pollutions while plasma working. The upper electrode that was made by stainless steel is connected to the DC power supply output. The substrate temperature is measured by thermal couple which equipped in the holder. Mass flow control (MKS model 247) system is used to regulate the flow rate of reacting gas while depositing. The work pressure of chamber can be regulated stably by throttling valve. There is no external heater system equipped on MPCVD. The plasma is used to heat the substrate as the heat source. Cooling cycle system is made up of the refrigerator with closed cooling water and the conduit.

The catalyst films are pretreated with H plasma under the following conditions : H₂ flow rate 100 sccm, microwave power 400 W, pressure 9 Torr, and deposition temperature 550 ~ 580°C in the MPCVD system and then followed by CNTs deposition using CH₄ and H₂ as source gases. The CNTs deposition conditions are CH₄/H₂ = 1/100 sccm/sccm, 800 W

microwave power, under 16 Torr and 660~680°C.

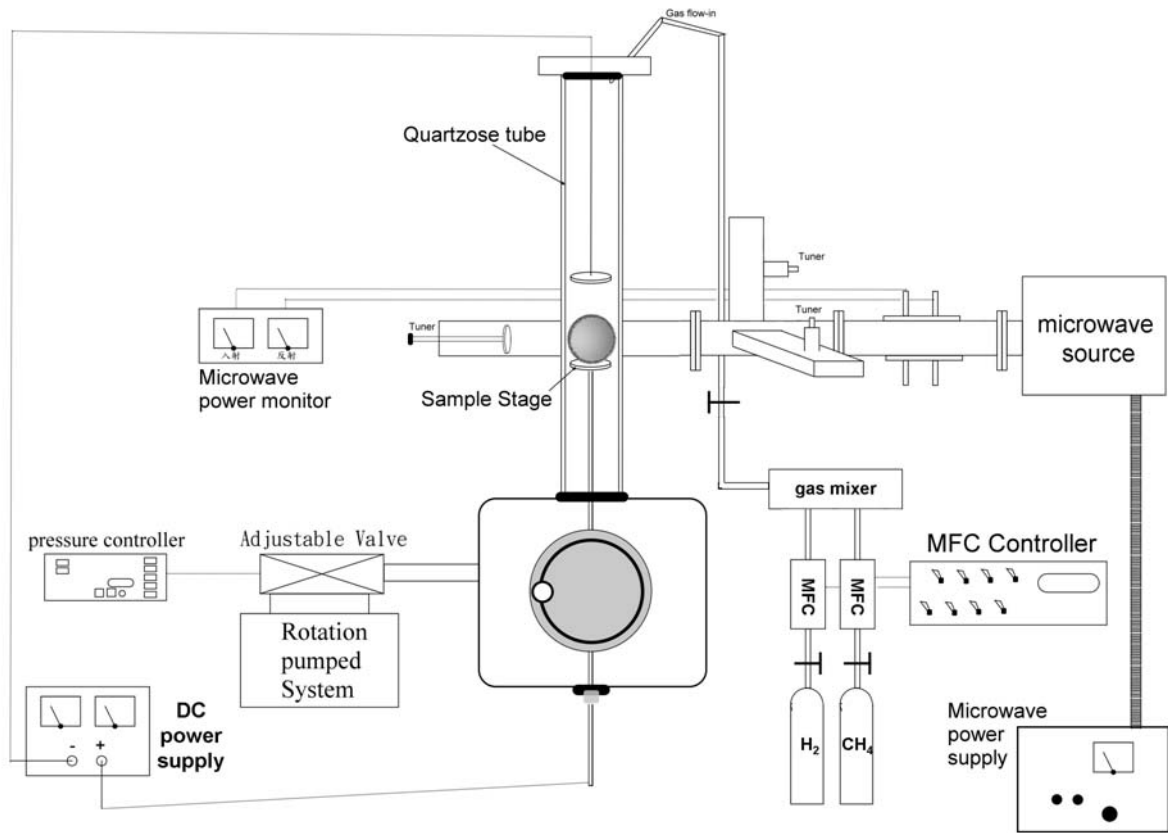


Fig. 3-9 Schematic diagram of the MPCVD system.

3.3.4 RTA heat treatment

Some as-deposited horizontally CNT are annealed at 760°C by rapid thermal annealing (RTA). Table 3-3 shows the specimen designations of the electroless plating catalyst-assisted method and clearly describes the substrate conditions catalyst material and their plating time.

Table 3-3 Specimen designations of the electroless plating catalyst-assisted CNTs and their deposition conditions.

Specimen Designation #	Substrate pretreated condition*	Catalyst (plating time, s)
B1	SC 1	Co (40)
B2	SC 1	Fe (120)
B3	SC 1	Ni (40)
B4	SC 2	Ni (10)
B5	SC 2	Ni (15)
B6	SC 2	Ni (20)
B7	SC 3	Ni (20)
B8	SC 2	Ni (30)
B9	SC 2	Ni (60)

* Substrate conditions (as described in 3.2.1):

SC 1: Si substrate with a:Si coating.

SC 2: Si substrate with SiO₂ 100 nm / Si₃N₄ 100 nm / a:Si 50 nm / Si₃N₄ 100 nm stacks patterned by Si₃N₄ / a:Si and with 400 nm trench width.

SC 3: Substrate preparation similar with SC2 but with 800 nm trench width.

Other disposition conditions:

H-plasma pretreatment conditions:

H₂=100 sccm, 400 W microwave power, under 9 Torr, and 550 ~ 580°C in the MPCVD system.

CNTs deposition conditions:

CH₄/H₂=1 sccm / 100 sccm, 800 W microwave power, under 16 Torr and 660~680°C in the MPCVD system.

3.4 CNSs-electrophoresis-assisted process

3.4.1 Substrate preparation for selective deposition

Various substrates are used in this method such as Al films on Si substrate, ITO glass, Al foil and the square-shaped pattern made of Al and SiO₂ components by lithography process. For the Al/Si substrate, an aluminum film is coated on silicon wafer by a high vacuum thermal evaporator (ULVAC EBX-6D) with a base pressure of $< 4 \times 10^{-6}$ Torr and aluminum ingots with a purity of 99.999% were used as aluminum source. For the Al-SiO₂ pattern, the SiO₂ film is first coated by plasma-enhanced chemical vapor deposition (PECVD, STS Multiplex Cluster System) using TEOS and O₂ process gas under plasma power 300W; process pressure: 300~800 mTorr and temperature 300°C. After photolithography, the photo resist is remained on the dark region in Fig. 3-10 and the region is designed for the SiO₂ part. The aluminum film is also coated by thermal evaporator and the aluminum on the photo resist is lifted off by sonification in acetone.

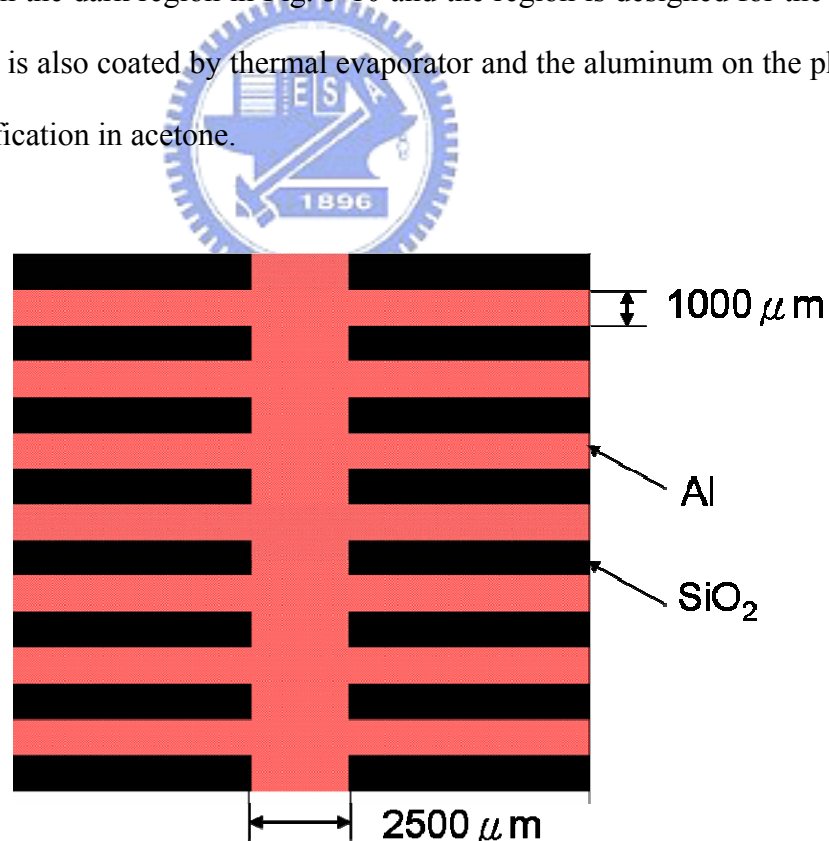


Fig. 3-10 Square-shaped pattern made of Al and SiO₂ components for EPD process.

3.4.2 Suspensions preparation for CNTs dispersion

The raw SWNTs in this work were prepared by arc discharge method and provided by ITRI (Industrial Technology Research Institute, Taiwan). The SWNT suspensions were made by adding 0.001 g of SWNTs and 0.2 g of the surfactant into 20 ml of solvent (de-ionized water or butyl alcohol) and sonicated for 3 hours, where the surfactants (acting as dispersants) include SDS (sodium dodecyl sulfate), CTAB (hexadecyl trimethyl ammonium bromide) and TOPO (trioctylphosphine oxide). The suspension solutions were then centrifuged for approximately 15 min and discarded the sedimentation. Suspension designations and their compositions are listed in the Table 3-4.

Table 3-4 Suspension designations and their compositions.

Suspension designations [#]	Solvent (20 ml)	Surfactant* (0.2 g)
S1	D.I water	--
S2	D.I water	SDS
S3	D.I water	CTAB
S4	butyl alcohol	TOPO

[#] Other composition: 0.001g CNT category are used in each suspension.

* SDS : Sodium dodecyl sulfate

CTAB : Hexadecyl trimethyl ammonium bromide

TOPO : Trioctylphosphine oxide

3.4.3 The electrophoretic processes with CNT suspensions

Experimental setup for electrophoretic depositions included a tank, electrodes, electrolyte and a power supply. Different EPD parameters such as applying dc voltage (30 ~ 50 V), anode-cathode distance (10 mm) and deposition time (60 ~ 120 s) are examined.

3.4.4 Post-annealing

The as-deposited CNSs films by electrophoresis were then annealed under air

environment on a hot plate at 100~300°C for 1 ~ 30 min. Table 3-5 shows the specimen designations for the EPD-prepared CNSs and their deposition parameters.

Table 3-5 Specimen designations of the CNSs-EPD-assisted films and their deposition parameters.

Specimen designation	Suspension designation [#]	EPD parameters at RT					Post air annealing	
		Electrode material [*]		anode-cathode distance [☆] (mm)	App. bias (V)	Dep. time (s)	Temp. (°C)	Time (min)
		anode	cathode					
C1	S1	Al	Al	10	30	60	300	5
C2	S2							
C3	S3							
C4	S4							
C5	S2	Al	Al	10	30	60	0	0
C6							100	3
C7							100	5
C8							200	3
C9							200	5
C10							300	1
C11							300	3
C12							300	10
C13							300	15
C14							300	30
C15	S2	Al-SiO ₂ ^{&}	Al	10	60	60	300	5
C16		ITO	ITO		50	120		
C17		Al foil	Al foil		30	60		

[#]The preparation of suspensions is described in detail in Table 3-4.

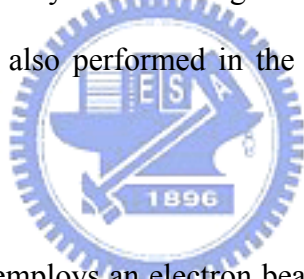
^{*} Electrodes of anode and cathode consist of the Si substrate coated with different electrode materials, except ITO and Al foil which are electrode materials without Si substrate.

[&]Al-SiO₂: The square-shaped pattern consists of Al and SiO₂ components, which is fabricated by lithography technique.

3.5 Structures and properties characterization

3.5.1 SEM, TEM, EDS and HRTEM

SEM is a very useful tool for observing surface morphology of specimen. SEM has secondary electrons or backscattered electrons detectors passing the signal to computer and forming image. TEM image is the result of electron transmitting through the specimen. TEM reveals the interior microstructure of the specimen, and it can give the high-resolution lattice image and the electron diffraction pattern as well. In this study, the morphologies and microstructures of the deposited structures were characterized by a field-emission SEM (FE-SEM) (Hitachi S-4000, JEOL JSM-6500F, and JSM-6700F), TEM (Philips Tecnai 20 (200 keV) and FETEM (JEOL-2100 (200 keV))). Specimens for the TEM analysis were cutting by the FIB technique or by ultrasonic agitation and dispersed onto Cu TEM grids. Moreover, EDS analyses were also performed in the TEM system to identify the chemical composition of the specimens.



3.5.2 AES

AES analysis technique employs an electron beam (2-30 keV) irradiating the specimen surface to excite Auger electrons which possess specific energy. Through assaying the kinetics energy of the Auger electrons by an electron energy analyzer, one can get to know the element composition and chemical state of the specimen. Because the incident electrons with low-energies (1-3 keV) have very short inelastic mean free paths (5-20 Å) inside the solid phase materials, AES technique is usually used to obtain the information within 50 Å away from the surface (surface analysis). In this study, AES was employed to investigate the chemical composition of the catalyst on the pattern. The AES analyses were performed using a Physical Electronics Auger 670 PHI Xi system with a Schottky field emission electron source.

3.5.3 Raman spectroscopy

Raman scattering was discovered by Raman in 1928. If an incident photon occurs inelastic scatter with specimen molecules and causes the energy change of the photon called Raman scattering. By this mechanism, one can measure the difference between incident and scattering light by a spectrometer to obtain the information of element and bonding structure of the specimen. In particular, Raman spectroscopy is useful in identifying carbon-based materials. There are two obvious bands located at about 1330 cm^{-1} (*D* band) and 1590 cm^{-1} (*G* band) which correlate with the vibration of sp^3 -bonded and sp^2 -bonded carbon atoms, respectively. In order to study the structural characterization of the CNS samples, a Jobin Yvon LABRAM HR Micro-Raman system with a He-Ne laser (wavelength: 632.8 nm) was utilized in the experiments.

3.5.4 XPS

Surface analysis by XPS involves irradiating a solid in vacuum with mono-energetic soft X-rays and analyzing the emitted electrons by energy. The spectrum is obtained as a plot of the number of detected electrons per energy interval versus their kinetic energy. Quantitative data can be obtained from peak height or peak areas, and identification of chemical states often can be made from exact measurement of peak positions and separations. In this study, XPS was employed to analysis the composition of the catalyst films by electroless plating. XPS analyses were performed on a ULVAC-PHI 1600 ESCA system with $Al-K\alpha$ (1486.6 eV) excitation. X-ray emission energy was 400 W with 15 kV accelerating voltage. Argon ion with ion energy of 5 keV was used for sputter profiling.

3.5.5 Electrical properties measurement

Fig. 3-11 shows the instrument setup and the test configuration used during field emission characterization. The measurements were conducted by the simple diode configuration and carried out in a high vacuum chamber pumped down to a pressure of about 10^{-6} Torr with a turbo molecular pump, backed up by a rotary mechanical pump.

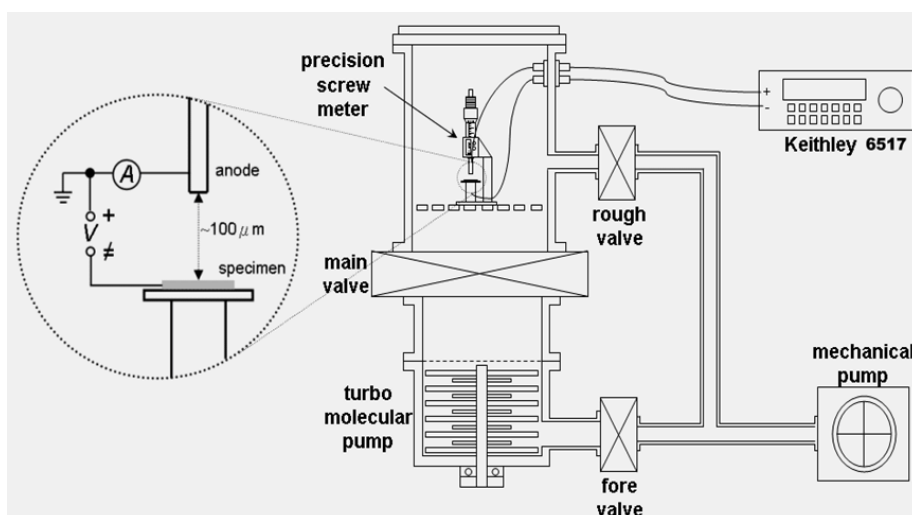


Fig. 3-11 Schematic diagram of the field emission measurement setup.

A steel probe with a diameter of 2 mm as anode was used for the measurement. The distance between the specimen and anode was about 100 μm controlled by a precision screw meter. The specimen (cathode) was biased with a voltage swept positively from 0 to 1000 V at room temperature to extract electrons from emitters. A high voltage source-measure unit (Keithley 237) was used for providing the sweeping electric field (E) and monitoring the emission current density (J). The measurement instruments are auto-controlled by the computer.

The I-V curves of the horizontally-oriented CNTs were examined by precision semiconductor parameter analyzer (HP 4156). The patterns were designed as shown in Fig. 3-8.

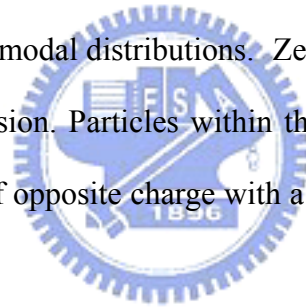
3.5.6 UV-Vis spectroscopy and Zeta potential measurement

Ultraviolet-visible (UV-Vis) absorption spectroscopy involves the spectroscopy of photons in the UV-visible region. It uses light in the visible and adjacent near ultraviolet and near infrared (NIR) ranges. UV-Vis spectrophotometer measures the intensity of light passing through a sample (I), and compares it to the intensity of light before it passes through the sample (I_0). The ratio I / I_0 is called the *transmittance*, and is usually expressed as a percentage (%T). The absorbance, A , is based on the transmittance:

$$A = -\log(\%T) \quad (3-1)$$

The basic parts of a spectrophotometer are a light source, a holder for the sample, a diffraction grating or monochromator to separate the different wavelengths of light, and a detector. In this study, samples for UV-Vis spectrophotometry (JASCO Model 7850) are placed in a transparent cell, which are rectangular in shape with an internal width of 1 cm and made of high quartz glass because it is transparent throughout the UV, visible and near infrared regions.

Dynamic Light Scattering from light scattering particle size analyzer (BROOKHAVEN 90 PLUS) provides a fast, simple method for submicron particle sizing. Random intensity fluctuations in scattered laser light arising from the Brownian motion of colloidal particles are analysed to give either a simple mean size and polydispersity (distribution width) or complete distribution data even for multimodal distributions. Zeta potential is measured by applying an electric field across the dispersion. Particles within the dispersion with a zeta potential will migrate toward the electrode of opposite charge with a velocity proportional to the magnitude of the zeta potential.



Chapter 4

Results and discussion for the AAO template -catalyst-assisted CNSs emitter arrays

4.1 Morphologies of AAO template and Co catalysts in nanopores

The AAO porous template prepared by the two step anodization process in oxalic acid solution had vertical channels and a uniform diameter around 80 nm (as shown in Fig. 4-1).

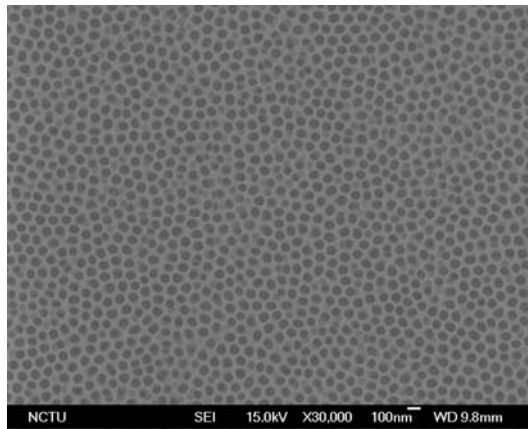


Fig. 4-1 SEM image of the AAO template after two-step anodization process.

Fig. 4-2 (a) to (f) are cross sectional-view SEM images of the AAO template after Co electroplating for 45, 60, 75, 90, 600 and 1200 s, respectively. Cobalt particles could be deposited at the bottom of AAO pore channels. The cobalt size increased with the electroplating time. The thickness of the barrier layer at the pore bottom can be greatly reduced by gradually decreasing the applied voltage at the end of the second anodization step [Thamida 2002-240]. This can be done in the pore widening step to expose the underlying conductive Al by wet etching. After the AAO template removal, the Co particles exhibited a diameter about 70 nm ~ 80 nm in diameter, in accordance with the AAO pore diameter because of the AAO pore channel confinement. The height of the Co particles is about 48 nm

for a depositing time of 45 s and increased to 84 nm for a depositing time of 90 s.

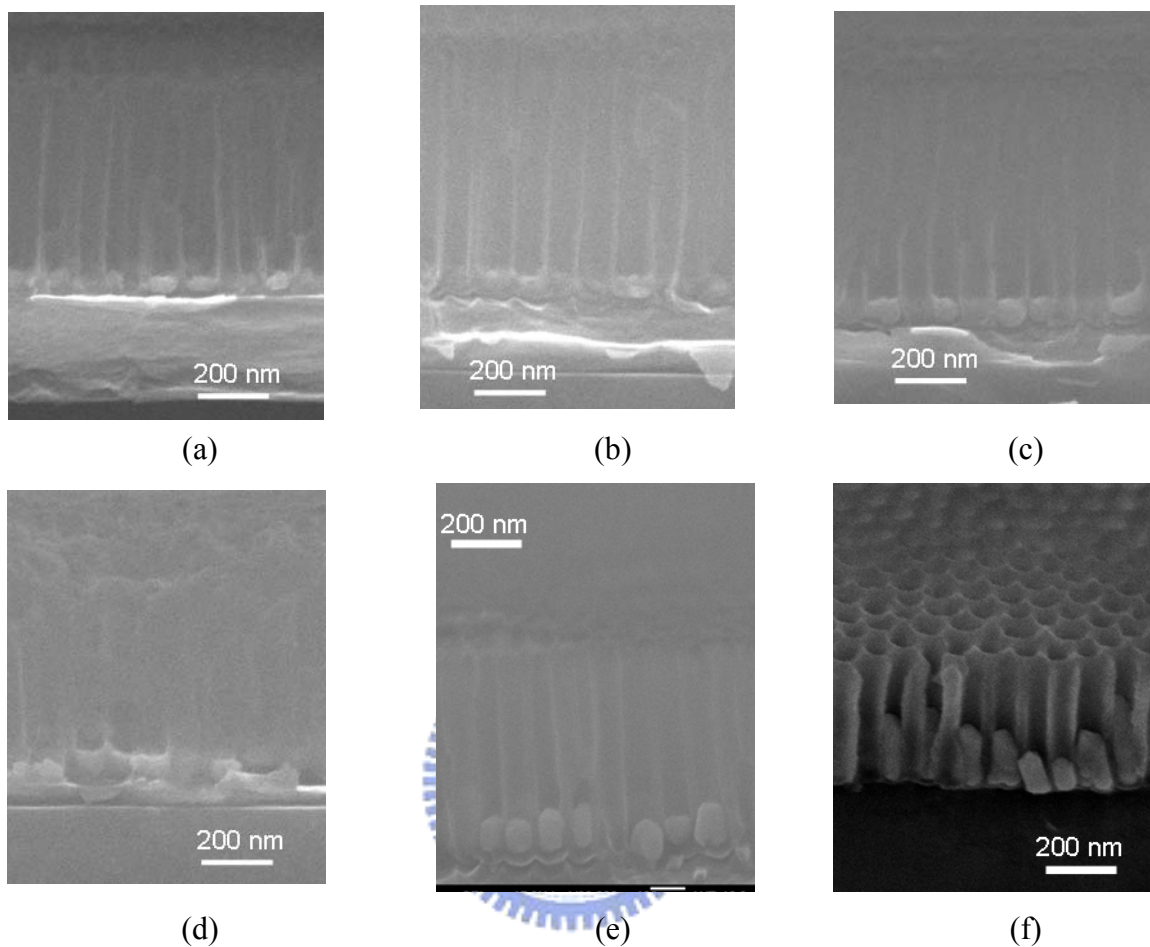


Fig. 4-2 Cross-section view of SEM images of the Co-deposited AAO template under different Co electroplating duration: (a) 45, (b) 60, (c) 75, (d) 90, (e) 600 and (f) 1200 s. (For SP. #A2, A3, A4, A5, A7 and A8, respectively.)

Fig. 4-3(a) shows the plot of the height of Co particle as a function of the electroplating time. Because of the confinement by the template, the height of the Co particles increased with increasing the deposition time with a constant cross-sectional diameter. The size and thus the height of the electrodeposited particle in AAO pores increased with the electroplating time.

4.2 Effects of the Co plating time on the AAO template-catalyst-assisted CNSs

4.2.1 On morphologies of the CNSs

Fig. 4-4 shows the side-view SEM images of CNSs grown out of the AAO template with Co catalysts electrodeposited for various times. For samples with Co catalysts deposited for 45 and 60 s (Fig. 4-4(a) and (b)), CNSs had irregular shapes with a sparse tube density and a diameter smaller than the AAO pore size. On the other hand, as the catalyst deposition time increased to 75 and 90 s (Figs. 4-4(c) and (d)), vertically aligned CNSs were grown out over the AAO surface with a tube diameter close to the AAO pore size.

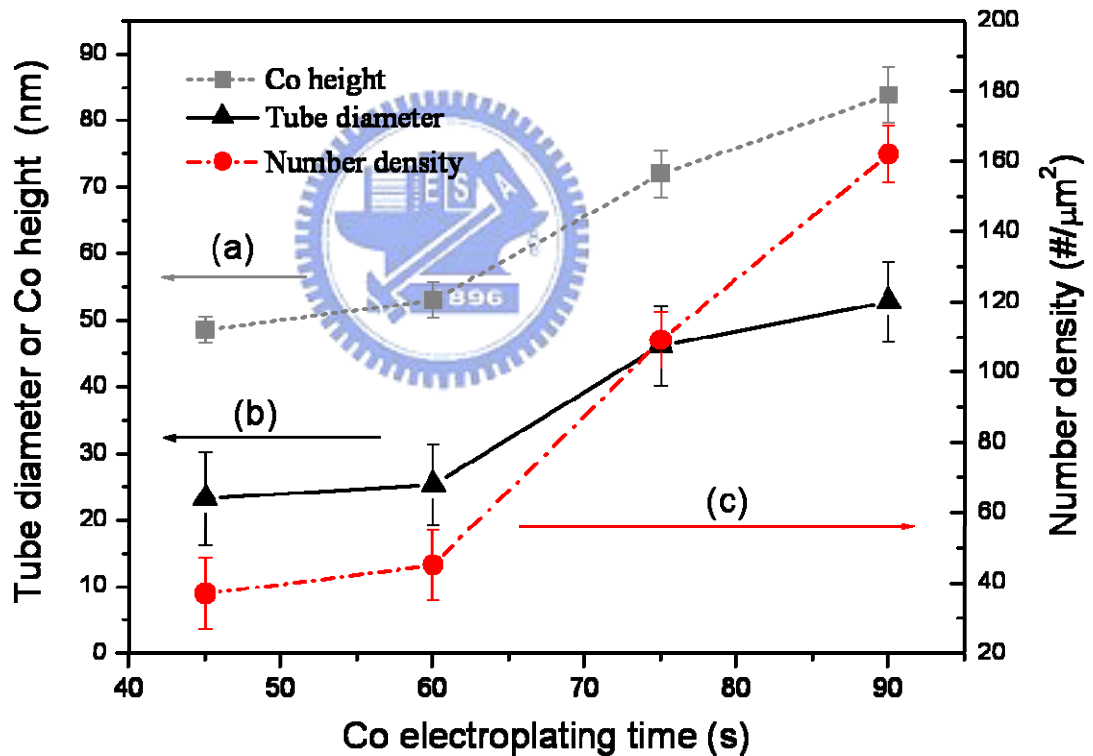


Fig. 4-3 The curves showing features of morphologies as a function of the Co plating time in AAO template catalyst-assisted process: (a) the deposited Co height in AAO, (b) tube diameter of CNSs, and (c) number density of the CNSs.

To examine the effects of the Co catalysts on the CNS growth on AAO template, the average tube diameter at half height of the CNS out of the AAO template was plotted against

the Co deposition time as shown in Fig. 4-3(b). The tube diameter was about 23 nm for the Co plating time of 45 s and increased to 53 nm when the Co deposition time was 90 s. The curve in Fig. 4-3(c) showed that CNSs had a larger number density with longer Co electroplating time.

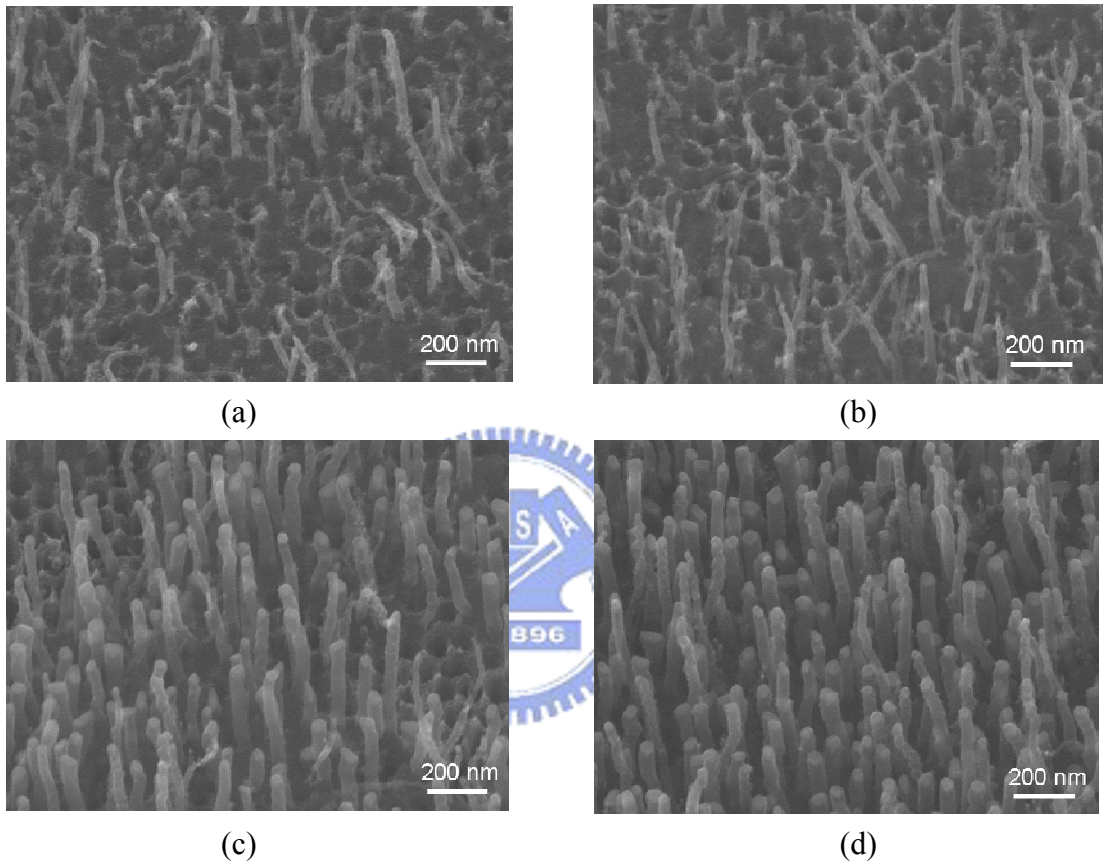


Fig. 4-4 Top-view SEM images of the as-deposited CNSs under different Co electroplating times: (a) 45, (b) 60, (c) 75 and (d) 90 s. (For SP. # A2, A3, A4 and A5, respectively)

4.2.2 On Raman spectra and TEM images of the CNSs

From Figs 4-4(a) and (b), some residual deposit can be clearly seen to cover a large area of the AAO surface. Amorphous carbon (a:C) residue is usually an inevitable byproduct during CNS growth by plasma assisted CVD process [Chen 2005-123111, Teo 2001-1534, Hofmann 2005-034308]. Raman spectra in Figs 4-5 showed a low intensity ratio of the G band to D band ($I_G/I_D < 0.36$) for samples with the Co catalyst deposited for < 60 s, indicating that a

significant amount of a:C was deposited on the AAO template during the CNS growth. The occurrence of the a:C deposit appeared to be closely related to the distribution of CNSs grown out of the AAO pores. The a:C was heavily deposited around CNSs, but became scarce away from the CNSs. This suggests that the CNS growth was accompanied by concurrent a:C deposition in the AAO pore channel.

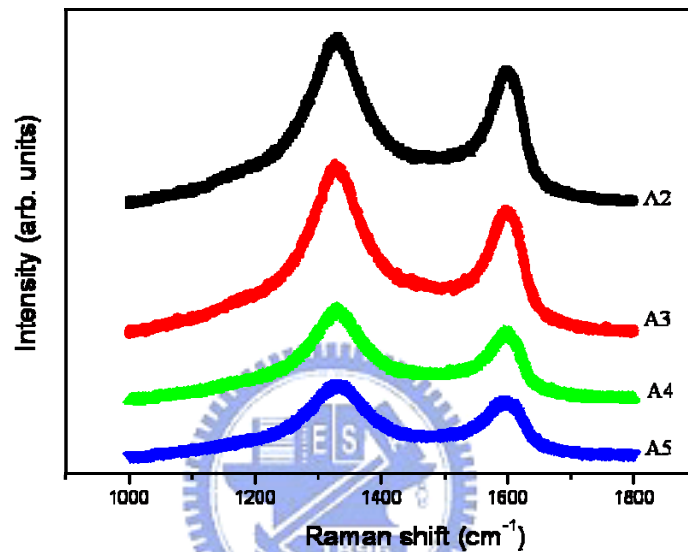


Fig. 4-5. Raman spectra of the as-deposited carbon nanostructures under different Co electroplating times. (SP. #A2-5)

Fig. 4-6 shows the cross-sectional SEM images of CNSs grown in the AAO template. CNSs grown with a smaller Co particle size were seriously distorted in shape and some were capped in the AAO pore channels (marked by circles) by the a:C deposit as shown in Fig. 4-6(a) for the Co catalyst deposited for 60 s. Most CNSs had a diameter smaller than the AAO pore size and those CNSs extending out of the AAO pores had a gradual decrease in the tube diameter along the tube shaft. It can be clearly seen that the lower part of CNSs inside the pore channels were embedded by lumps of precipitate (marked by arrows). For those pore channels from which CNSs were completely detached during SEM specimen preparation, the pore wall surface exhibited scaly and wrinkled feature, suggesting that CNF growth was

accompanied by precipitation of, probably, a:C. On the other hand, according to Fig. 4-6(b), CNSs grown with the Co catalyst deposited for 90 s had the growth direction much more compliant with the pore channel, and were vertically aligned after extending out of the pore. Fig. 4-6(c) shows the SEM image of the AAO template treated with the same CNS deposition condition but without the Co catalyst. The top portion of the AAO exhibited a clean but jagged feature, suggesting that the AAO template surface was subject to plasma etch during the plasma-assisted CVD (PACVD) process. It has been reported that CNTs/CNFs could be grown in the AAO template without metallic catalysts^[Lee 2001-2387, Yao 2001-11395]. However, no CNF or CNT growth was observed in the study, and the pore wall surface was very smooth. The observation implied that the Co particle played a major role not only catalyzing the CNF or CNT growth but also facilitating deposition of the a:C residue.

TEM image of an FIB prepared sample with the Co catalyst deposited for 90 s is shown in Fig. 4-7(a). The CNF growth time of the sample was deliberately controlled to keep the length of the CNFs smaller than the height of the AAO pore channels. It can be clearly seen that cone-shaped catalyst particles were present at the tip of the CNFs, indicating that the CNF growth in the AAO template was via the tip-growth mode. Because some Co particles remained at the pore bottom of the AAO template, the electroplated Co particle must be ripped apart during the CNF growth. Co particle fragments were also observed inside the CNF shaft. Fig. 4-7(b) shows the TEM image of several nanofibers grown with the Co catalyst deposited for 90 s. The CNFs were separated from the AAO template by ultrasonic agitation in ethanol. Some Co particles were stuck to the root of the CNFs. They were likely those originally left at the AAO pore bottom during the CNF growth but detached from the pore channels with the CNFs during TEM sample preparation.

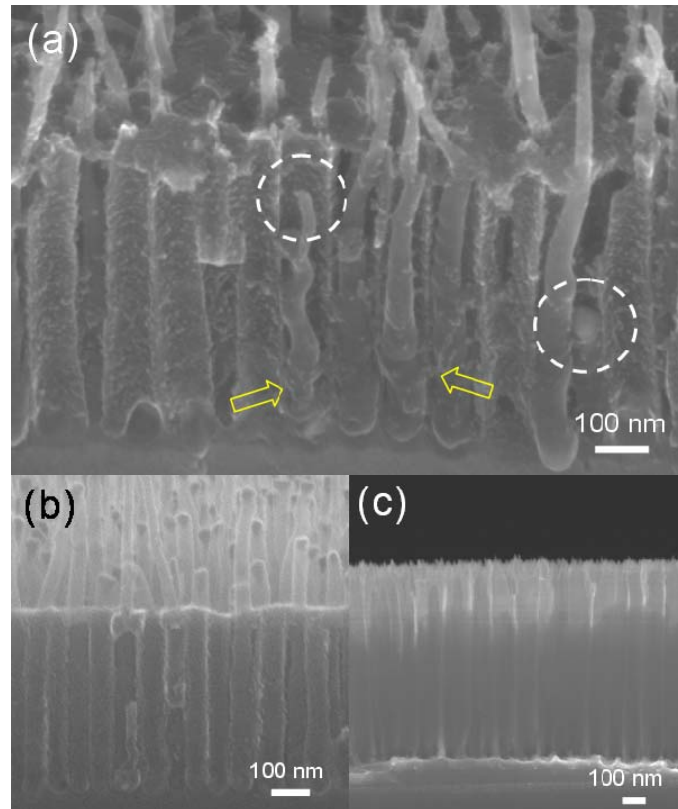


Fig. 4-6 Cross-sectional SEM images of the as-deposited CNSs in nanopores of AAO template under different Co electroplating times: (a) 60, (b) 90 and (c) 0 s. (For SP. # A3, A5 and A1, respectively)

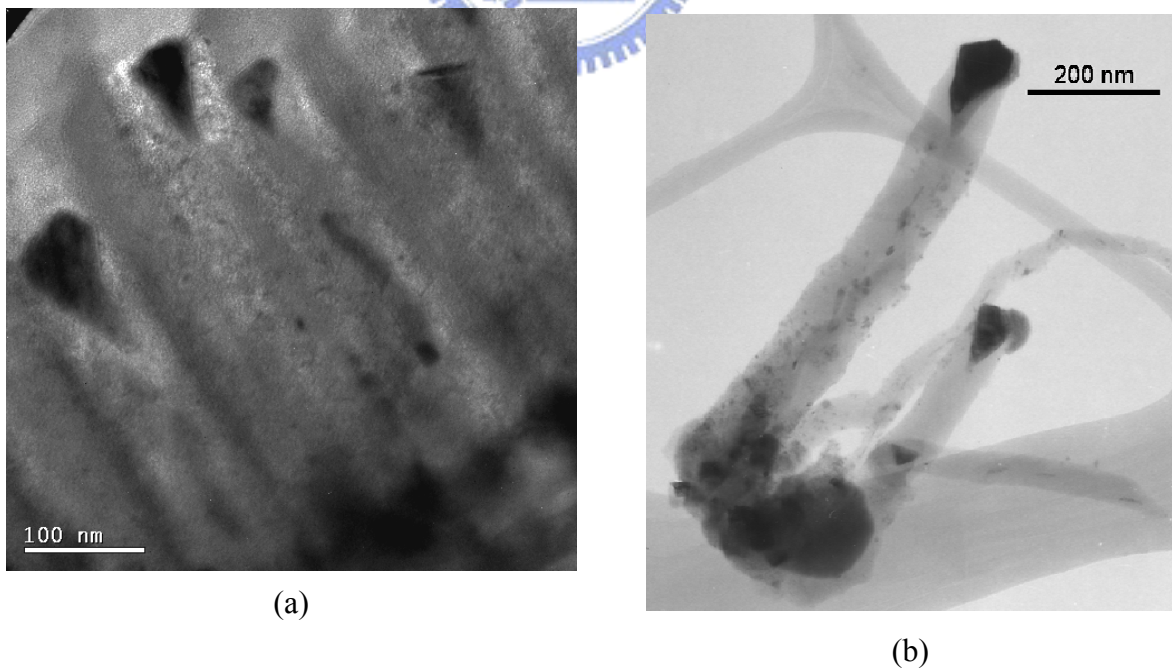


Fig. 4-7 TEM images of the Co-assisted CNSs: prepared by different sampling techniques: (a) FIB and (b) ultrasonic agitation. (SP. #A6, and A5, respectively)

Fig. 4-8 are the HRTEM image of the CNFs grown on AAO template at the Co deposition time of 60 and 90 s; The CNF was removed from the substrates by ultrasonic cutting and dispersed onto Cu TEM grids. The MWNT was 30 nm in diameter and exhibited a bamboo-like structure. Disordered amorphous carbon was found on the surface of the tube. The tube contained 34 well-ordered graphitic walls and the interwall distance (d_{002}) was approximately 3.7 Å. Compared to the CNFs grown at Co deposition time 75 s, the number of graphitic wall for the tubes increased to 53 and larger diameter about 45 nm was observed. When the Co deposition time was increased to 90 s (in Fig. 4-7(b)), the diameter of CNF increased to 55 nm and the tube contains 61 graphitic walls. The increase of the tube diameter observed in Fig. 4-4 resulted from the progressive increase in the number of graphene layers with the expanding catalysts volume.

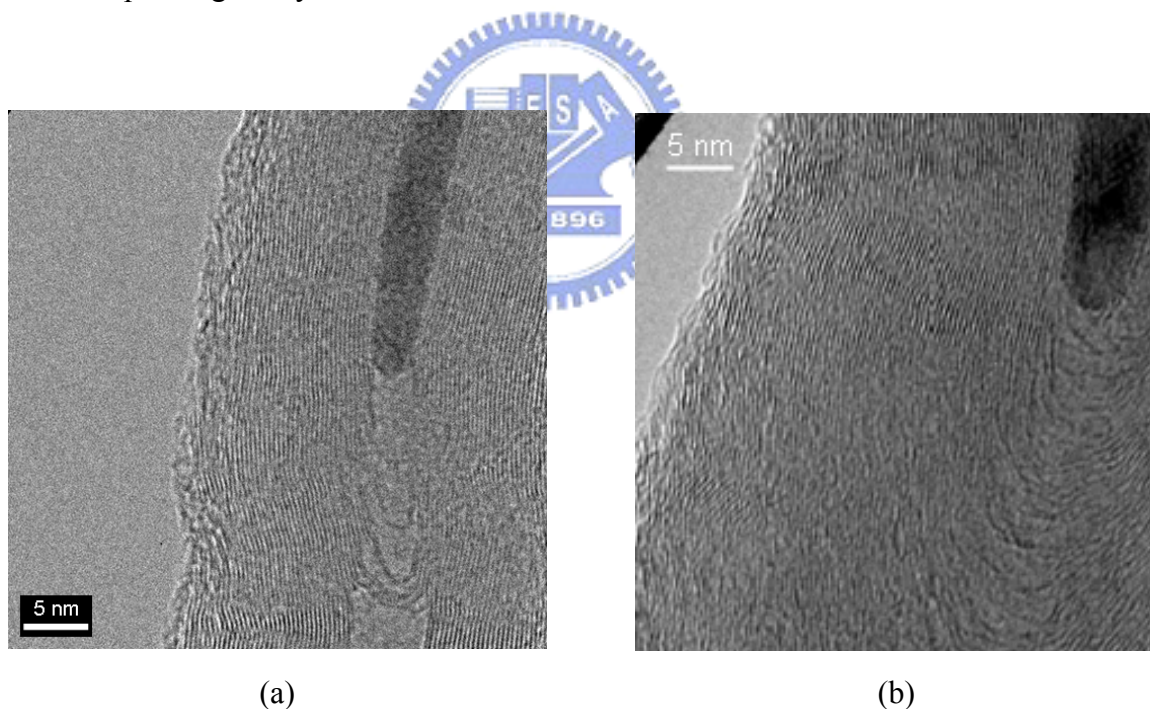


Fig. 4-8 HRTEM images of CNFs near the tip under different Co electroplating times: (a) 60 and (b) 90 s. (For SP. # A3 and A5)

4.2.3 On number density of the CNSs and growth mechanism discussion

The vapor-liquid-solid model is a commonly accepted CNT/CNF growth mechanism, which suggests that carbon diffusion in the liquefied metal catalyst is a required step for CNF

growth. The cone-shaped catalyst and the segmentation of Co particles shown in the TEM images is an implication of Co liquefaction during the CNF growth in the AAO template. It has been proposed that a temperature gradient can be developed in the catalyst particle as the concentration distribution of the dissolved carbon is nonuniform in the particle [Kanzow 1998-525]. The catalyst has a higher temperature in the region supersaturated with carbon, and graphene sheets develop from the region with a smaller carbon concentration [Harutyunyan 2005-153113]. The particle segmentation probably resulted from the temperature gradient developing in the Co particle. The top portion of the Co particle was liquefied earlier than the bottom portion due to the quicker supersaturation with carbon, which was supplied by the inflowing carbonaceous plasma species under the CNF growth condition. As the liquefied Co particle moved upward with the growing CNF shaft, the Co particle was eventually separated leaving the unliquefied part at the bottom of the AAO pore channel. Besides, because Co has a reasonable wetting strength with aluminum oxide [Wang 2004-081401, Chambers 2002-827], it was likely that capillary force might assist lifting the liquefied Co particle and thus allow easy precipitation of graphitic sheets.

As discussed above, CNF growth on the AAO template was accompanied by deposition of a:C, and more a:C was deposited for a smaller Co particle. The a:C accumulation on the pore wall surface could hinder the motion of the liquefied catalyst particle in the pore channel, thereby changing the moving direction and geometric shape of the catalyst during the CNF growth. This can explain why most CNFs grown under a condition of heavy a:C deposition showed a twisted feature inside the pore channels and had a fiber diameter smaller than the AAO pore size. In addition, from Fig. 4-7(b), many nanosized particles, probably Co, adhered to the tube surface of the CNFs. It is possible that the rough wall surface of the AAO pore channel, resulting from the a:C deposition, disturbed the movement of the liquefied Co particle on the tip of the growing CNF, and thereby stripped off surface atoms from the Co catalyst particle, which might later agglomerate and adhere to the growing CNFs.

The growth mechanism of CNFs in AAO pore channels is schematically illustrated in Fig. 4-9. Because the AAO pore channels not only limit the flow direction and the flux of plasma species toward the Co catalyst but also define the exposing area of the Co particle, the impinging rate of carbonaceous and hydrogen radicals and ions onto the catalyst surface should be independent of the height of the Co particle. Once adsorbed and decomposed on the Co catalyst surface, carbon species may diffuse on the surface and dissolve into the particle. The Co particle becomes supersaturated with carbon on the top region earlier than the lower part, resulting in the development of a temperature gradient in the particle and thus Co liquefaction occurs earlier in the top region. Carbon atoms precipitating at the bottom of the liquefied Co segment then grow into graphitic sheets, forming carbon nanofibers in the AAO pore channel via the tip-growth mode. Because etching the a:C deposit by plasma species is not effective in the pore channel due to the high aspect ratio, removal of carbonaceous deposit in the pore channel is more sluggish than on the AAO template surface. Carbon dissolution into the Co particle becomes the major pathway for reducing surface concentration of the carbon deposit. Because carbon becomes saturated more quickly in the smaller particle than the bigger one, more a:C may remain on the particle surface. If the a:C deposition prevails over CNF growth, extensive a:C accumulation can occur on the top of the catalyst and the pore wall, thus retarding the CNF growth. The a:C deposit can modify the geometric shape of the liquefied catalyst and thus diminish active catalytic area, thereby leading to growth of CNFs with a smaller diameter and a distorted shape. In the extreme situation, the pore opening may be completely blocked by the a:C deposit before the CNF grows out of the pore, thus terminating the inflow of the precursor species and stopping the CNF growth. On the other hand, the bigger Co particle dissolves more carbon atoms and, therefore, accumulation of a:C on the surface can be effectively diminished, making CNF growth in the pore channel more favorable. Once CNFs grow out of the AAO pore surface, plasma etch become effective to remove excessive carbon deposit on the Co catalyst and plasma precursors can reach the

catalyst surface without much obstacle. Thus CNFs can be grown continuously under a growth condition similar to that in an open space.

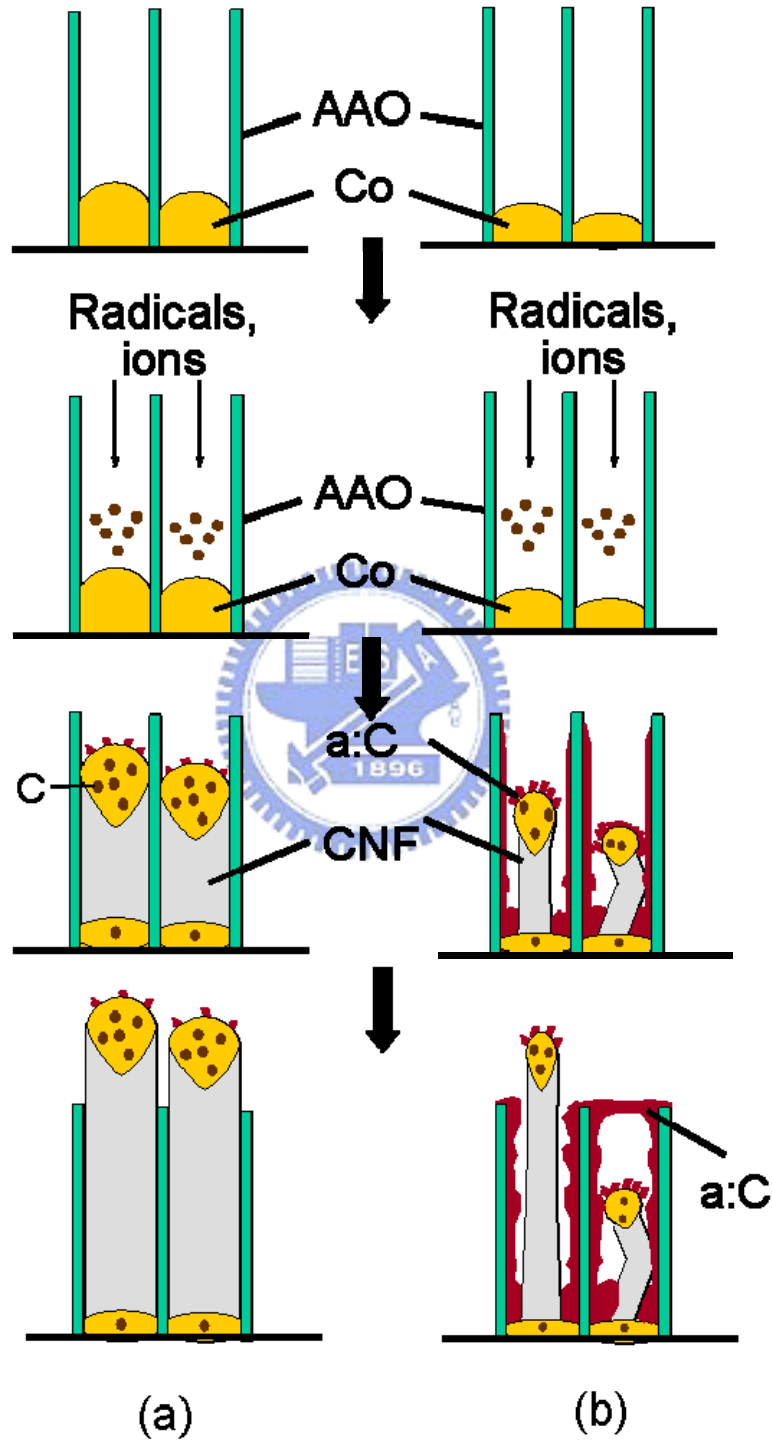


Fig. 4-9 Schematic illustration of carbon nanostructure growth mechanism in the AAO pore channel with different Co plating time: (a) 90 s and (b) 60 s, respectively.

4.2.4 On field emission properties of the CNSs

To compare field emission properties of CNFs grown on the AAO template for different Co deposition times, the field emission current density (J) as a function of electric field (E) curves were shown in Fig. 4-10(a). The lowest turn-on field (E_{to}) 5.08 V/ μm , where E_{to} is defined as the electric field required to produce an emission current density of 0.01 mA/cm², was found at the CNFs on the AAO template under Co electroplating time 60 s. On the other hand, CNFs grown with the Co catalysts deposited for 90 s had the highest turn-on field E_{to} 7.35 V/ μm . This indicated the template-assisted CNSs with high packing density, highly vertical aligned and uniform diameter does not ensure a better field emission. The CNFs grown with the Co catalyst deposited for 60 s had a smaller diameter with a higher local field and an optimal tube number density to prevent a larger field screening effect^[Nilsson 2000-2071]. The corresponding Fowler-Nordheim (F-N) plot for the J-E curve of the CNFs under Co electroplating 60 s was shown in the inset of the Fig. 4-10. Two linear segments with a slope of about -14700 in the low field regime and a slope of about -6100 in the high field regime. Non-linearity of F-N plot could be attributed to the space charge effects^[Xu 2003-19], interactions between neighboring nanotubes^[Collins 1997-9391], dielectric barrier layer existence^[Tanaka2004-1651] and surface adsorbate effects^[Dean 2000-2071]. In Fig. 4-4(b) and Fig. 4-6 (a), a:C byproduct was clearly seen on the CNFs and it could modify the local work function and altered field emission characteristics. Electrons emitted from CNF tips need to overcome the extra energy barrier imposed by a:C and this can cause deviation of the field emission from the normal F-N characteristics in the high emission current regime.

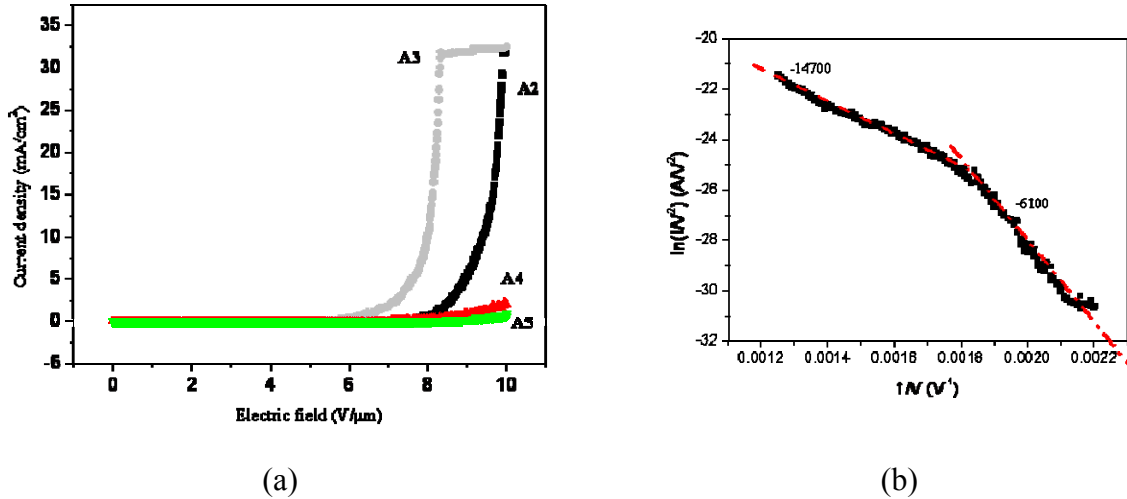


Fig. 4-10 (a) J-E curves of the as-deposited AAO-assisted CNSs under different Co electroplating times. (SP. #A2, A3, A4, A5, respectively) and (b) is the F-N plot of the SP. #A3.

4.3 Effects of the processing parameters of the field emitter arrays

4.3.1 Effect of the CNSs growth time on SiO₂ film morphology

To fabricate AAO-assisted emitter arrays, CNSs are first grown on the AAO template under Co electroplating time 1 min. Then the dielectric layer and the gate electrode layer were directly deposited on the CNS emitters. The morphologies of CNSs embedded in the SiO₂ dielectric layer of 1.5 μm in thickness are shown in the cross-sectional SEM micrograph of Fig. 4-11. When the CNS growth time is 35 min as shown in Fig. 4-11(b), the length of the CNSs extending out of the AAO template is over 500 nm and the surface of the SiO₂ dielectric layer become rugged. The surface roughness of the SiO₂ dielectric layer could be decreased by reducing the length of CNSs extending out of AAO channels or increasing the thickness of the SiO₂ layer. Therefore an appropriate combination of the length of CNSs and the thickness of the dielectric layer is crucial to photolithographically define the pattern of the field emission arrays.

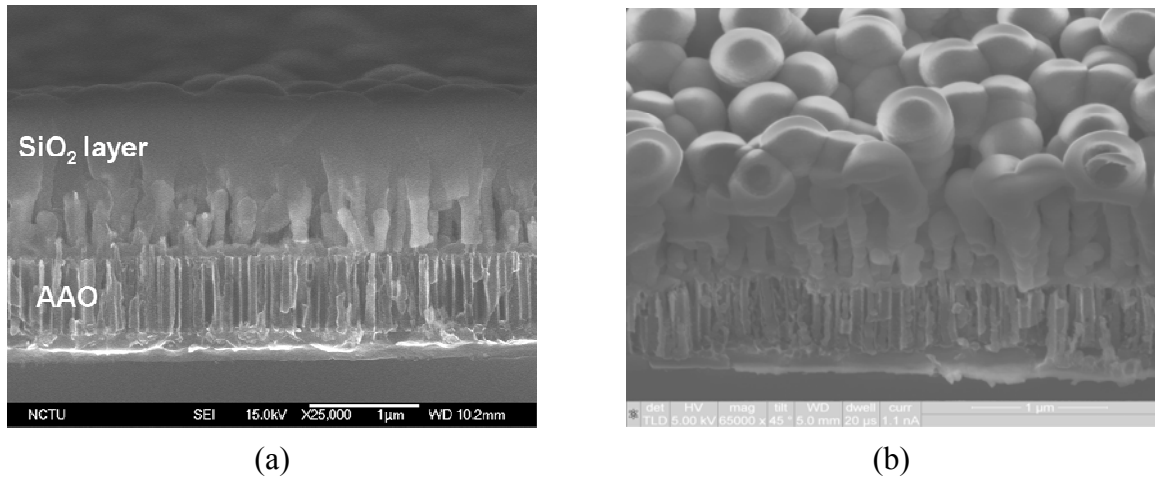
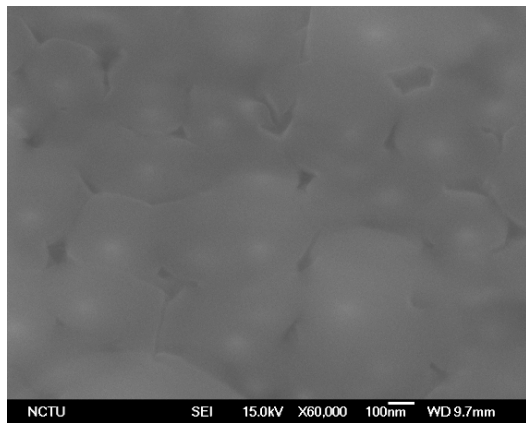


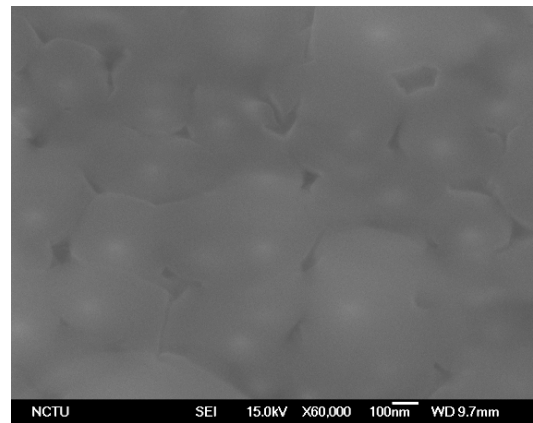
Fig. 4-11 SEM side view images of the SiO₂-coated CNSs for different CNS growth times (a) 30, and (b) 35 min, respectively.

4.3.2 Effect of the etching times and methods on emitter morphology and CNSs Raman spectra

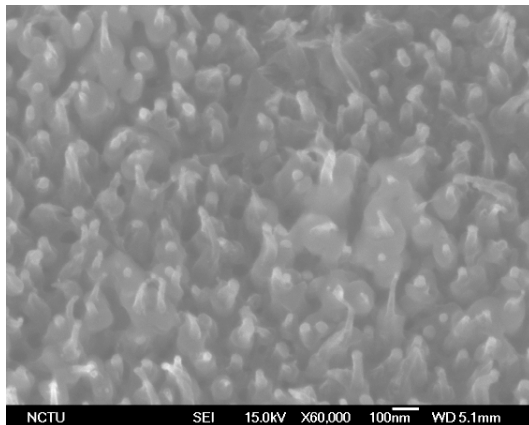
After photolithography, the Al gate layer was etched by RIE. The silicon dioxide dielectric layer was then partially removed by RIE using a 50/50% mixture of CHF₃ and Ar (with a gas flow of 80 sccm) as the gas source at a pressure of 10 mTorr. Fig 4-12 shows the SiO₂-coated CNSs after RIE etch for different times. It is generally believed that ion sputtering can alter the microstructure of carbon nanotubes and thus alter the field-emission property. Carbon nanostructures would suffer from ion bombardment as the CNSs in the array pattern were exposed to the plasma during the etch of the SiO₂ dielectric as shown in the Fig 4-12(f). During the reactive-ion-etch of the SiO₂ dielectric layer, a mixture of CHF₃ and Ar was used, and thus CNSs were subject to bombardment of various ions, including hydrogen, fluorine, argon and fluorocarbon ions. It has been reported that hydrogen ion bombardment could increase C-H bondings in CNSs and resulted in a more disordered microstructure [Zhi 2002-1690]. On the other hand, fluorination occurs on the CNSs when CNSs are treated by fluorocarbon plasma, such as CF₄ [Plank 2003-2426, Felten2005-074308].



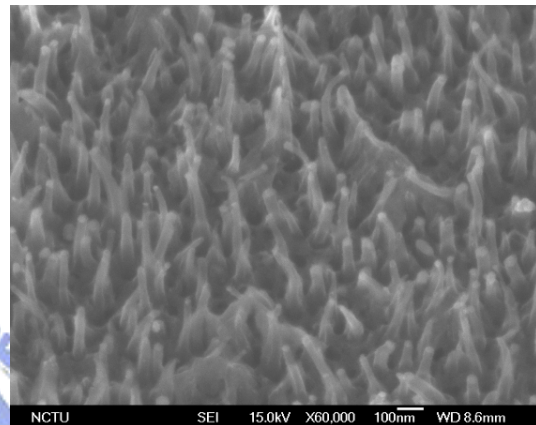
(a)



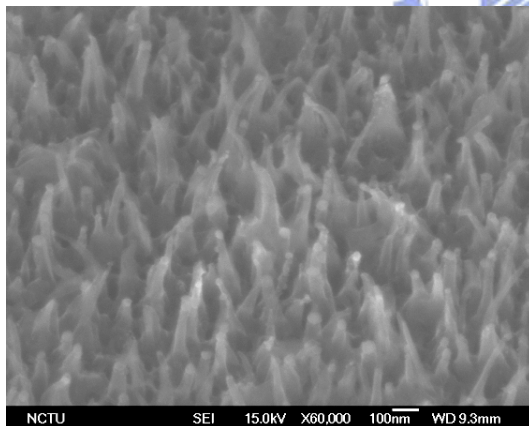
(b)



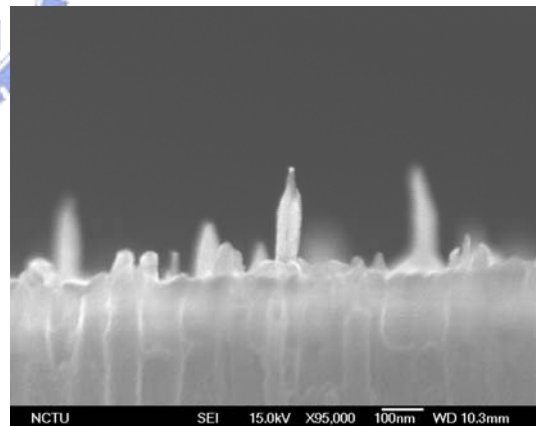
(c)



(d)



(e)



(f)

Fig. 4-12 SEM images of the SiO₂-coated CNSs after RIE etch for (a) 240 s, (b) 300 s, (c) 360 s, (d) 420 s, (e) 480 s and (f) higher magnification of (e). (SP. #A9, A11, A12, A13 and A14 respectively)

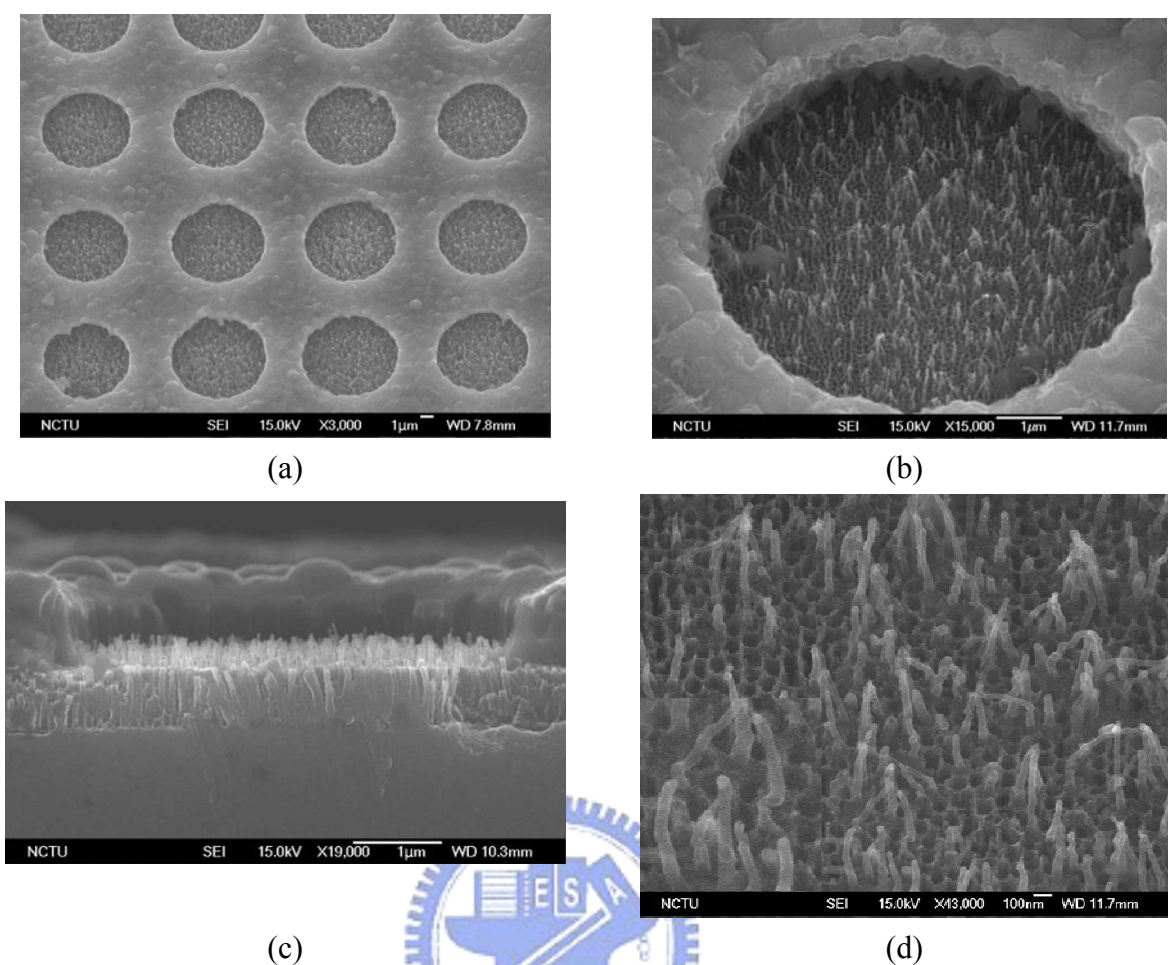


Fig. 4-13 SEM images of the as-prepared AAO-assisted emitter arrays: (a) top-view of emitters, (b) higher magnification of (a), (c) side-view of (b), and (d) higher magnification of (c), respectively. (SP. #A10)

With optimal RIE process for 270 s, the remnant SiO_2 on the CNSs was then completely removed by BOE wet etch for 5 s. Fig. 4-13 shows the SEM image of the AAO-assisted emitter arrays fabricated as described. The open emitting area is $6.5 \mu\text{m}$ in diameter and $2 \mu\text{m}$ in depth. The RIE process to remove partial SiO_2 dielectric layer seemed not to cause obvious damage. Fig. 4-13(a) shows the SEM image of the AAO-CNS emitters after the dielectric layer was removed by RIE etch for 270 s, followed by BOE etch for 5 s. It can be clearly seen that Co catalyst particles were still present at tips of the CNSs implying that the RIE etch induced little damage to the AAO-assisted CNSs. Difference in the length and density of CNSs between the as-prepared AAO-assisted CNSs and that after the removal of the dielectric

layer was hardly perceivable.

Fig. 4-14 shows Raman spectra of the as-grown CNSs on the AAO template and that after the removal of SiO₂ by RIE and BOE etches. The two prominent Raman peaks are located at ~1325 cm⁻¹ (D band) and ~1598 cm⁻¹ (G band). The former is due to the ring stretching mode in a disordered graphitic structure and the later sp² bond stretching mode [Tamor 1994-3823, Ferrari 2000-14095]. Peak features of both Raman modes, such as peak position and intensity, are commonly used to study the insight of the crystallinity and graphitic bonding of CNSs. The ratio of the integral intensities of the G and D bands, I_G/I_D , can be used to estimate the microstructure disorder of carbon nanotubes. The SiO₂ encapsulated sample had an I_G/I_D ratio about 0.46 after the RIE and BOE etches, and this value was close to that of the as-prepared AAO-assisted CNSs, ~ 0.5. In addition, the two Raman peaks of the etched sample had no apparent peak shift as compared to the counterparts of the as-prepared AAO-assisted CNSs, suggesting that removal of the SiO₂ dielectric layer by RIE and BOE etches did not cause significant chemical and microstructure damage to the CNSs.

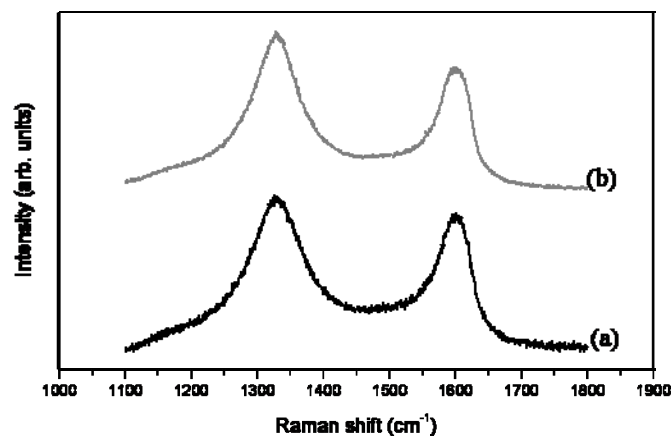


Fig. 4-14. Raman spectra of (a) the as-deposited CNSs and (b) the as-prepared AAO-assisted emitter arrays. (SP. #A3 and A10)

4.4 Field emission properties of the emitter arrays

Field-emission measurement of the AAO-catalyst-assisted CNSs emitter arrays was conducted under a vacuum condition of $\sim 10^{-6}$ Torr with a simple diode measurement configuration. A cylindrical probe was placed 100 μm above the AAO-assisted CNS emitters arrays without any electrical connection to the Al gate electrode. The measured field emission current density (J) as a function of the electric field (E) was plotted in Fig. 4-15. The anode turn-on electric field (E_{to}), which is defined as the electric field required to produce an emission current density of 1 mA/cm^2 , was ~ 8.05 $\text{V}/\mu\text{m}$. The measured E_{to} was slightly higher than that of AAO-assisted CNS emitters with a similar tube density grown on a blanket AAO template previously reported [Chen 2005-123111]. The emission current density of the AAO-assisted CNS emitter arrays at an anode-cathode voltage of 8.1 $\text{V}/\mu\text{m}$ was about one fourth of that of the blanket sample. Because the emitter arrays occupied only one third area of the AAO template, it is expected that the measured field emission density should be smaller for the emitter arrays. The F-N plot shown in the inset of Fig. 4-15 exhibited two linear segments. The two-segment feature of the F-N plot has been reported in chapter 4.2.4 and it may be due to the amorphous carbon residual deposited on the CNCs.

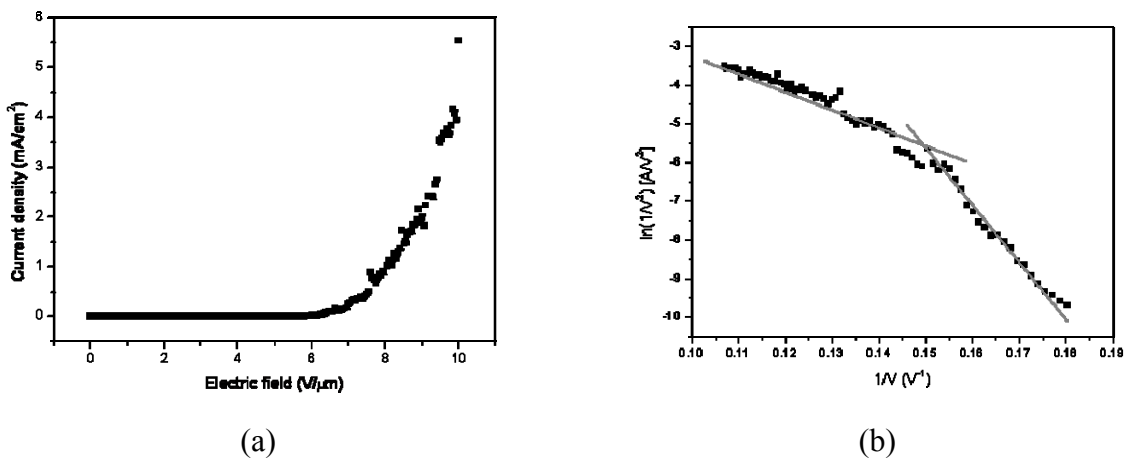


Fig. 4-15 (a) J-E curve of the AAO-catalyst-assisted CNSs emitter arrays and (b) is its corresponding F-N plot. (SP. #A10)

4.5 Summary

Using AAO template with vertical pore channels, vertically-aligned CNSs were grown in the AAO template by ECR-CVD using electroplated cobalt as the catalyst. The tube density, diameter and tube alignment of CNSs grown in AAO pore channels strongly depended on the size of the electroplated Co particle. Carbon dissolution in the Co particle at the bottom of the pore channel induced a temperature gradient and Co melting in the particle, leading to the segmentation of the Co particle in the AAO pore channel. When the Co catalyst particle was small, heavy deposition of a:C took place in the pore channel under the plasma assisted CVD condition, and the CNS growth was adversely affected. A growth mechanism was proposed to delineate the effect of the Co catalyst size on the CNS growth confined in the AAO pore channels. For emitter arrays fabrication, standard IC process techniques are used on the vertically aligned CNSs with AAO template and an anode turn-on electric field of $8.1 \text{ V}/\mu\text{m}$ was obtained for the emitter arrays.

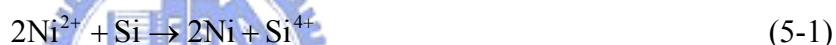


Chapter 5

Results and discussion for the electroless plating catalyst-assisted process

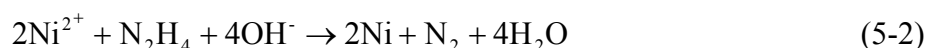
5.1 Compositions of the catalyst films by XPS and EDS

The electroless plating process involves a continuous buildup of metal coating on a substrate by the mere immersion in a suitable aqueous solution. In this research, Si substrate is first coated by a 150 nm-thick a:Si and a:Si layer is acted as a catalytic surface and the catalytic surface is the only place where electroless plating occurs. Silicon can be made catalytic for electroless deposition by replacing the surface Si atoms, for example:



The reaction is called displacement deposition, because the Ni ions in solution simply displace the silicon at the surface [Ting 1989-456]. Once the deposition starts on a surface, the deposited metal must also be catalytic for the deposition to continue.

During the electroless plating process, there are no external electrodes present, but there is charge transfer involved. Instead of an anode, the metal is supplied by the metal salt and a substrate serves as the cathode. A chemical reducing agent in solution supplies the electrons for converting metal ions to the metal form. For example, Ni alkaline bath used in this research is composed by a metallic salt $\text{NiSO}_4 \cdot 6\text{H}_2\text{O}$ and a reducing agent N_2H_4 and their reaction could be written as following:



As deposition progresses, islands are formed around these nucleation sites. These islands grow in size until they merge and a continuous film results. Here, hydrazine is used as the reducing agent because the purity of the electroless Ni deposits produced from hydrazine

solutions could be contain up to 99% Ni [Schlesinger 2000-673]. Two other common reducing agents, hypophosphite and sodium borohydride, yield electroless Ni films containing phosphorus (Ni-P) and boron (Ni-B). The chemical analysis of the as-plated Ni film (SP. #B3) by electroless plating is examined by EDS as shown in the Fig. 5-1. Ni, Si, O, and S signals are observed in the EDS spectrum. The result indicates that Ni could deposit on the a:Si surface by electroless plating from a metallic salt $\text{NiSO}_4 \cdot 6\text{H}_2\text{O}$ and a reducing agent N_2H_4 . The S signal in the EDS spectrum may result from the metallic salt residue. XPS analysis also show a typical Ni XPS signals in Fig. 5-2(c), Ni $2p_{3/2}$ peak and Ni $2p_{1/2}$ peak exists with a difference of 17.4 eV but the binding energy of Ni $2p_{3/2}$ locate at 857 eV BEs and present a

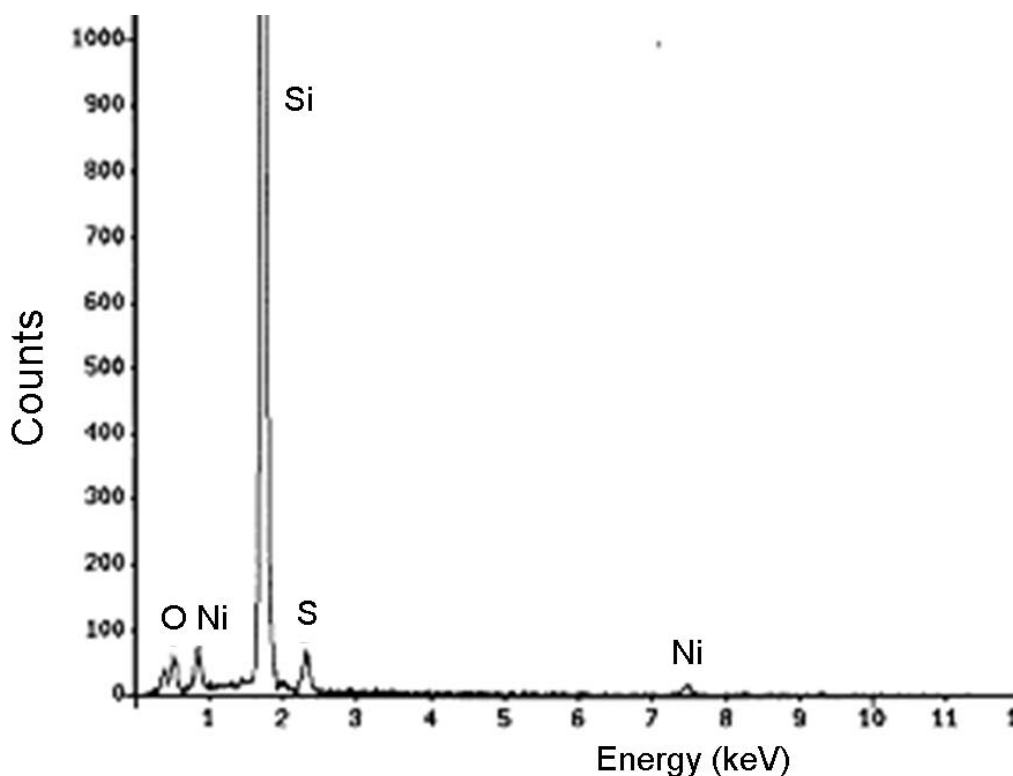


Fig. 5-1 EDS spectrum of the as-plated Ni catalyst films on a:Si/Si substrate by electroless plating (SP. #B3).

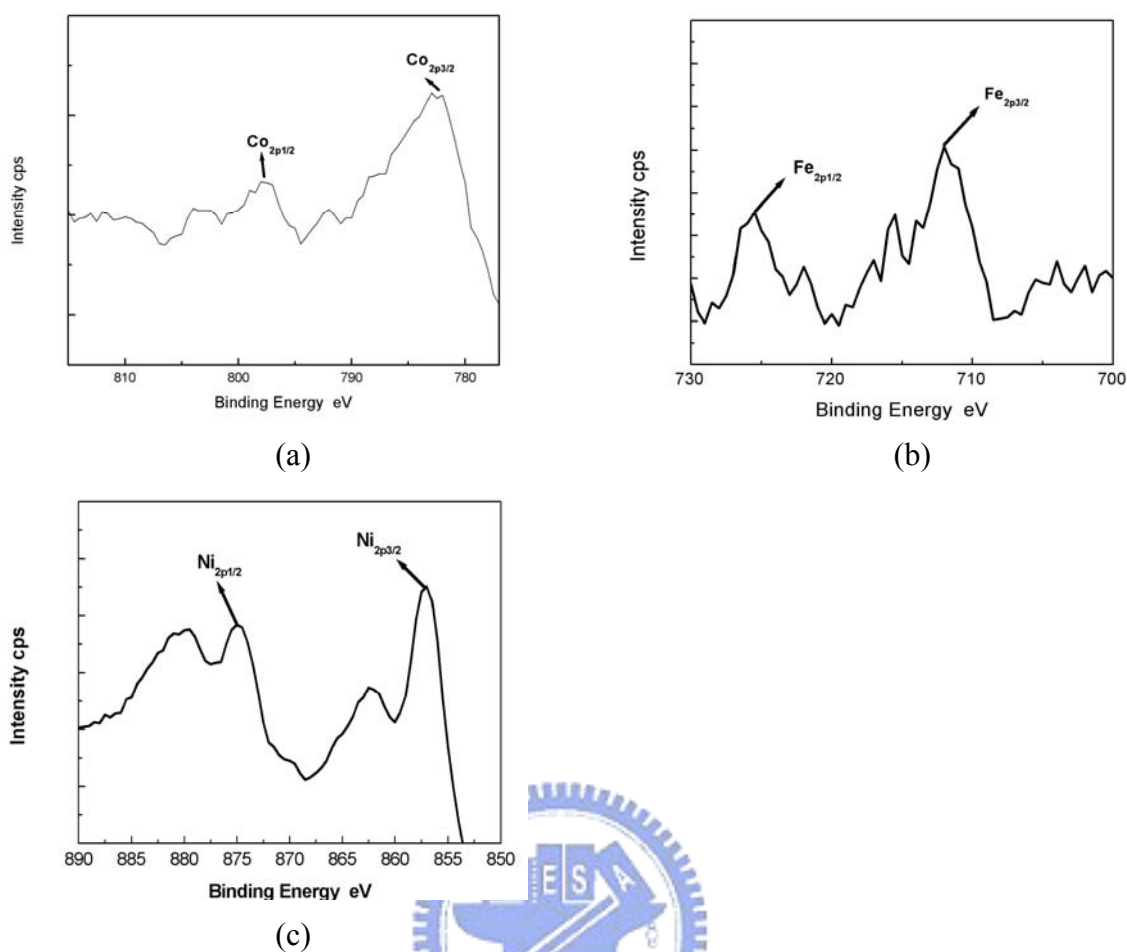


Fig. 5-2 XPS spectra of the as-plated catalyst films on a:Si/Si substrates for different catalyst materials: (a) Co, (b) Fe and (c) Ni. (SP. # B1, B2 and B3, respectively)

negative shifted 4 eV with respect to pure Ni _{2p3/2}. This result indicate the Ni films could deposit by electroless plating on the a:Si/Si substrate and the BE shift may be due to the oxidized phased forming when specimen was exposed to the air. Two other catalyst materials, Co and Fe films (SP. #B1 and B2) plated on the a:Si/Si substrate using $\text{Co}(\text{NO}_3)_2 \cdot 6\text{H}_2\text{O}$ and $\text{Fe}(\text{NO}_3)_3 \cdot 9\text{H}_2\text{O}$ metallic salts and their XPS spectra are shown in Fig. 5-2 (a) and (b), respectively. In the Fig. 5-2(a) and (b), Co 2p peaks and Fe 2p peaks also present a negative shifted about 4 eV with respect to pure element. These results indicate the Co and Fe films are deposited by electroless plating on the a:Si/Si substrate and the BEs shift may be due to the oxidized phased forming when specimen was exposed to the air.

5.2 Morphologies and lattice images of the catalyst nanoparticles and the as-deposited CNTs

Before CNT growth, as-plated catalyst films are pretreated by H-plasma for 10 minute in the MPCVD system. Catalyst nanoparticles are formed after H-plasma pretreatment as shown in the Fig. 5-3. In the Fig. 5-3(a), Co catalyst nanoparticles have a similar number density around 100 particles/ μm^2 and a diameter distribution from 30 to 65 nm. Denser Fe catalyst nanoparticles are observed in Fig. 5-3(b) with a number density around 150 particles/ μm^2 and a diameter distribution 20-50 nm. Ni catalyst nanoparticles in Fig. 5-3(c) have a similar number density with Co nanoparticles and their diameter distribution is 20-50 nm.

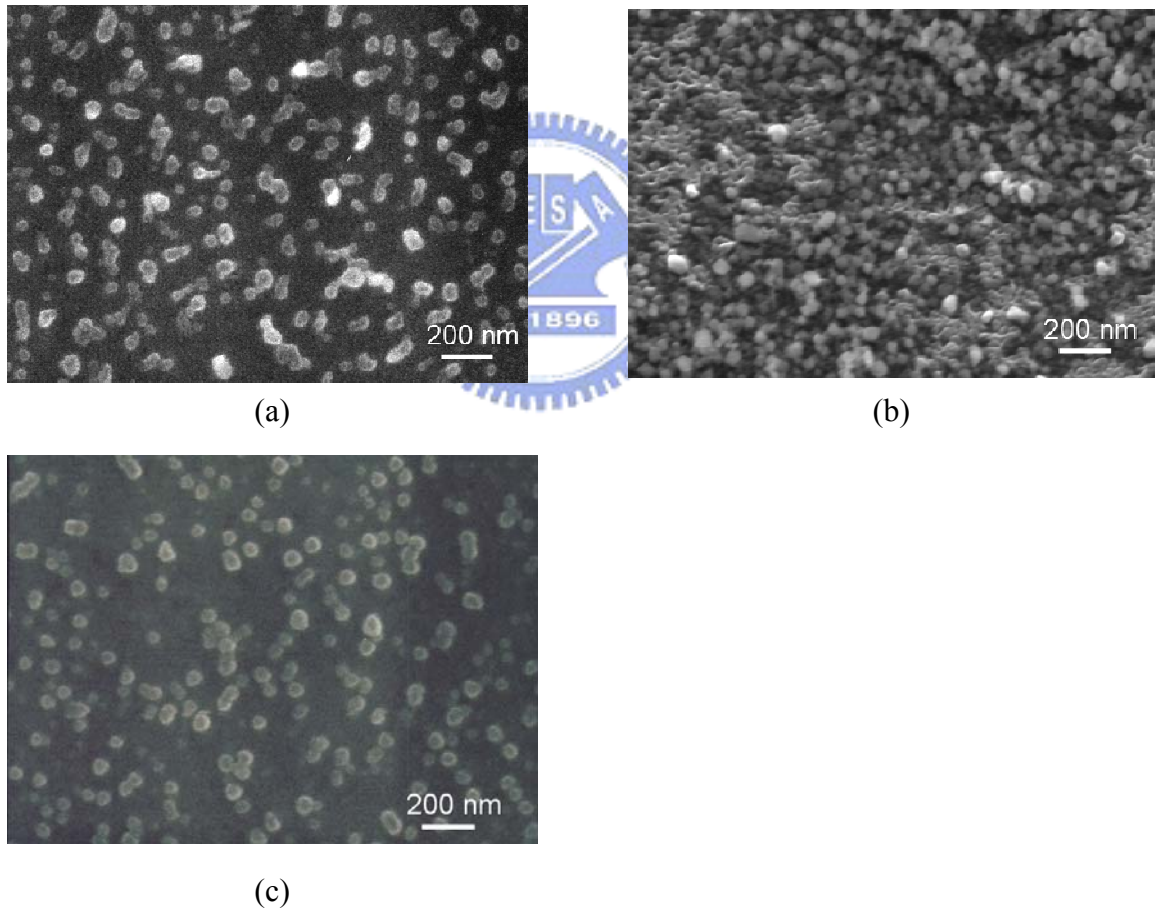


Fig. 5-3 SEM micrographs of nanoparticles after H-plasma pretreatment for different catalyst materials: (a) Co, (b) Fe and (c) Ni. (SP. # B1, B2 and B3, respectively)

Then the CNT growth is performed in the MPCVD system under the conditions: CH_4/H_2

= 1 sccm / 100 sccm, 800 W microwave power, under 16 Torr and 660 ~ 680 °C for 30 min. The morphologies of the CNTs grown from different catalyst Co, Fe, and Ni by electroless plating are shown in Fig. 5-4 (a), (b) and (c), respectively. The CNTs are all seemed to be randomly oriented and well distributed on the substrate and the feature of the tubes are listed in Table 5.1. From the observation in Fig. 5-4 (a), the CNTs grown from Co catalyst have 200-1200 nm in length and 25-40 nm in diameter, and a tube number about 600 tubes / μm^2 . For the Fe catalyst assisted CNTs in Fig. 5-4 (b), the similar tube length 200-1200 nm, diameter distribution 20-50 nm and a denser tube density about 800 tubes / μm^2 are found. In the Fig. 5-4 (c), the CNTs grown from Ni catalysts are 100-1200 nm in length, 10-30 nm in diameter, and much denser 2000 tubes/ μm^2 in tube number density. The Raman spectra of the CNTs grown from different catalyst materials are depicted in Fig. 5-5 and there are also two obvious peaks around ~ 1350 and $\sim 1580 \text{ cm}^{-1}$, which are belong to sp^3 -bonded (D band) and sp^2 -bonded (G band) carbon atoms, respectively. The higher intensity G band to D band ratio (I_G/I_D) is indicating high graphitization. There is a higher ratio about 2.0 for Ni catalyst-assisted CNTs, indicated that the CNTs grown from the Ni catalyst has better crystallization than Co catalyst and Fe catalyst. The ratio is about 1.1 for Co and 1.0 for Fe. The features of the CNTs grown from the catalyst by electroless plating as shown in Table 5-1 including the tube length, diameter, density, and Raman I_G/I_D ratio. The Average tube number grown from one catalyst particle is calculated from the ratio of the tube number density and the catalyst particle density. From the micrograph in the Fig. 5-4(c), the tube numbers are much more than the numbers of the catalyst particles in Fig. 5-3(c), and this maybe due to the numbers of the spaghetti-like CNTs can not be identified precisely. Table 5-1 also indicates that the CNTs for Ni catalyst give a greater tube number density and better graphitization but smaller in length and diameter.

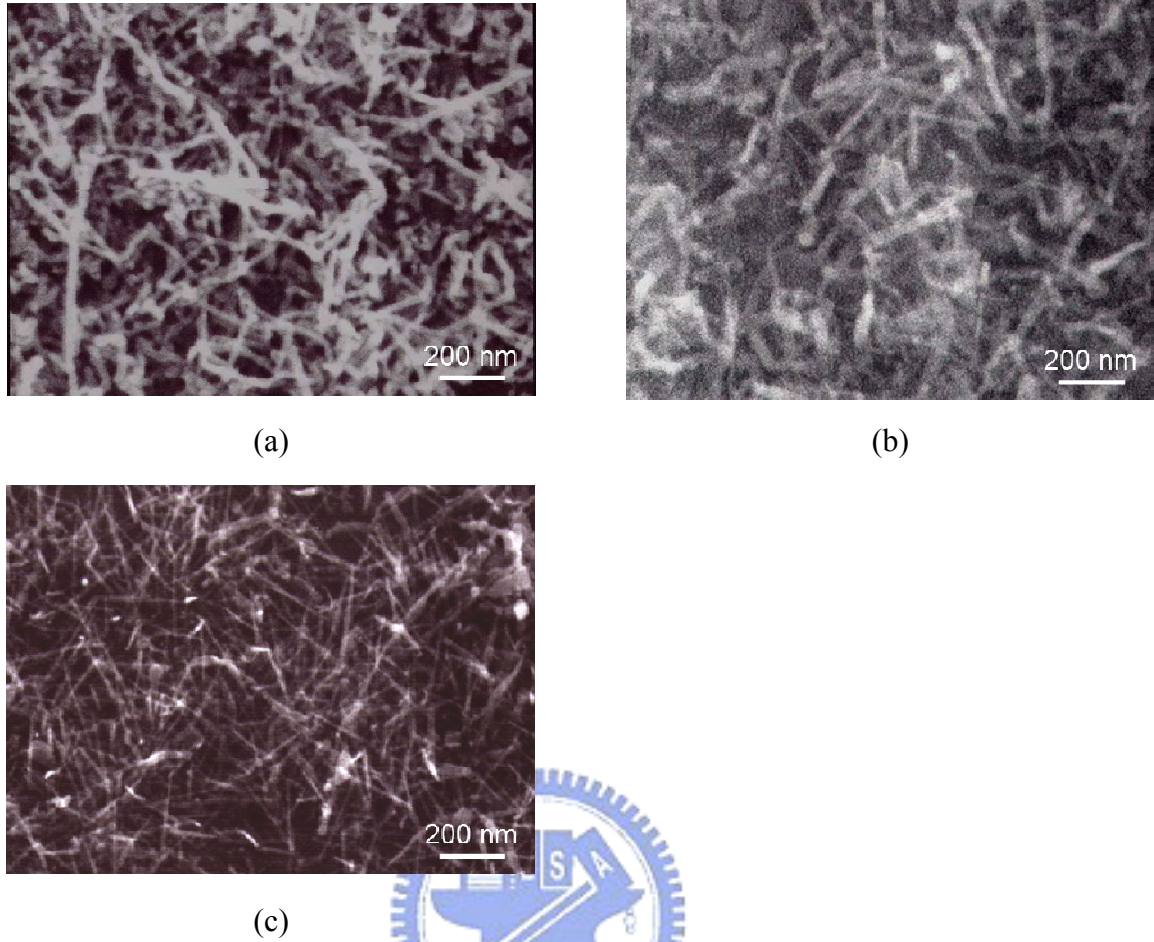


Fig. 5-4 SEM micrographs of the as-deposited CNTs for different catalyst materials: (a) Co, (b) Fe and (c) Ni. (SP. # B1, B2 and B3, respectively)

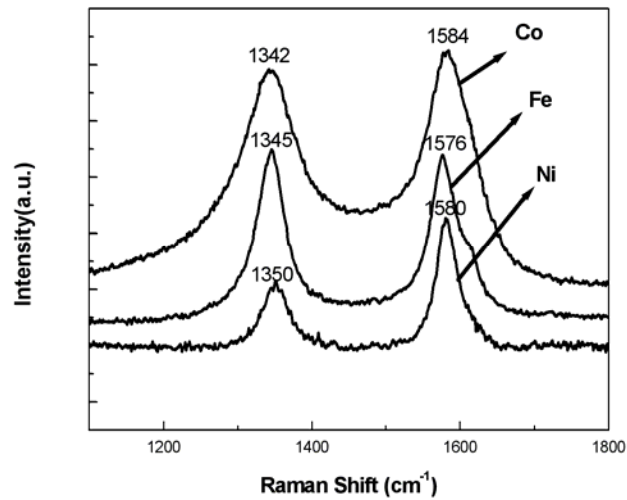


Fig. 5-5 Raman spectra of the as-deposited CNTs for different catalyst materials: (a) Co, (b) Fe and (c) Ni. (SP. # B1, B2 and B3, respectively).

Table 5-1 Comparison of the features of the electroless plating catalyst-assisted carbon nanotubes with different catalyst materials.

SP. #	B1	B2	B3
Catalyst material	Co	Fe	Ni
Electroless plating time (s)	40	120	40
Catalyst particle density (particles/ μm^2)	100	150	100
Tube length (nm)	200 ~ 1200	200 ~ 1200	150 ~ 1200
Tube diameter (nm)	25 ~ 40	20 ~ 50	20 ~ 40
Tube density (tubes/ μm^2)	600	800	2000
Raman I_G/I_D ratio	1.1	1.0	2.0

Fig. 5-6 is the TEM images of an as-grown CNT, depicting a base-growth bamboo-like MWNT with discrete Ni catalyst particles (about 5 ~ 15 nm in size). Base-growth mode could be determined that the CNT are grown from a catalyst particle on the substrate surface and there is no catalyst particle on the tip of the tube. The stronger bonding between catalyst and substrate may result from the NiSi_x silicide forming when the temperature reaches about 680°C during CNT growth in MPCVD for 30 min. This phenomena also found in other two catalysts Co, and Fe cases. It is also interesting to note that the bamboo-like CNTs were formed this may be due to the residual nitrogen on specimen during electroless deposition in plating solution N_2H_4 , NH_4Cl , or NH_4OH [Lin, 2003-1851]. HRTEM lattice image around a compartment of bamboo-like CNTs is shown in Fig. 5-7. The tube wall is composed of about 20~30 layers of graphene sheets, and widthwise side of the compartment consists of 10~15 graphene sheets.

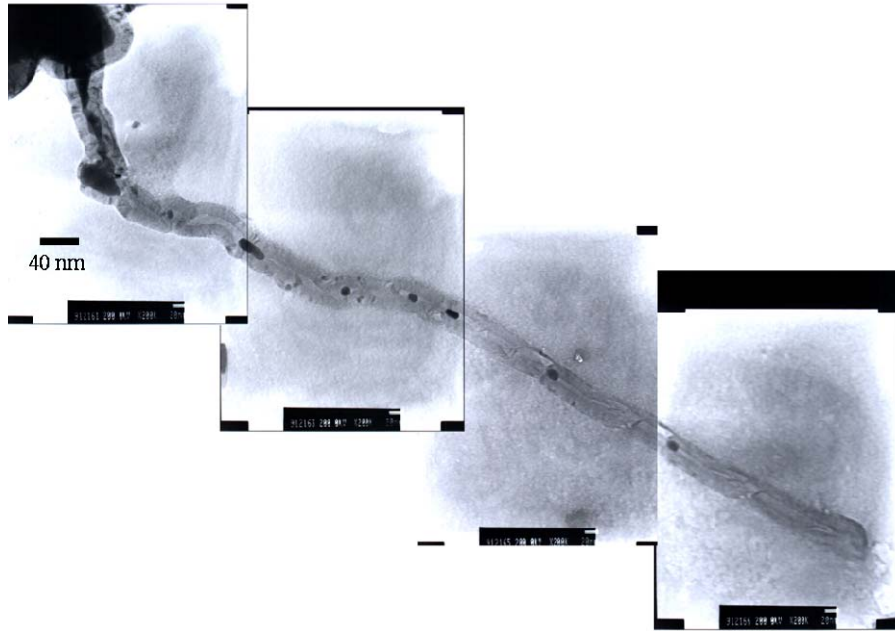


Fig. 5-6 TEM micrograph showing morphology of the as-deposited bamboo-like CNT with discrete Ni catalyst particles split from one original particle in the tube. (SP. #B3)

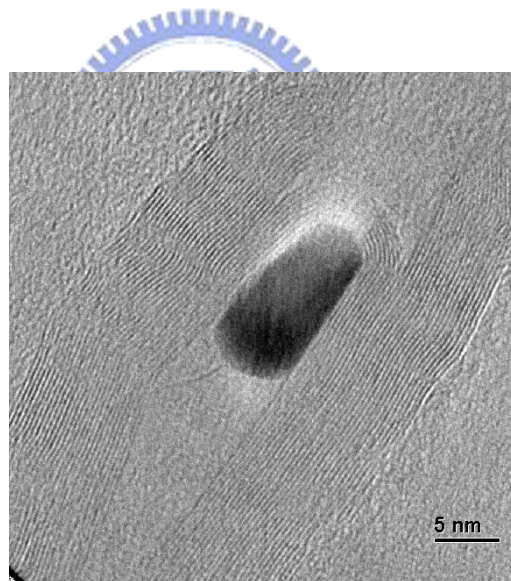


Fig. 5-7 HRTEM lattice image of a compartment of the tube around the Ni catalyst. (SP. # B3)

5.3 Auger spectra at different positions on the Ni catalyst-deposited pattern

In order to investigate the composition and distribution of the as-deposited catalyst pattern, the Ni-patterned Si wafer was examined by AES at Positions 1, 2 and 3 in Fig. 5-8 (a) after Ni electroless plating for 40 s. The AES spectra for Position 1 (at the top Si_3N_4 layer)

and Position 2 (at the bottom of the trench) are almost the same and the typical one is shown in Fig. 5-8 (b). It indicates Si and N peaks from Si_3N_4 layer, C and O peaks from surface absorptions, and S peak from residual electroless solution $\text{NiSO}_4 \cdot 6\text{H}_2\text{O}$. In contrast, we can only detect the Ni peaks at the side wall of the a:Si layer, as shown in Fig. 5-8 (c) for Position 3 in Fig. 5-8 (a). In other words, the Ni catalysts were successfully selectively deposited on the a:Si layers of the pattern.

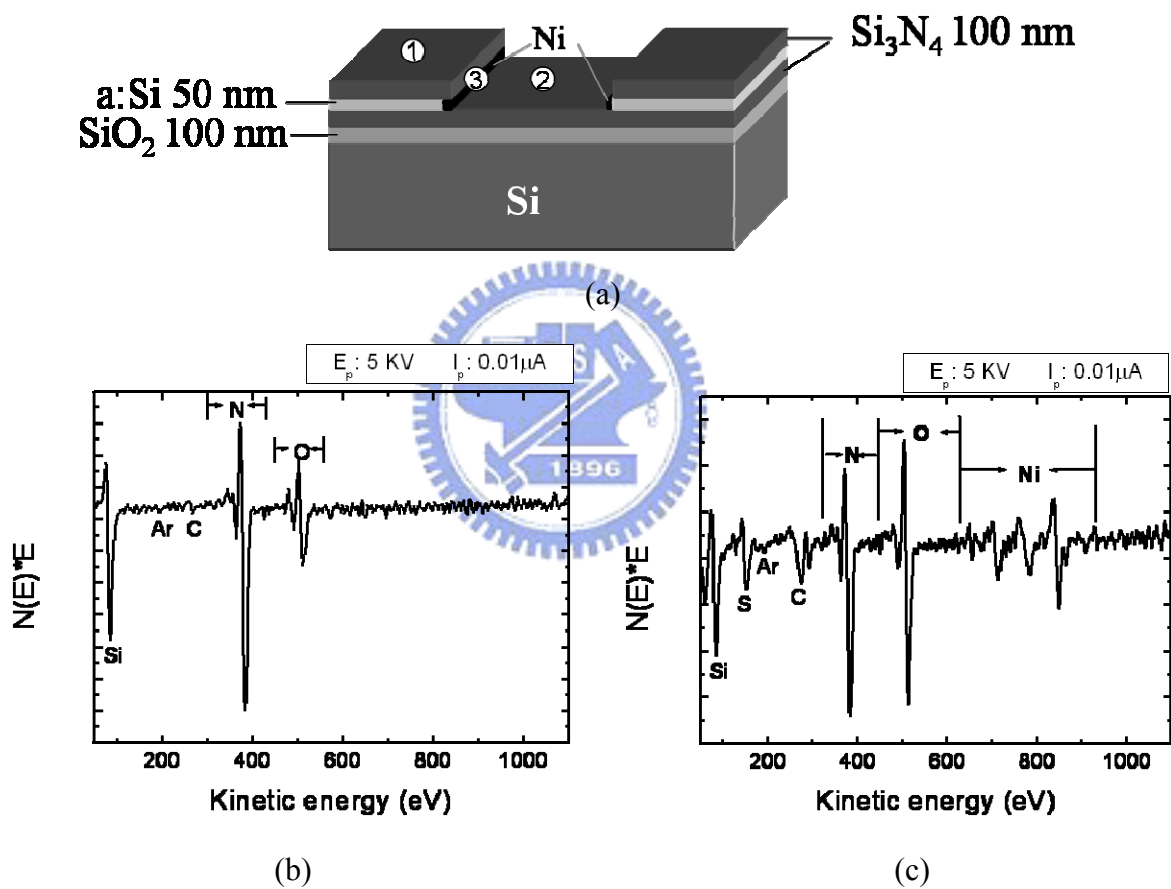


Fig. 5-8 (a) Schematic diagram showing the AES analytical positions on the patterned substrate, (b) the corresponding Auger spectra of Ni catalyst at Position 1 or 2, and (c) Position 3, respectively. (SP. #B7)

5.4 Morphologies at trench on the pattern with the Ni-assisted CNTs

The results indicate that the plating time is a crucial parameter to manipulate the tube number density of MWNTs. For Ni plating time of 10 s (Fig. 5-9 (a)), the catalyst was merely

deposited on the corner of the trench and the CNTs started to grow at the corner. For Ni plating time of 15 s (Fig. 5-9 (b)), the CNTs were grown from the catalyst film on the trench wall. Further increases in plating time to 20 s, the CNTs grown on the Ni pattern are long enough to cross the trench, as shown in Fig. 5-9 (c). Furthermore, while the electroless plating time of Ni is over 30 s (Fig. 5-9 (d)), the trench would be filled by the randomly oriented CNTs due to mutual restrictions from the neighboring CNTs.

The well-aligned horizontally oriented CNTs were reported to be synthesized on Si wafer under 200 V substrate bias and by using ECR-CVD, where the source gases were guided to flow horizontally by a Ti foil positioned 1~2 mm on top of the specimen ^[Lin, 2003-1851]. Similar process was reported by Han, et al. ^[Han 2001-5731]. They control the diameter, tube number density and orientation of CNTs on the pattern by varying the catalyst thickness, pressure, acetylene gas concentration and temperature. The horizontally-aligned CNTs were also prepared on the patterned Si towers with no catalysts on the pattern by thermal CVD, where the source gases were guided to flow through the catalyst bed ^[Franklin 2000-890], and prepared on a poly-Si pattern by the electric field-assisted thermal CVD ^[Zhang 2001-3155]. The growth mechanisms of these CNTs bridges are still a controversy issue. The proposed mechanisms are based on the following arguments: growth competition due to interaction between flow rate and flow direction differences plus van der Waals interaction ^[Bower 2000-830, Tsai 1999-3462], growth directed by interaction between electric field and the CNTs ^[Franklin 2000-890], where the field-alignment effect originates from the high polarization ability of CNTs. In this research, the typical horizontally-aligned CNT is shown in Fig. 5-10 (a) and (b), the physical restriction of Si₃N₄ layer on top of Ni catalyst layer and the self-generated electric potential difference between the trench walls will guide the ions to flow horizontally, and the tube number density can be controlled through manipulating the catalyst plating time to minimize the mutual growth restrictions by the neighboring tubes; so the CNTs can be grown horizontally across the trenches.

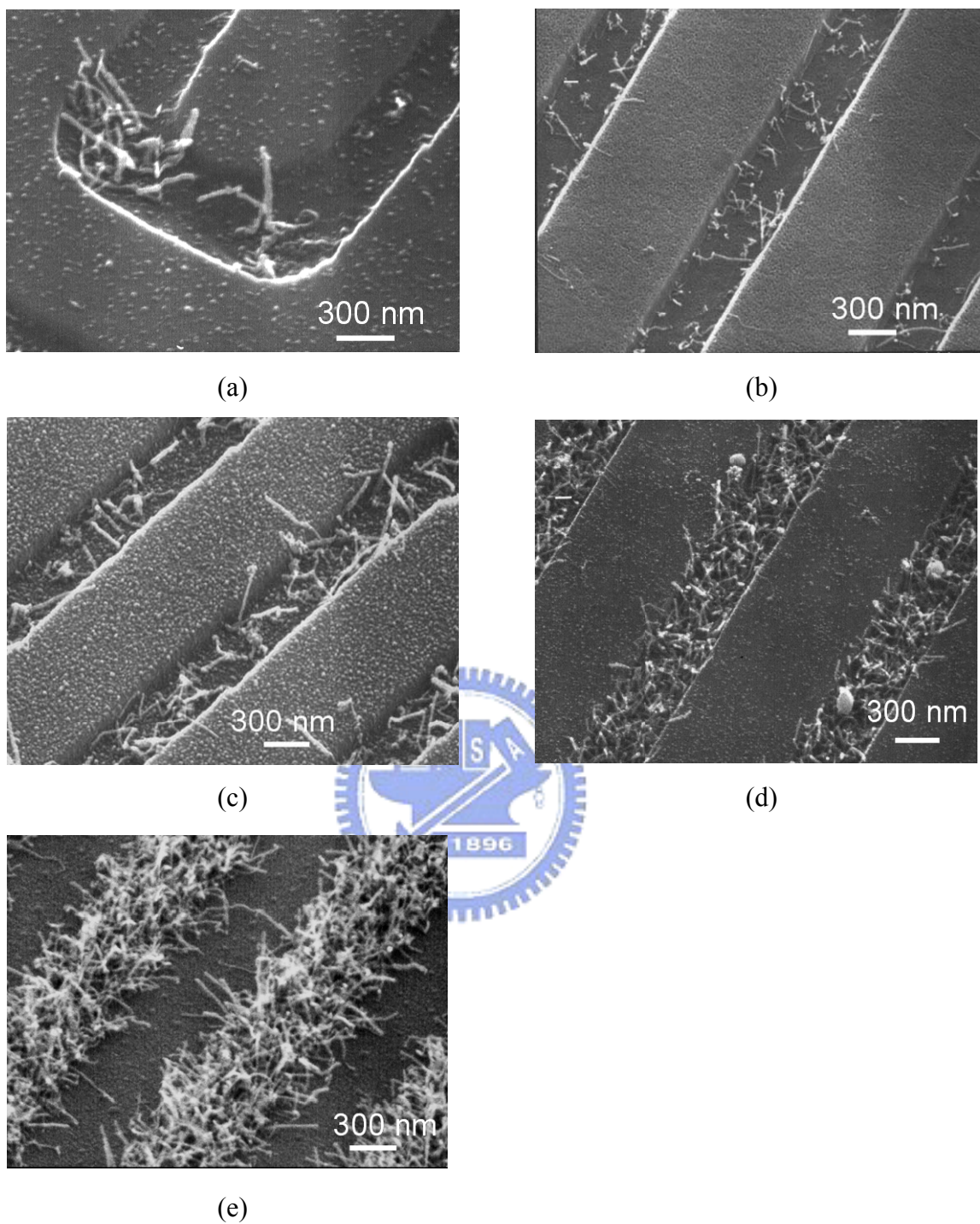


Fig. 5-9 SEM micrographs of the as-deposited CNTs on the substrate patterned by $\text{Si}_3\text{N}_4/\text{a}:\text{Si}$ under different catalyst electroless plating times: (a) 10, (b) 15 (c)20 (d)30 and (e) 60 s. (SP. # B4, B5, B6, B8 and B9, respectively)

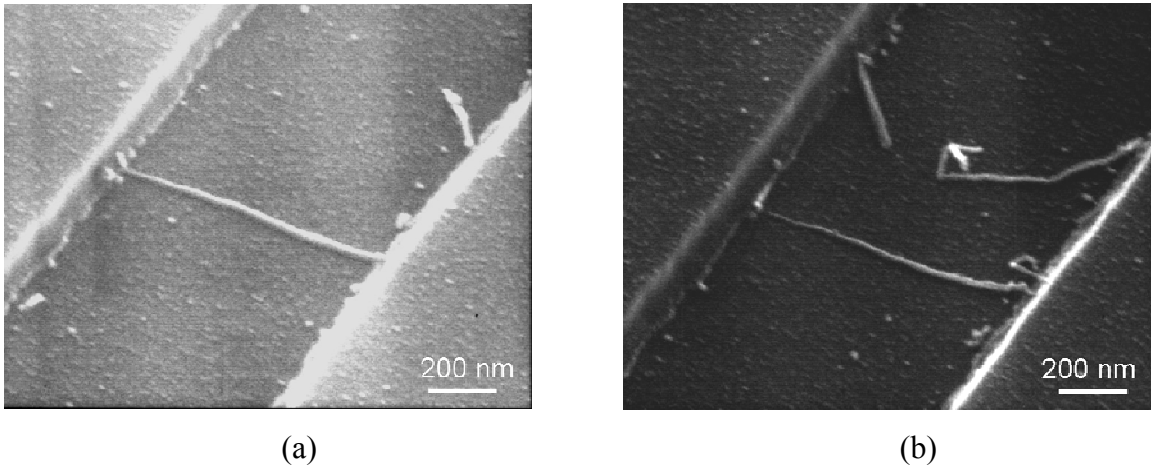


Fig. 5-10 (a) and (b) are two typical SEM micrographs of the as-deposited CNTs across trenches of the Ni-coated patterns at two different positions of SP. #B7.

5.5 I–V curves of the pattern with the horizontally-aligned CNTs across trenches

In order to examine the transport properties of the horizontally-aligned CNTs across the trench, Fig. 5-11 shows their I–V characteristics for both as-deposited and annealed patterns. The annealed pattern is treated by RTA (rapid thermal annealing) at 760°C. It indicates metallic properties at lower applied voltages with resistance of about 3×10^{13} and 5×10^{11} ohm for the as-deposited and annealed bridges, respectively. The RTA annealing may improve the

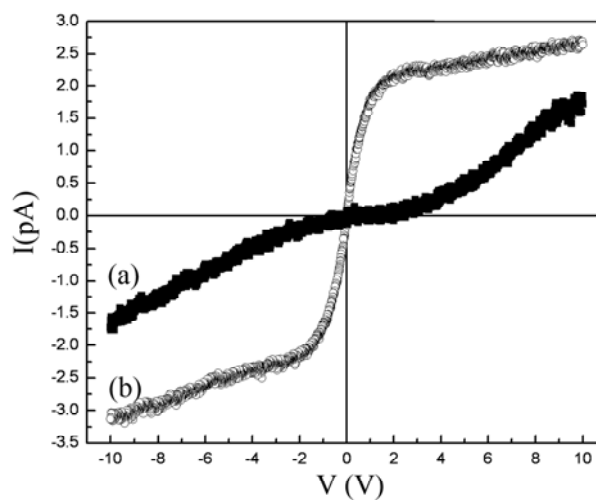


Fig. 5-11 I-V curves of the horizontally-oriented CNTs patterns, (a) the as-deposited, and (b) the post-annealed conditions. (SP. #A7)

crystallization of the CNTs and reduce the resistance of CNT-a:Si contacts . However, it shows in overall a nonlinear I–V relation, signifying non-ohmic contact between bamboo-like MWNTs and Co-catalyst on a:Si. This is in agreement with the proposed statement that the bridges may behave an intramolecular junction (a metal–semiconductor junction) due to defects of the bending parts and cause nonlinear electron transport characteristics^[Han 2001-5731].

5.6 Summary

The horizontally-aligned CNTs are selectively synthesized on the Ni-coated parts of a patterned silicon wafer in the MPCVD system. For catalysts deposited by electroless process, the features of the CNTs grown in MPCVD are 100 ~ 1200 nm in length; 10 ~ 50 nm in diameter; and the CNTs for Ni catalyst give a greater tube number density and better graphitization. The CNTs are mainly bamboo-like MWNTs and base growth mode, signifying a stronger bonding between catalyst and substrate. The possible reason for forming bamboo-like MWNTs may be the presence of the residual nitrogen on specimen from electroless catalyst deposition. The selectivity of the catalyst film by electroless plating could be obtained due to the greater chemical reactivity of the catalyst with amorphous silicon than Si₃N₄, where the catalyst by electroless process can only be deposited on a:Si substrate. The physical restriction of Si₃N₄ layer on top of Ni catalyst layer and the self-generated electric potential difference between the trench walls will guide the ions to flow horizontally, and the tube number density can be controlled through manipulating the catalyst plating time to minimize the mutual growth restrictions by the neighboring tubes; so the CNTs can be grown horizontally to form bridges between trenches. I–V results indicate in overall a nonlinear I–V relations, signifying non-ohmic contact between bamboo-like MWNTs and Ni-catalyst on a:Si and the resistance of the as-deposited MWNTs can be greatly reduced by subjecting to 760°C annealing under nitrogen atmosphere.

Chapter 6

Results and discussion for the CNSs-electrophoresis-assisted process

6.1 Raman spectrum of the raw SWNTs

The raw CNTs consist of bundles of spaghetti-like long SWNTs with average ~ 3 nm in diameter, as examined by TEM. The typical Raman spectrum of the SWNTs is depicted in Fig. 6-1 with strong peaks in radial breathing mode (RBM), indicating existence of SWNTs with high graphitization. There are also two obvious peaks around ~ 1322 and ~ 1580 cm^{-1} , which are belong to sp^3 -bonded (D band) and sp^2 -bonded (G band) carbon atoms, respectively. The intensity G band to D band ratio can go up to 15.4, also indicating high graphitization.

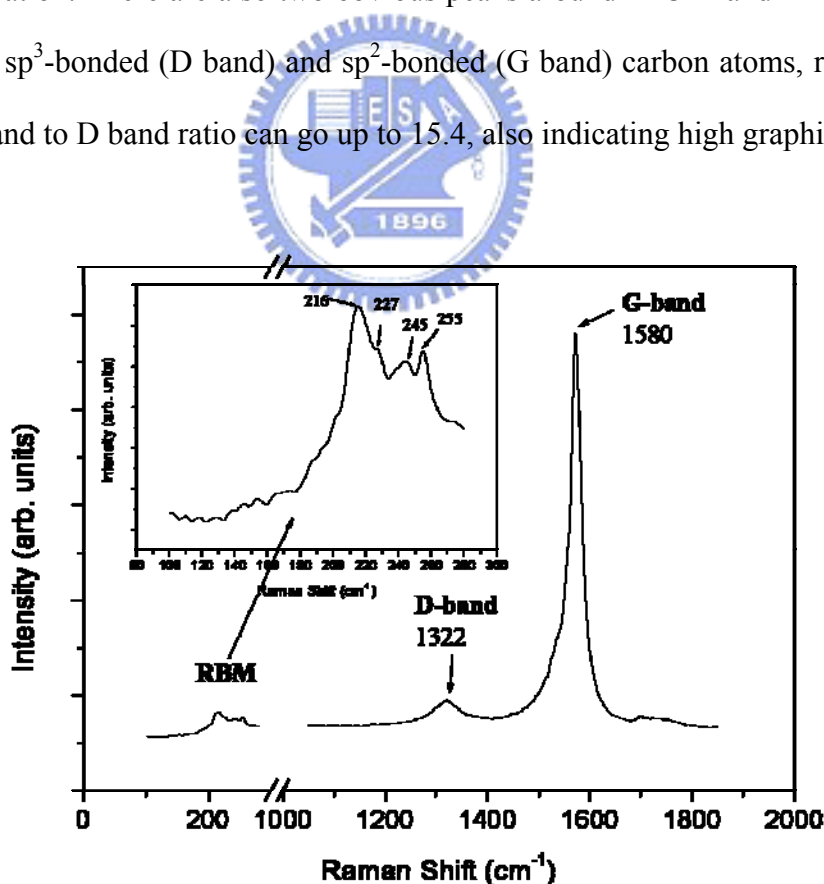


Fig. 6-1 Raman spectrum of raw SWNTs materials, the inset is the corresponding detail of RBM spectrum.

6.2 Effect of the surfactant type on stability of SWNT suspensions

In order to form the deposits with good uniformity in thickness and compositions, it is necessary to prepare suspensions with good stability and well dispersion. Four different CNT suspensions are prepared by adding different surfactants and solvents and their composition is listed in Table 3-4. D.I. water or butyl alcohol is used as solvent and different dispersant SDS, CTAB or TOPO is added to improve the CNTs dispersion stability. Photograph in Fig. 6-2(a) shows the four different as-agitated suspensions and then Fig. 6-2(b) is the photograph of suspensions placed after two weeks. For the dispersion S2 shows no indication of precipitation after prolonged standing under ambient atmosphere. Furthermore, the stability of the suspensions was also evaluated by UV-Vis absorbance spectroscopy, basing on dependence of absorption to suspension concentration. The results show no significant decreases in absorbance between as-prepared suspension with SDS surfactant and suspension after 2 weeks sedimentation (Fig. 6-3(a)). In contrast, the suspensions with TOPO or CTAB surfactants indicate significant decrease in absorbance after 2 weeks sedimentation (as also shown in Fig. 6-3(b)). In other words, SDS is a much better surfactant for this application. This may be due to fact that each CNT can be adsorbed by Van der Waals interactions and surrounded by the hydrocarbon hydrophobic part of an anionic SDS surfactant. Then, the sulfate hydrophilic part of the surfactant is oriented towards the aqueous phase, and creates a distribution of negatively charged surface for each surrounded CNT, which prevents their aggregation and induces stable suspensions in water. This suspension stability is also confirmed with the zeta potential measurements, indicating a negative zeta-potential about -60 mV in the pH range from 3 to 11. The zeta potential is an index of the magnitude of the electrostatic interaction between colloidal particles.

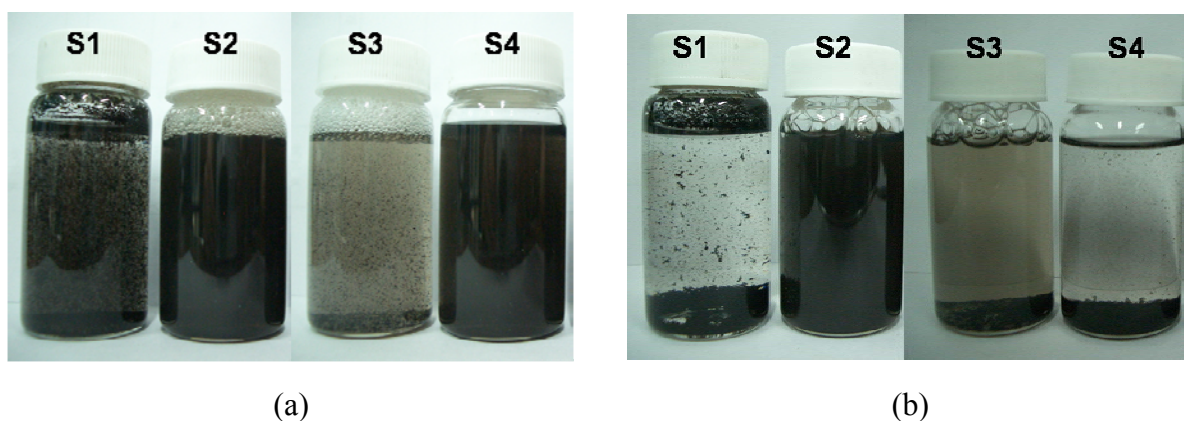


Fig. 6-2 Pictures of (a) the as-agitated suspensions, and (b) corresponding suspensions after 2 week precipitation. (Suspension designation: S1: SWNTs and D.I. water, S2: SWNTs, SDS and D.I. water, S3: SWNTs, CTAB and D.I. water, and S4: SWNTs and TOPO and butyl alcohol)

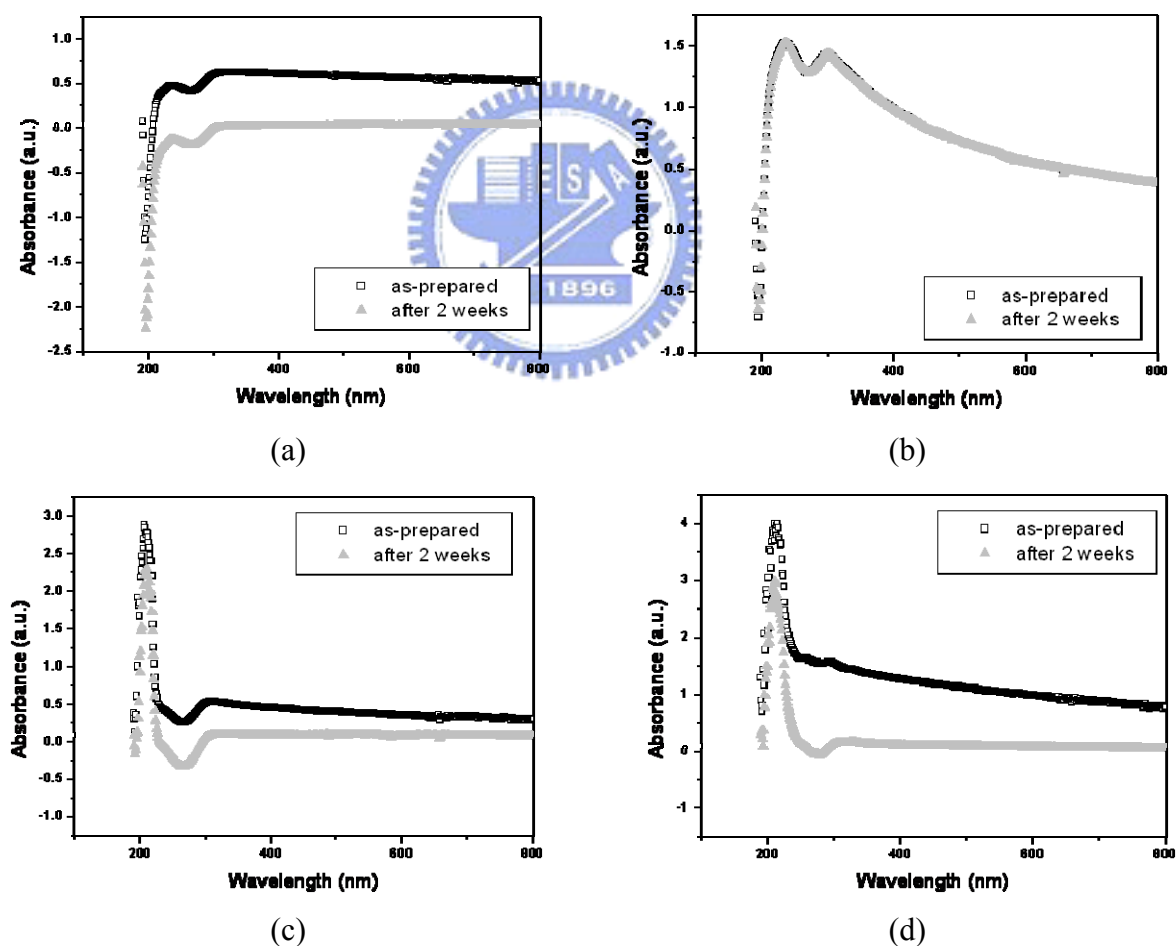
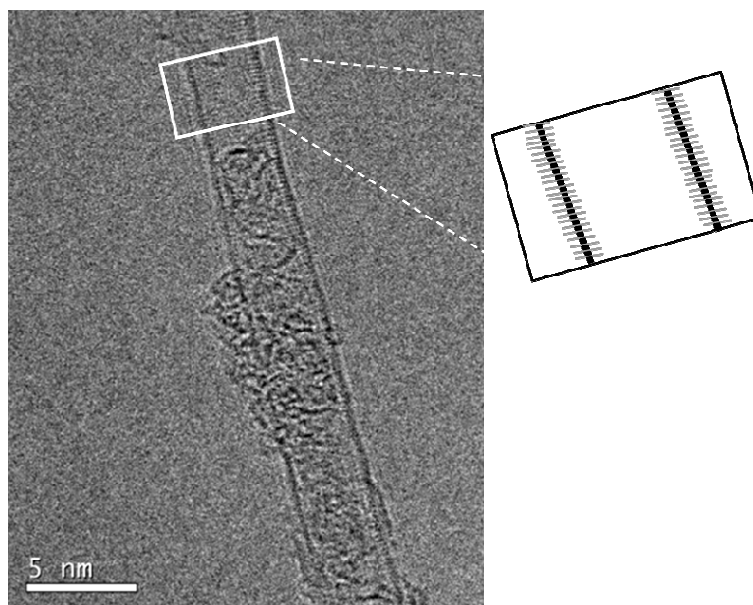
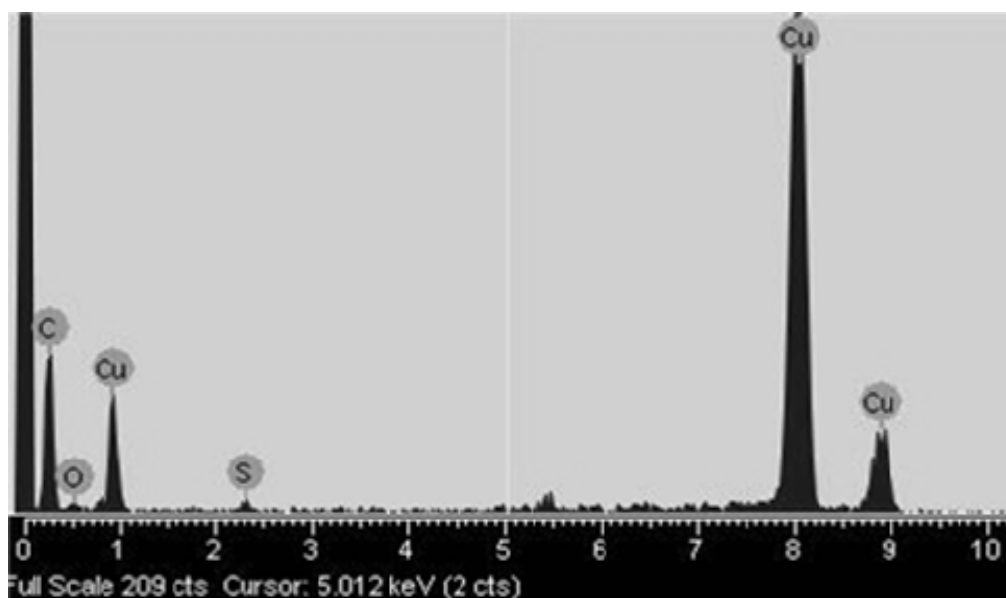


Fig. 6-3 UV-Vis absorption spectra of the as-sonicated suspensions (black line) and the corresponding suspensions after 2 weeks precipitation (grey line) for different suspensions: (a) S1, (b) S2, (c) S3 and (d) S4, respectively.



(a)



(b)

Fig. 6-4 (a) HRTEM image of the SWNT sonicated for 3 hours in SDS aqueous suspension (with schematic inset to show the SDS striations), and (b) the corresponding EDS spectrum.

The interactions between CNT and SDS surfactant are also consistent with HRTEM and EDS analyses. The suspensions in the solution after ultrasonic agitation are collected by screening and dried in air for HRTEM examination. By comparing the suspensions in the solutions after 3 hours and 15 min ultrasonic agitation, there are more individual SWNT in the former suspension, as shown in Fig. 6-4(a) HRTEM image, in which some orderly oriented

striations are observed on the surface of the CNT, as indicated by an inset. These striations represent the adsorption of the SDS molecules [Richard 2003-775]. The corresponding EDS spectrum of Fig. 6-4(a) is shown in Fig. 6-4(b), where the sulfur peak existence is another evidence for the adsorption of SDS on the surface of the CNTs.

6.3 Effect of post annealing on morphologies and field emission properties of the CNSs-EPD-assisted films

For EPD conditions of 30 V for 60 s and with SDS as surfactant, Figs. 6-5(a) to (c) show the SEM morphologies of the deposited and 3-minute-annealed films in air at 3 different annealing temperatures 100°C, 200°C and 300°C, respectively. It shows that a higher post annealing temperature for the deposited films gives rise to forming more micrometer-sized islands with the horizontally oriented SWNTs between them (Fig. 6-5(d)). During progress of annealing, the formation of islands is started by net-like crack forming, crack enlarging, tubes stretching and crack edge curling to release the film stress. Furthermore, it is interesting to note that the horizontally oriented SWNTs across the crack straits, which may provide the opportunity to measure the individual properties of the tubes.

Considering the field emission (FE) properties of the films, Fig. 6-6 presents the four curves of field emission current density (J) versus electric field (E) for the annealed films at different annealing temperatures, respectively. The results indicate that the EPD parameters, i.e. the applied voltage, electrode distance or deposition time, have no significant effects on its FE properties. In contrast, the post annealing temperature and time have a notable influence on their FE properties. The annealing process is purposed to enhance the possible chemical bonding between the film and the Al substrate, and also to remove some volatile materials and solvents in the films. The turn-on field (E_{t0}), which is defined as the electric field required to produce an emission current density of 0.01 mA/cm², decreases with increasing annealing

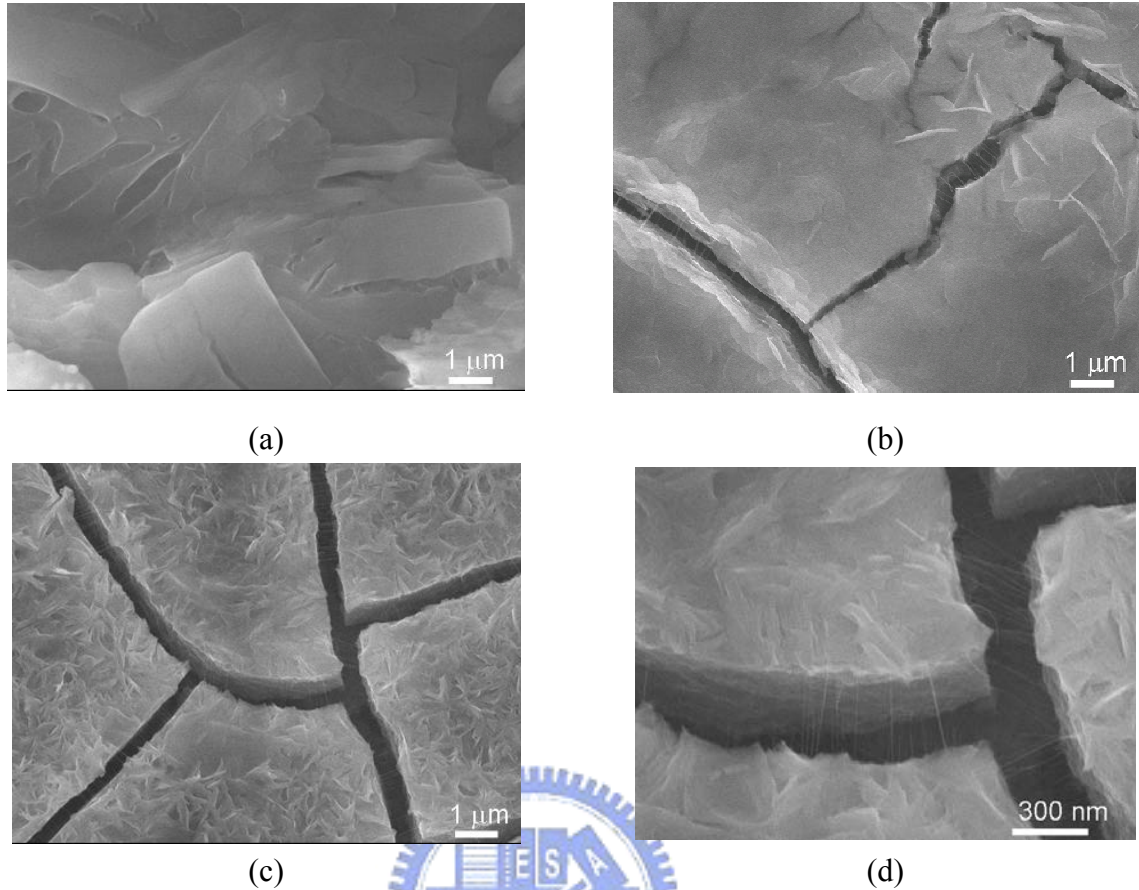


Fig. 6-5 SEM micrographs of the deposited and 3-min-annealed films under same EPD deposition conditions but different post annealing temperatures: (a) 100°C, (b) 200°C, (c) 300°C (SP. #C6, C8 and C11, respectively) and (d) is the corresponding image of (c) at higher magnification.

temperature, showing E_{to} down to 2.4 V/μm at the highest annealing temperature of 300°C in Fig. 6-6. According to FE study, the emission sites of CNTs are mainly from the defected areas of the walls or bodies of tubes [Chen 2000-2469, Hsu 2002-420, Zhou 2001-836, Jung 2002-12]. At higher annealing temperature, there are more horizontally oriented clean SWNTs stretched between the cracked islands, as shown in Fig. 6-5, which may provide more favor emission sites to enhance the FE properties. At 300°C annealing temperature, Fig. 6-7 shows the J-E curves as a function of annealing time. There is an optimum annealing time (~ 5 min) to obtain the best FE properties. In order to examine the possible reasons for the best FE properties, the tape-pulling and scratching tests were adopted to study the adhesion of the deposited films

after post annealing. This is based on the fact that a poor film-substrate adhesion generally results in greater film-substrate electrical resistance and so poorer emission ability. When the annealing time is longer than 10 min, the edges of the islands will become curling and the curling edges can cause poor adhesion and worse FE properties. In other words, a higher annealing temperature and a proper annealing time are essential to obtain the best field emission properties, where the film-substrate adhesion may play an important role.

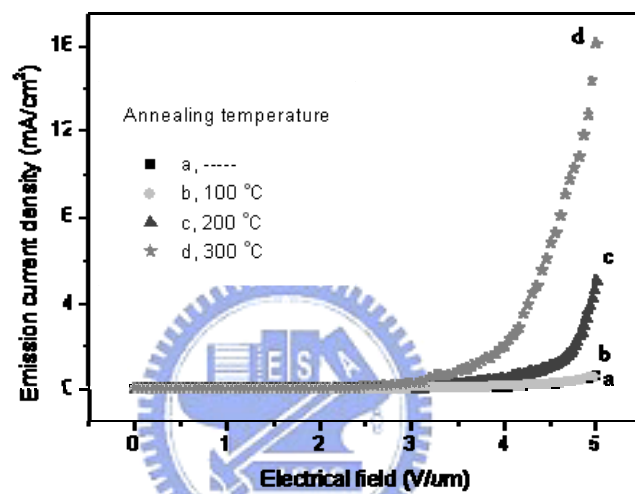


Fig. 6-6 J-E curves of the deposited and annealed films on Al-coated Si substrate under same annealing time (5 min) but different annealing temperatures: (a) as-deposited, (b) 100°C, (c) 200°C and (d) 300°C. (SP. #C5, C7, C9, and C2, respectively)

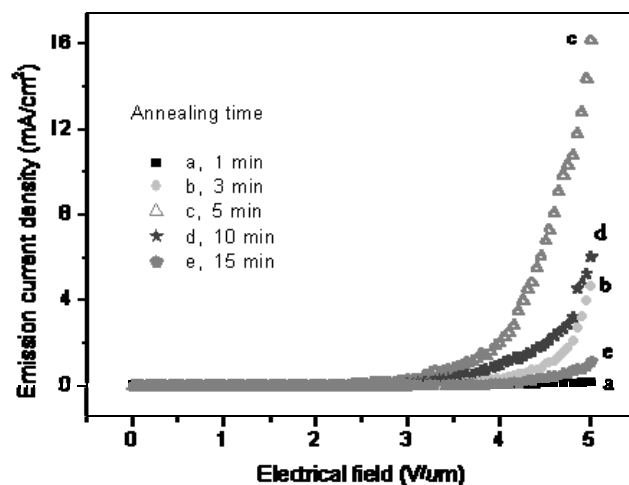


Fig. 6-7 J-E curves of the deposited and annealed films on Al-coated Si substrate under same annealing temperature (300°C) but different annealing times: (a) 1, (b) 3, (c) 5, (d) 10 and (e) 15 min. (SP. #C10, C11, C2, C12 and C13, respectively)

6.4 CNSs deposition selectivity of the pattern components by EPD

The patterns made of the Al-coating and SiO₂ films were used as substrate to examine the deposition selectivity of the SWNTs by EPD. Under EPD conditions of 30 V for 60 s and post annealing of 300°C for 5 min, the SEM morphologies of the deposited films at the Al/SiO₂ interface and on the Al coating part of the Al-SiO₂ pattern are shown in Figs. 6-8(a) and (b), respectively. It is obvious that at the left side of Fig. 6-8(a), or the nonconductive SiO₂ region of the pattern, there are no detectable SWNTs films on the surface. In contrast, there are denser of the SWNTs islands on the conductive Al regions of the pattern, as shown in Fig. 6-8(b) and right side of Fig. 6-8(a), indicating an excellent selectivity of the EPD for the SWNTs pattern deposition.

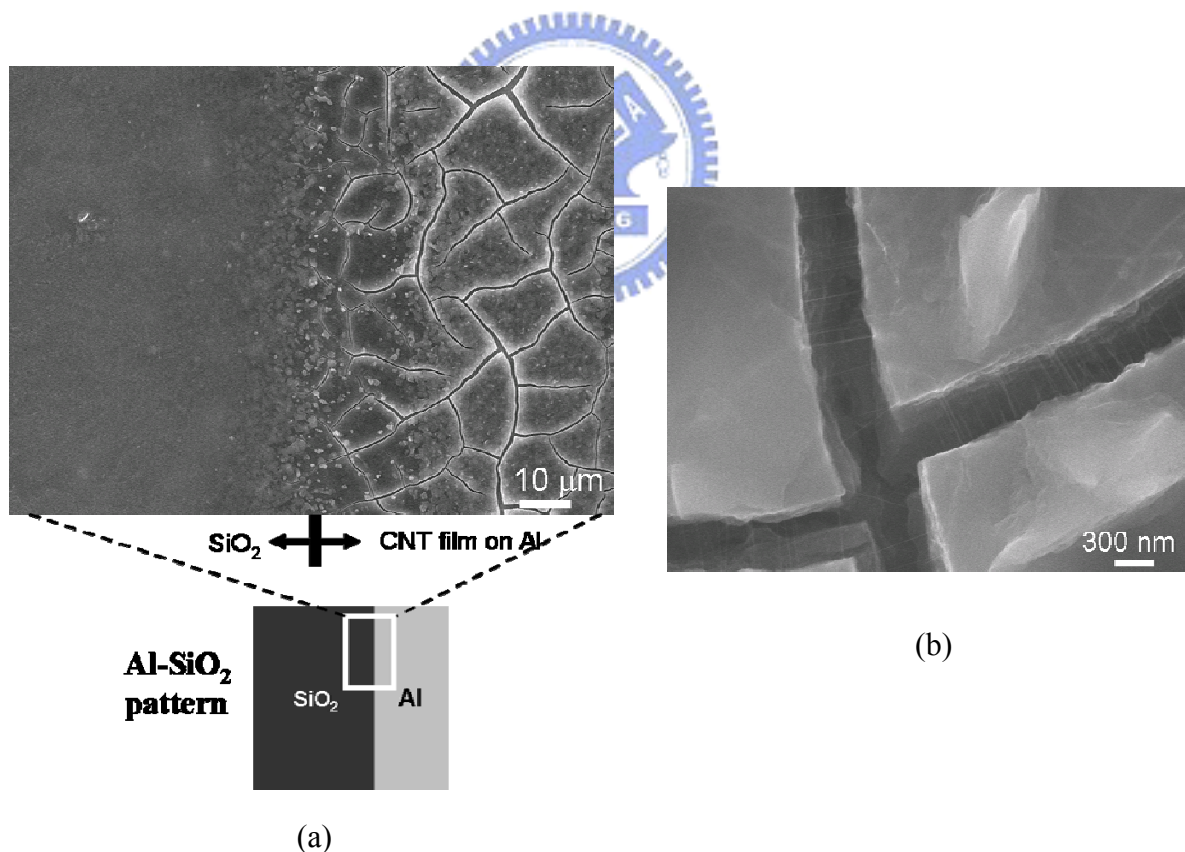


Fig. 6-8 SEM morphologies of the EPD-prepared SWNTs pattern made of Al and SiO₂ coatings: (a) at Al/SiO₂ interface (with schematic inset to show the interface position on the pattern), and (b) on the Al region of the pattern. (SP. #C15)

6.5 Substrate diversifications of the EPD process

On feasibility to apply the EPD process on other substrates, the Fig. 6-9 shows the as-deposited EPD films on the ITO by applying 50V for 120 s after post annealing at 300°C for 5 min. It has a field emission properties with a turn-on field (E_{to}) about 2.7 V/ μm . To deposit films on different shapes, for example of a curved Al-foil as shown in Fig. 6-10(a), microstructures shown in Fig. 6-10(b) is similar with the film on the Al coated Si substrate and it demonstrates a good adhesion even on the curved surface.

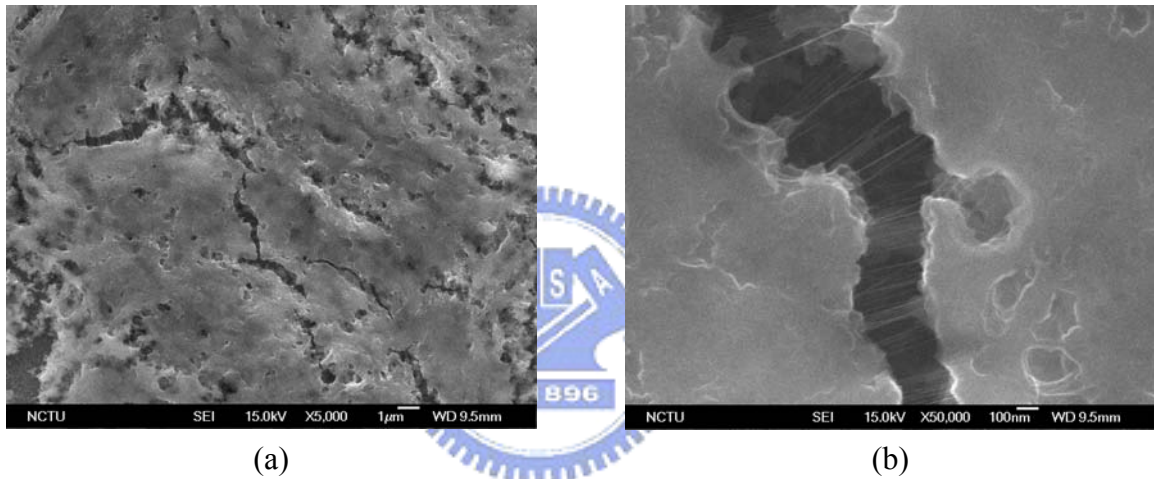


Fig. 6-9 (a) SEM morphology of the EPD-deposited film on ITO, (b) is the higher magnification SEM morphologies of the sections marked in (a). (SP. #C16)

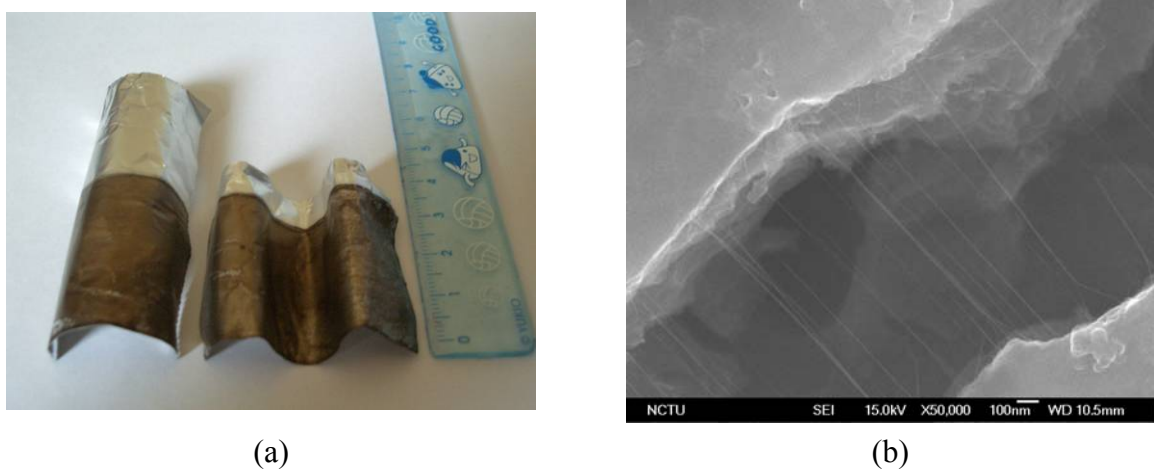
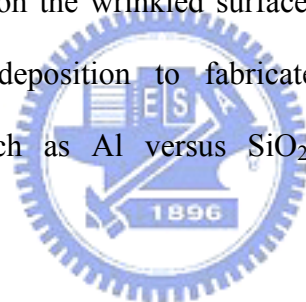


Fig. 6-10 Pictures of the EPD-deposited films on Al foil with varies shapes and higher magnification image shown in both (b). (SP. #C17)

6.6 Summary

For the EPD-deposited films, the results show that the most important parameters of the EPD and post annealing treatment are surfactant material, post annealing temperature and time. In order to form the deposit with good uniformity in thickness and compositions, the results show that the suspension with good stability and well dispersion is necessary. The SDS surfactant is the best choice in this case. A higher post annealing temperature under an optimum annealing time is more favor for the best FE properties ($E_{to} = 2.4 \text{ V}/\mu\text{m}$). The results also show that the best FE properties of the films are in consistent with the best film-substrate adhesion strength. On feasibility to apply the EPD process on other substrates with different shapes, such as ITO or the curved Al-foil, it demonstrates a good performance in emission properties and adhesion even on the wrinkled surface. On selectivity to fabricate the CNTs pattern, the selective area deposition to fabricate pattern made of conductive and nonconductive substrates, such as Al versus SiO_2 substrates in this work, has been successfully demonstrated.



Chapter 7

Conclusions

Three different processes had been successfully demonstrated their high feasibility and great potential to fabricate the CNSs patterns for nano devices applications. From the experimental results, the following conclusions can be drawn.

(a) Comparison on growth mechanisms and features of CNSs for each process

	AAO template -catalyst-assisted process	Electroless plating catalyst-assisted process	CNSs-electrophoresis- assisted process
Growth mechanism	Tip growth mode Diameter controllable	Base growth mode	SWNTs (raw material)
Types of CNSs	CNTs and CNFs	CNTs	SWNTs (raw material)
Diameters of CNSs	23 ~ 53 nm	20 ~ 55 nm	1 ~ 3 nm (raw material)
Number density of CNSs	37 ~ 162 #/ μm^2	600 ~ 2000 #/ μm^2	-

(b) Comparison on advantages and disadvantages of each process

	AAO template -catalyst-assisted process	Electroless plating catalyst-assisted process	CNSs-electrophoresis- assisted process
CNSs selectivity scheme	Template confinement and Co electroplating	Chemical reactivity between of the catalyst (Ni) with a:Si and Si ₃ N ₄ .	Conductive / nonconductive pattern
CNSs orientation control	Template confinement and tuning by Co electroplating time	Restrictions of Si ₃ N ₄ layers and proper tube number density	Post annealing
CNSs number density control	Adjusting Co electroplating time	Adjusting trench width and electroless plating time	Adjusting the concentration of SWNTs addition
Field emission properties control	Co plating time		Post annealing temperatures and times
Deposition area	Medium	Low	High
Deposition temperature	Medium	High	Low
Mass production	Medium	Low	High

Chapter 8

Future Prospects

In this research, the AAO-template-catalyst-assisted, electroless plating catalyst-assisted and CNSs-electrophoresis-assisted CNSs pattern fabrication processes were studied to examine the selectivity of the process and the structure-property manipulations. However, there are still many unknown questions that need to study further:

(a) Effects of catalyst-substrate bonding, CNSs alignment, tube diameter uniformity, tube number density and the AAO template pore size on field emission properties can be further studied.

(b) For electroless plating catalyst-assisted process, further studies can focus on manipulating the CNSs connectors across the trenches at the desired spots and with the desired tube diameter and chirality. The contact resistance between tube and trench is another issue to study.

(c) For CNSs-electrophoresis-assisted process, effect of contamination of the suspension on properties of the CNSs-EPD-assisted films needs to study further. Pollution problem of the chemical process is also an important issue for this and other processes. Other processes to functionalize the CNSs directly without using surfactants are also a possible route to prepare the CNSs-assisted films.

References

A

1. Ago, H., K. Petritsch, M. S. P. Shaffer, A. H. Windle, and R. H. Friend, *Advanced Materials* 11 (1999) 1281-1285, "Composites of carbon nanotubes and conjugated polymers for photovoltaic devices".
2. Ago, H., K. Nakamura, K. I. Ikeda, N. Uehara, N. Ishigami, and M. Tsuji, *Chemical Physics Letters* 408 (2005) 433-438, "Aligned growth of isolated single-walled carbon nanotubes programmed by atomic arrangement of substrate surface".
3. Ajayan P, Zhou O. *Applications of carbon nanotubes*, University of North Carolina; 2001. p. 391-425.

B

4. Bachtold, A., P. Hadley, T. Nakanishi, and C. Dekker, *Science* 294 (2001) 1317-1320, "Logic circuits with carbon nanotube transistors".
5. Baughman, R. H., A. A. Zakhidov, and W. A. de Heer, *Science* 297 (2002) 787-792, "Carbon nanotubes - the route toward applications".
6. Boccaccini, A. R., J. Cho, J. A. Roether, B. J. C. Thomas, E. J. Minay, and M. S. P. Shaffer, *Carbon* 44 (2006) 3149-3160, "Electrophoretic deposition of carbon nanotubes".
7. Bower, C, W. Zhu, S. H. Jin, and O. Zhou, *Applied Physics Letters* 77 (2000) 830-832, "Plasma-induced alignment of carbon nanotubes".
8. Britto, P. J., K. S. V. Santhanam, A. Rubio, J. A. Alonso, and P. M. Ajayan, *Advanced Materials* 11 (1999) 154-157, "Improved charge transfer at carbon nanotube electrodes".
9. Brodie, I., C. Spindt, *Advances in electronics and electron physics* 83 (1992) 1-106, "Vacuum microelectronics".
10. Burghard, M., G. Duesberg, G. Philipp, J. Muster, and S. Roth, *Advanced Materials* 10 (1998) 584-588, "Controlled adsorption of carbon nanotubes on chemically modified electrode arrays".

C

11. Chambers, S. A., T. Droubay, D. R. Jennison, and T. R. Mattsson, *Science* 297 (2002) 827-831, "Laminar growth of ultrathin metal films on metal oxides: Co on hydroxylated alpha-Al₂O₃(0001)".

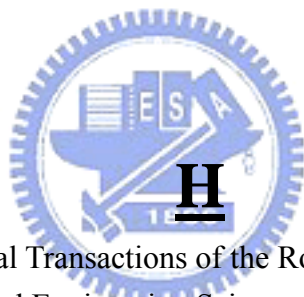
12. Che, G., B. B. Lakshmi, C. R. Martin, E. R. Fisher, and R. S Ruoff., *Chemistry of Materials* 10 (1998) 260-267, "Chemical vapor deposition based synthesis of carbon nanotubes and nanofibers using a template method".
13. Chen, P., X. Wu, J. Lin, and K. L. Tan, *Science* 285 (1999) 91-93, "High H₂ uptake by alkali-doped carbon nanotubes under ambient pressure and moderate temperatures".
14. Chen, P. L., J. K. Chang, C. T. Kuo, and F. M. Pan, *Applied Physics Letters* 86 (2005) 123111, "Field emission of carbon nanotubes on anodic aluminum oxide template with controlled tube density".
15. Chen, X. Q., T. Saito, H. Yamada, and K. Matsushige, *Applied Physics Letters* 78 (2001) 3714-3716, "Aligning single-wall carbon nanotubes with an alternating-current electric field".
16. Cheng, Y., and O. Zhou, *Comptes Rendus Physique* 4 (2003) 1021-1033, "Electron field emission from carbon nanotubes".
17. Chen, Y., D. T. Shaw, and L. Guo, *Applied Physics Letters* 76 (2000) 2469-2471, "Field emission of different oriented carbon nanotubes".
18. Choi, I. M., S. Y. Woo, and S. S. Hong, *Journal of Vacuum Science & Technology A* 24 (2006) 1556-1559, "Vacuum measurement by carbon nanotube field emission".
19. Choi, W. B., D. S. Chung, J. H. Kang, H. Y. Kim, Y. W. Jin, I. T. Han, Y. H. Lee, J. E. Jung, N. S. Lee, G. S. Park, and J. M. Kim, *Applied Physics Letters* 75 (1999) 3129-3131, "Fully sealed, high-brightness carbon-nanotube field-emission display".
20. Claye, A. S., J. E. Fischer, C. B. Huffman, A. G. Rinzler, and R. E. Smalley, *Journal of the Electrochemical Society* 147 (2000) 2845-2852, "RE Solid-state electrochemistry of the Li single wall carbon nanotube system".
21. Collins, P. G., and A. Zettl, *Physical Review B* 55 (1997) 9391-9399, "Unique characteristics of cold cathode carbon-nanotube-matrix field emitters".

D

22. Dean, K. A., and B. R. Chalamala, *Applied Physics Letters* 76 (2000) 375-377, "Current saturation mechanisms in carbon nanotube field emitters".
23. Deheer, W. A., A. Chatelain, and D. Ugarte, *Science* 270 (1995) 1790-1180, "A carbon nanotube field-emission electron source".
24. Dillon, A. C., K. M. Jones, T. A. Bekkedahl, C. H. Kiang, D. S. Bethune, and M. J. Heben, *Nature* 386 (1997) 377-379, "Storage of hydrogen in single-walled carbon nanotubes".
25. Du, C. S., J. Yeh, and N. Pan, *Journal of Materials Chemistry* 15 (2005) 548-550, "Carbon nanotube thin films with ordered structures".

F

26. Fan, Shoushan, M. G. Chapline, N. R. Franklin, T. W. Tombler, A. M. Cassell, and H. Dai, *Science* 283 (1999) 512-514, "Self-oriented regular arrays of carbon nanotubes and their field emission properties".
27. Felten, A., C. Bittencourt, J. J. Pireaux, G. Van Lier, and J. C. Charlier, *Journal of Applied Physics* 98 (2005) 074308, "Radio-frequency plasma functionalization of carbon nanotubes surface O₂, NH₃, and CF₄ treatments".
28. Ferrari, AC, and J. Robertson, *Physical Review B* 61 (2000) 14095-14107, "Interpretation of Raman spectra of disordered and amorphous carbon".
29. Fowler, R. H. and L. W. Nordheim, *Proc. Roy. Soc., Ser. A* 119 (1928) 173-176, "Electron emission in intense electric fields".
30. Franklin, N. R., and H. J. Dai, *Advanced Materials* 12 (2000) 890-894, "An enhanced CVD approach to extensive nanotube networks with directionality".
31. Fuhrer, M. S., J. Nygard, L. Shih, M. Forero, Y. G. Yoon, M. S. C. Mazzoni, H. J. Choi, J. Ihm, S. G. Louie, A. Zettl, and P. L. McEuen, *Science* 288 (2000) 494-497, "Crossed nanotube junctions".



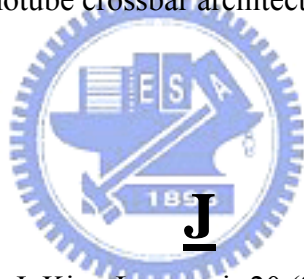
32. Haddon, R. C., *Philosophical Transactions of the Royal Society of London Series A-Mathematical Physical and Engineering Sciences*, 343 (1993) 53-62, "The fullerenes - powerful carbon-based electron-acceptors".
33. Hafner, J. H., C. L. Cheung, and C. M. Lieber, *Nature* 398 (1999) 761-762, "Growth of nanotubes for probe microscopy tips".
34. Han, Y. S., J. K. Shin, and S. T. Kim, *Journal of Applied Physics* 90 (2001) 5731-5734, "Synthesis of carbon nanotube bridges on patterned silicon wafers by selective lateral growth".
35. Harutyunyan A. R., T. Tokune, and E. Mora, *Applied Physics Letters* 86 (2005) 153113, "Liquefaction of catalyst during carbon single-walled nanotube growth".
36. Heimann, R. B., S. E. Evsyukov, and Y. Koga, *Carbon* 35 (1997) 1654-1658, "Carbon allotropes: a suggested classification scheme based on valence orbital hybridization".
37. Hernadi, K., A. Fonseca, J. B. Nagy, D. Bernaerts, A. Fudala, and A. A. Lucas, *Zeolites* 17 (1996) 416-432, "Catalytic synthesis of carbon nanotubes using zeolite support".
38. Hilding, J., E. A. Grulke, Z. G. Zhang, and F. Lockwood, *Journal of Dispersion Science and Technology* 24 (2003) 1-41, "Dispersion of carbon nanotubes in liquids".
39. Hofmann, S., M. Cantoro, B. Kleinsorge, C. Casiraghi, A. Parvez, J. Robertson, and C. Ducati, *Journal of Applied Physics* 98 (2005) 034308, "Effects of catalyst film thickness

on plasma-enhanced carbon nanotube growth”.

40. Hsu, C. M., C. H. Lin, H. L. Chang, and C. T. Kuo, *Thin Solid Films* 420 (2002) 225-229, “Growth of the large area horizontally-aligned carbon nanotubes by ECR-CVD”.
41. Huang, S., B. Maynor, X. Cai, and J. Liu, *Advanced Materials* 15 (2003) 1651-1655, “Ultralong, well-aligned single walled carbon nanotube architectures on surfaces”.
42. http://en.wikipedia.org/wiki/Allotrope_of_carbon
43. <http://www.personal.psu.edu/users/s/b/sbk142/nanotube.htm>

I

44. Iijima, S., *Nature* 354 (1991) 56-58, “Helical microtubules of graphitic carbon”.
45. Islam, M. F., E. Rojas, D. M. Bergey, A. T. Johnson, and A. G. Yodh, *Nano Letters* 3 (2003) 269-273, “High weight fraction surfactant solubilization of single-wall carbon nanotubes in water”.
46. Ismach, A. and E. Joselevich, *Nano Letters* 6 (2006) 1706-1710, “Orthogonal self-assembly of carbon nanotube crossbar architectures by simultaneous graphoepitaxy and field-directed growth”.



47. Jang, S. R., R. Vittal, and K. J. Kim, *Langmuir* 20 (2004) 9807-9810, “Incorporation of functionalized single-wall carbon nanotubes in dye-sensitized TiO₂ solar cells”.
48. Joselevich, E., and C. M. Lieber, *Nano Letters* 2 (2002) 1137- 1141, “Vectorial growth of metallic and semiconducting single-wall carbon nanotubes”.
49. Jung, Y. S., and D. Y. Jeon, *Applied Surface Science* 193 (2002) 129-137, “Surface structure and field emission property of carbon nanotubes grown by radio-frequency plasma-enhanced chemical vapor deposition”.

K

50. Kanzow, H., A. Schmalz, and A. Ding, *Chemical Physics Letters* 295 (1998) 525-530, “Laser-assisted production of multi-walled carbon nanotubes from acetylene”.
51. Kim, D. Y., J. B. Yoo, I. T. Han, H. J. Kim, H. J. Kim, J. E. Jung, Y. W. Jin, J. M. Kim, and K. H. Chin, *Diamond and Related Materials* 14 (2005) 2084-2088, “The density control of carbon nanotubes using spin-coated nanoparticle and its application to the electron emitter with triode structure”.

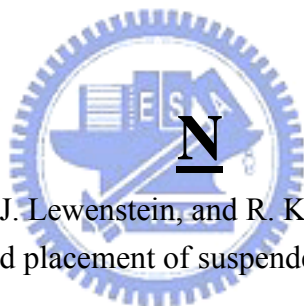
52. Kim, P., and C. M. Lieber, *Science* 286 (1999) 2148-2150, "Nanotube nanotweezers".
53. Kim, Y., S. Hong, S. Jung, M. S. Strano, J. Choi, and S. Baik, *Journal of Physical Chemistry B* 110 (2006) 1541-1545, "Dielectrophoresis of surface conductance modulated single-walled carbon nanotubes using cationic surfactants".
54. Kongkanand, A., R. M. Dominguez, and P. V. Kamat, *Nano Letters* 7(2007) 676-680, "Single wall carbon nanotube scaffolds for photoelectrochemical solar cells. Capture and transport of photogenerated electrons".
55. Kroto, H. W., J. R. Heath, S. C. O'Brien, R. F. Curl, and R. E. Smalley, *Nature* 318 (1985) 162-163, "C₆₀ – Buckminsterfullerene".
56. Krupke, R., F. Hennrich, H. B. Weber, M. M. Kappes, and H. V. Lohneysen, *Nano Letters* 3 (2003) 1019-1023, "Simultaneous deposition of metallic bundles of single-walled carbon nanotubes using ac-dielectrophoresis".

L

57. Lambin, P., V. Meunier, L. Henrard, and A. A. Lucas, *Carbon* 38 (2000) 1713-1721, "Measuring the helicity of carbon nanotubes".
58. Lee, J. S., G. H. Gu, H. Kim, K. S. Jeong, J. Bae, and J. S. Suh, *Chemistry of Materials* 13 (2001) 2387-2391, "Growth of carbon nanotubes on anodic aluminum oxide templates: Fabrication of a tube-in-tube and linearly joined tube".
59. Lee, N. S., D. S. Chung, I. T. Han, J. H. Kang, Y. S. Choi, H. Y. Kim, S. H. Park, Y. W. Jin, W. K. Yi, M. J. Yun., J. E. Jung, C. J. Lee, J. H. You, S. H. Jo, C. G. Lee, and J. M. Kim, *Diamond and Related Materials* 10 (2001) 265-270, "Application of carbon nanotubes to field emission displays".
60. Lee, T. Y., P. S. Alegaonkar, and J. B. Yoo, *Thin Solid Films* 515(2007) 5131-5135, "Fabrication of dye sensitized solar cell using TiO₂ coated carbon nanotubes".
61. Li, A. P., F. Muller, A. Birner, K. Nielsch, and U. Gosele, *Journal of Applied Physics* 84 (1998) 6023-6026, "Hexagonal pore arrays with a 50-420 nm interpore distance formed by self-organization in anodic alumina".
62. Li, F. Y., L. Zhang, and R. M. Metzger, *Chemistry of Materials* 10 (1998) 2470-2480, "On the growth of highly ordered pores in anodized aluminum oxide".
63. Li, J., C. Papadopoulos, J. M. Xu, and M. Moskovits, *Applied Physics Letters* 75 (1999) 367-369, "Highly-ordered carbon nanotube arrays for electronics applications".
64. Lin, C. H., H. L. Chang, C. M. Hsu, A. Y. Lo, and C. T. Kuo, *Diamond and Related Materials* 12 (2003)1851-1857, "The role of nitrogen in carbon nanotube formation".
65. Liu, C., Y. Y. Fan, M. Liu, H. T. Cong, H. M. Cheng, and M. S. Dresselhaus, *Science* 286 (1999) 1127-1129, "Hydrogen storage in single-walled carbon nanotubes at room temperature".

M

66. Marsh, D. H., G. A. Rance, M. H. Zaka, R. J. Whitby, and A. N. Khlobystov, *Physical Chemistry Chemical Physics* 9 (2007) 5490-5496, "Comparison of the stability of multiwalled carbon nanotube dispersions in water".
67. Meitl, M. A., Y. Zhou, A. Gaur, S. Jeon, M. L. Usrey, M. S. Strano, and J.A. Rogers, *Nano Letters* 4 (2004) 1643-1647, "Solution casting and transfer printing single-walled carbon nanotube films".
68. Miller, A. J., R. A. Hatton, and S. R. P. Silva, *Applied Physics Letters* 89 (2006) 133117, "Interpenetrating multiwall carbon nanotube electrodes for organic solar cells".
69. Miller, A. J., R. A. Hatton, and S. R. P. Silva, *Applied Physics Letters* 89 (2006) 123115, "Water-soluble multiwall-carbon-nanotube-polythiophene composite for bilayer photovoltaics".
70. Miller, A. J., R. A. Hatton, and S. R. P. Silva, *Applied Physics Letters* 90 (2007) 023105, "Carbon nanotubes grown on In_2O_3 : Sn glass as large area electrodes for organic photovoltaics".



71. Nagahara, L. A., I. Amlani, J. Lewenstein, and R. K. Tsui, *Applied Physics Letters* 80 (2002) 3826-3828, "Directed placement of suspended carbon nanotubes for nanometer-scale assembly".
72. Nilsson, L., O. Groening, C. Emmenegger, O. Kuettel, E. Schaller, L. Schlapbach, H. Kind, J. M. Bonard, and K. Kern, *Applied Physics Letters* 76 (2000) 2071-2073, "Scanning field emission from patterned carbon nanotube films".
73. Nutzenadel, C., A. Zuttel, D. Chartouni, and L. Schlapbach, *Electrochemical and Solid State Letters* 2 (1999) 30-32, "Electrochemical storage of hydrogen in nanotube materials".

P

74. Planeix, J. M., N. Coustel, B. Coq, V. Brotons, P. S. Kumbhar, R. Dutartre, P. Geneste, P. Bernier, and P. M. Ajayan, *Journal of the American Chemical Society* 116 (1994) 7935-7936, "Application of carbon nanotubes as supports in heterogeneous catalysis".
75. Plank, N. O. V., L. D. Jiang, and R. Cheung, *Applied Physics Letters* 83 (2003) 2426-2428, "Fluorination of carbon nanotubes in CF_4 plasma".

R

76. Ren, Z. F., Z. P. Huang, D. Z. Wang, J. G. Wen, J. W. Xu, J. H. Wang, L. E. Calvet, J. Chen, J. F. Klemic, and M. A. Reed, *Applied Physics Letters* 75 (1999) 1086-1088, "Growth of a single freestanding multiwall carbon nanotube on each nanonickel dot".
77. Richard, C., F. Balavoine, P. Schultz, T. W. Ebbesen, and C. Mioskowski, *Science* 300 (2003) 775-778, "Supramolecular self-assembly of lipid derivatives on carbon nanotubes".
78. Rochefort, A., M. Di Ventura, and P. Avouris, *Applied Physics Letters* 78 (2001) 2521-2523, "Switching behavior of semiconducting carbon nanotubes under an external electric field".
79. Rodriguez, N. M., A. Chambers, and R. T. K. Baker, *Langmuir* 11 (1995) 3862-3866, "Catalytic engineering of carbon nanostructures".
80. Rosen, R., W. Simendinger, C. Debbault, H. Shimoda, L. Fleming, B. Stoner, and O. Zhou, *Applied Physics Letters* 76 (2000) 1668-1670, "Application of carbon nanotubes as electrodes in gas discharge tubes".



81. Saito, Y., S. Uemura, and K. Hamaguchi, *Japanese Journal of Applied Physics Part 2-Letters & Express Letters* 37 (1998) L346-L348, "Cathode ray tube lighting elements with carbon nanotube field emitters".
82. Saito, Y., and S. Uemura, *Carbon* 38 (2000) 169-182, "Field emission from carbon nanotubes and its application to electron sources".
83. Sugie, H., M. Tanemura, V. Filip, K. Iwata, K. Takahashi, and F. Okuyama, *Applied Physics Letters* 78 (2001) 2578-2580, "Carbon nanotubes as electron source in an x-ray tube".

T

84. Tamor, M. A., and W. C. Vassell, *Journal of Applied Physics* 76 (1994) 3823-3830, "Raman fingerprinting of amorphous-carbon films".
85. Tanaka, H., S. Akita, L. J. Pan, and Y. Nakayama, *Japanese Journal of Applied Physics Part 1-Regular Papers Short Notes & Review Papers* 43 (2004) 1651-1654, "Instability of field emission from a standalone multiwalled carbon nanotube with an insulator barrier".
86. Teo, K. B. K., M. Chhowalla, G. A. J. Amaratunga, W. I. Milne, D. G. Hasko, G. Pirio, P. Legagneux, F. Wyczisk, and D. Pribat, *Applied Physics Letters* 79 (2001) 1534-1536, "Uniform patterned growth of carbon nanotubes without surface carbon".

87. Thamida, S. K., and H. C. Chang, Chaos 12 (2002) 240-251, "Nanoscale pore formation dynamics during aluminum anodization".
88. Ting, C. H., and M. Paunovic, Journal of the Electrochemical Society 136(1989) 456-462, "Selective electroless metal-deposition for integrated-circuit fabrication".
89. Tsai, S. H., C. W. Chao, C. L. Lee, and H. C. Shih, Applied Physics Letters 74 (1999) 3462-3464, "Bias-enhanced nucleation and growth of the aligned carbon nanotubes with open ends under microwave plasma synthesis".

U

90. Ural, A., Y. Li, and H. Dai, Applied Physics Letters 81 (2002) 3464- 3466, "Electric-field-aligned growth of single-walled carbon nanotubes on surfaces".
91. Utsumi, T., IEEE Trans. Electron Devices 38 (1991) 2276-2283, "Vacuum microelectronics: what's new and exciting".



W

92. Wang, W. K., and J. H. Zhao, Diffusions in Materials: Dimat 2000, Pts 1 & 2 Book Series: Defect and Diffusion Forum 194-1 (2001) 883-889, "Determination of the interdiffusion coefficients of liquid Zn and Sn using Ta/Zn-Sn/Si trilayers".
93. Wang, X. G., and J. R. Smith, Physical Review B 70 (2004) 081401, "Hydrogen and carbon effects on Al₂O₃ surface phases and metal deposition".
94. Wei, Y. Y., X. Fan, and G. Eres, Journal of Vacuum Science & Technology B 18 (2000) 3586-3589, "Directed assembly of carbon nanotube electronic circuits by selective area chemical vapor deposition on prepatterned catalyst electrode structures".
95. Wong, Y. M., W. P. Kang, J. L. Davidson, B. K. Choi, Hofmeister W., and J. H. Huang, Diamond and Related Materials 15(2006) 334-340, "Fabrication of aligned convex CNT field emission triode by MPCVD".

X

96. Xu, N. S., S. Z. Deng, and J. Chen, Ultramicroscopy 95 (2003) 19-28, "Nanomaterials for field electron emission: preparation, characterization and application".

Y

97. Yamabe, T., M. Imade, M. Tanaka, and T. Sato, *Synthetic Metals* 117 (2001) 61-65, "Electronic structures and transport properties of carbon nanotube".
98. Yang, Z. H., and H. Q. Wu, *Materials Chemistry and Physics* 71 (2001) 7-11, "Electrochemical intercalation of lithium into raw carbon nanotubes".
99. Yang, Z. H., Y. Feng, Z. F. Li, S. B. Sang, Y. H. Zhou, and L. H. Zeng, *Journal of Electroanalytical Chemistry* 580 (2005) 340-347, "An investigation of lithium intercalation into the carbon nanotubes by a.c. impedance".
100. Yao, B. D., and N. Wang, *Journal of Physical Chemistry B* 105 (2001) 11395-11398, "Carbon nanotube arrays prepared by MWCVD".

Z

101. Zhang, Z. J., B. Q. Wei, G. Ramanath, and P. M. Ajayan, *Applied Physics Letters* 77 (2000) 3764-3766, "Substrate-site selective growth of aligned carbon nanotubes".
102. Zhang, Y. G., A. L. Chang, J. Cao, Q. Wang, W. Kim, Y. M. Li, N. Morris, E. Yenilmez, J. Kong, and H. J. Dai, *Applied Physics Letters* 79 (2001) 3155-3157, "Electric-field-directed growth of aligned single-walled carbon nanotubes".
103. Zhi, C. Y., X. D. Bai, and E. G. Wang, *Applied Physics Letters* 81 (2002) 1690-1692, "Enhanced field emission from carbon nanotubes by hydrogen plasma treatment".
104. Zhou G., W. H. Duan, and B. L. Gu, *Applied Physics Letters* 79 (2001) 836-838, "Dimensional effects on field emission properties of the body for single-walled carbon nanotube".